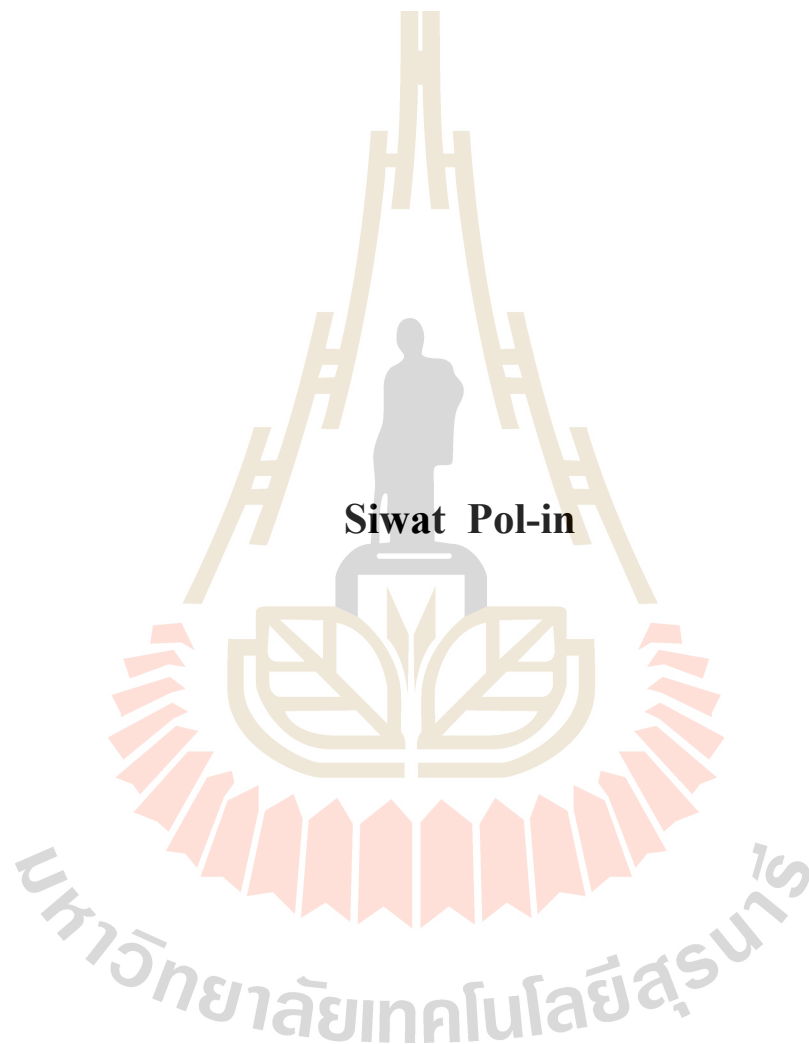


**MAGNETIC STUDY OF LIGHT SENSITIVE  
MATERIALS BY KERR EFFECT MEASUREMENT**



**A Thesis Submitted in Partial Fulfillment of the Requirement for the  
Degree of Doctor of Philosophy in Physics  
Suranaree University of Technology  
Academic Year 2020**

การศึกษาเชิงแม่เหล็กสารที่ตอบสนองต่อแสงด้วยการวัดปรากฏการณ์เคอร์



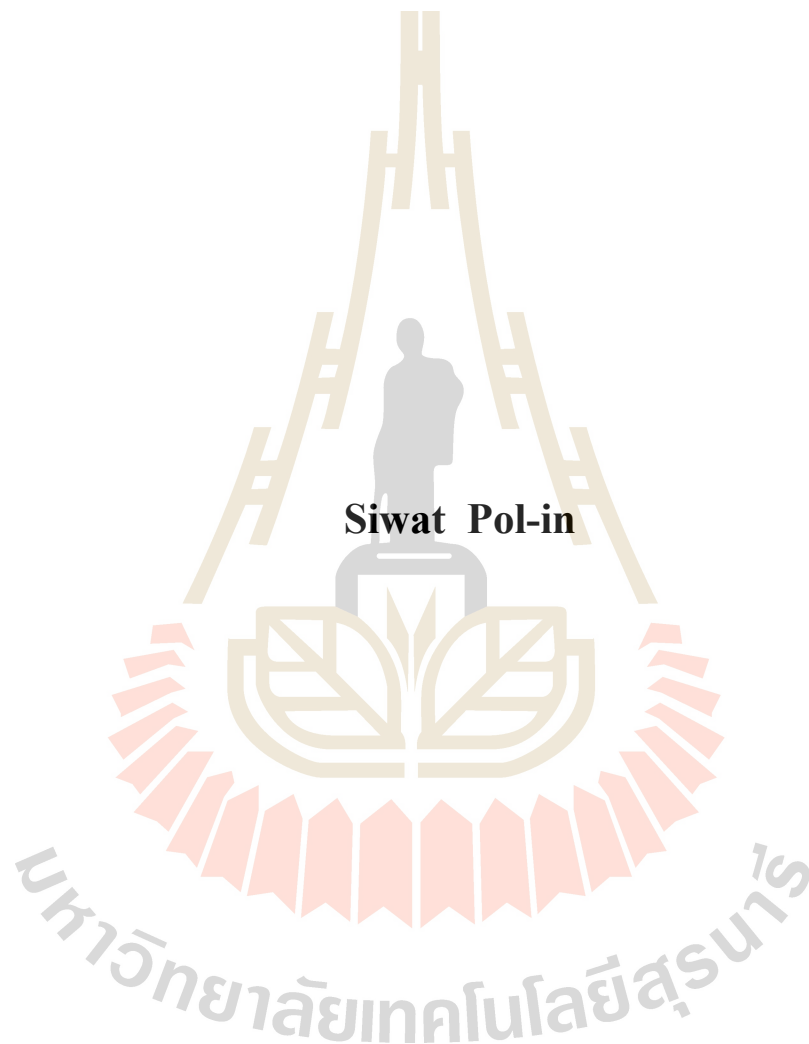
วิทยานิพนธ์นี้เป็นส่วนหนึ่งของการศึกษาตามหลักสูตรปริญญาวิทยาศาสตรดุษฎีบัณฑิต

สาขาวิชาฟิสิกส์

มหาวิทยาลัยเทคโนโลยีสุรนารี

ปีการศึกษา 2563

**MAGNETIC STUDY OF LIGHT SENSITIVE  
MATERIALS BY KERR EFFECT MEASUREMENT**

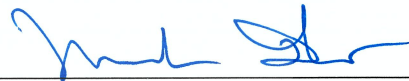


**A Thesis Submitted in Partial Fulfillment of the Requirement for the  
Degree of Doctor of Philosophy in Physics  
Suranaree University of Technology  
Academic Year 2020**

**MAGNETIC STUDY OF LIGHT SENSITIVE MATERIALS BY  
KERR EFFECT MEASUREMENT**

Suranaree University of Technology has approved this thesis submitted in partial fulfillment of the requirements for the Degree of Doctor of Philosophy.

Thesis Examining Committee



(Assoc. Prof. Dr. Panomsak Meemon)

Chairperson



(Assoc. Prof. Dr. Worawat Meevasana)

Member (Thesis Advisor)



(Assoc. Prof. Dr. Prayoon Songsiriritthigul)

Member



(Prof. Dr. Supree Pinitsoontorn)

Member



(Dr. Hideki Nakajima)

Member



(Assoc. Prof. Dr. Yupaporn Ruksakulpiwat)

Vice Rector for Academic Affairs

and Quality Assurance



(Prof. Dr. Santi Maensiri)

Dean of Institute of Science

ศิวต์ม พลอินทร์ : การศึกษาเชิงแม่เหล็กสารที่ตอบสนองต่อแสงด้วยการวัดปรากฏการณ์  
เคอร์ (MAGNETIC STUDY OF LIGHT SENSITIVE MATERIALS BY KERR  
MEASUREMENT). อาจารย์ที่ปรึกษา : รองศาสตราจารย์ ดร.วรวรรณ มีวาสนา, 143 หน้า.

วิทยานิพนธ์นี้มุ่งศึกษาสมบัติแม่เหล็กที่ตอบสนองต่อแสงด้วยการวัดปรากฏการณ์เคอร์ ผู้  
วิจัยแบ่งการศึกษาออกเป็นสองส่วนด้วยกัน คือ ส่วนที่หนึ่งมุ่งเน้นการศึกษาวัสดุ  $\text{BiFeO}_3$  ที่มี  
โครงสร้างแบบฟิล์มหลายชั้น ( $\text{BiFeO}_3/\text{SrRuO}_3/\text{SrTiO}_3$ ) เพื่อศึกษาผลของแสงความยาวคลื่นเดี่ยว ที่  
ส่งผลต่อการเปลี่ยนแปลงมุมเคอร์ในฟิล์มบางบิสมีสเฟอไรต์ การศึกษาในส่วนนี้พบสิ่งที่น่าสนใจ  
คือมุมเคอร์ของบิสมีสเฟอไรต์มีการเปลี่ยนแปลงอย่างเห็นได้ชัดภายใต้การถูกกระตุ้นด้วยแสงที่มี  
ความยาวคลื่น 405 นาโนเมตร งานวิจัยนี้ได้แสดงแนวทางการนำไปประยุกต์ที่สำคัญในการสร้าง  
สถานะเชิงแสงของสารบิสมีสเฟอไรต์ด้วยการฉายแสงเลเซอร์และใส่สนามแม่เหล็กภายนอก และ  
เพื่อทำความเข้าใจพฤติกรรมการเปลี่ยนของมุมเคอร์หลังจากการฉายแสง ผู้วิจัยได้ตรวจสอบโครงสร้าง  
สร้างทางอิเล็กทรอนิกส์ของสารในขณะที่อยู่ภายใต้แสงเลเซอร์โดยพบช่องว่างของออกซิเจนที่ซึ่งมี  
การสะสมของอิเล็กตรอนในชั้นที่อยู่ภายในช่องว่างแถบพลังงานซึ่งจะเป็นปัจจัยสำคัญเกี่ยวกับการ  
เกิดสนามไฟฟ้าภายในสารและทำให้โพลาริเซชันทางไฟฟ้าภายในบิสมีสเฟอไรต์ลดลงส่งผลให้  
มุมเคอร์เกิดการเปลี่ยนแปลง

ส่วนที่สองเป็นการรายงานผลการศึกษาค่าการตอบสนองต่อแสงที่มีความยาวคลื่น 405 นาโน  
เมตร ของฟิล์มบางนิกเกิลบนบิสมีสเฟอไรต์ ( $\text{Ni}/\text{Bi}_2\text{Te}_3$ ) ซึ่งเตรียมด้วยวิธีการตกสะสมทางเคมีแบบ  
ไร้ขั้วไฟฟ้าและศึกษาวงอิเลกตรอนที่สร้างขึ้นจากความสัมพันธ์ระหว่างค่าสนามแม่เหล็กภายนอก  
และมุมการหมุนของเคอร์ซึ่งแปรผันตรงกับความเป็นแม่เหล็กของสาร ผลการทดลองพบว่าการฉาย  
แสงส่งผลให้ค่าแมกนีไทเซชันอิ่มตัว ( $M_s$ ) มีค่าเพิ่มขึ้น และค่าสภาพบังคับ ( $H_c$ ) มีค่าลดลง อย่างเห็น  
ได้ชัด ผลจากการศึกษาสถานะประจุของ Ni ด้วยเทคนิค XANES พบว่า ในขณะที่ทำการ ฉายแสง  
เลเซอร์ธาตุนิกเกิลไม่มีประจุ แต่อาจจะมีการเคลื่อนที่ของ อิเล็กตรอน ระหว่างธาตุนิกเกิล (Ni) กับ  
ธาตุเทลลูเรียม (Te) และอาจเกิดพันธะแบบอ่อน ( $\text{Ni}-\text{Te}$ ) ซึ่งส่งผลต่ออันตรกิริยาแม่เหล็ก แบบเฟอร์โร

สาขาวิชาฟิสิกส์  
ปีการศึกษา 2563

ลายมือชื่อนักศึกษา

ลายมือชื่ออาจารย์ที่ปรึกษา



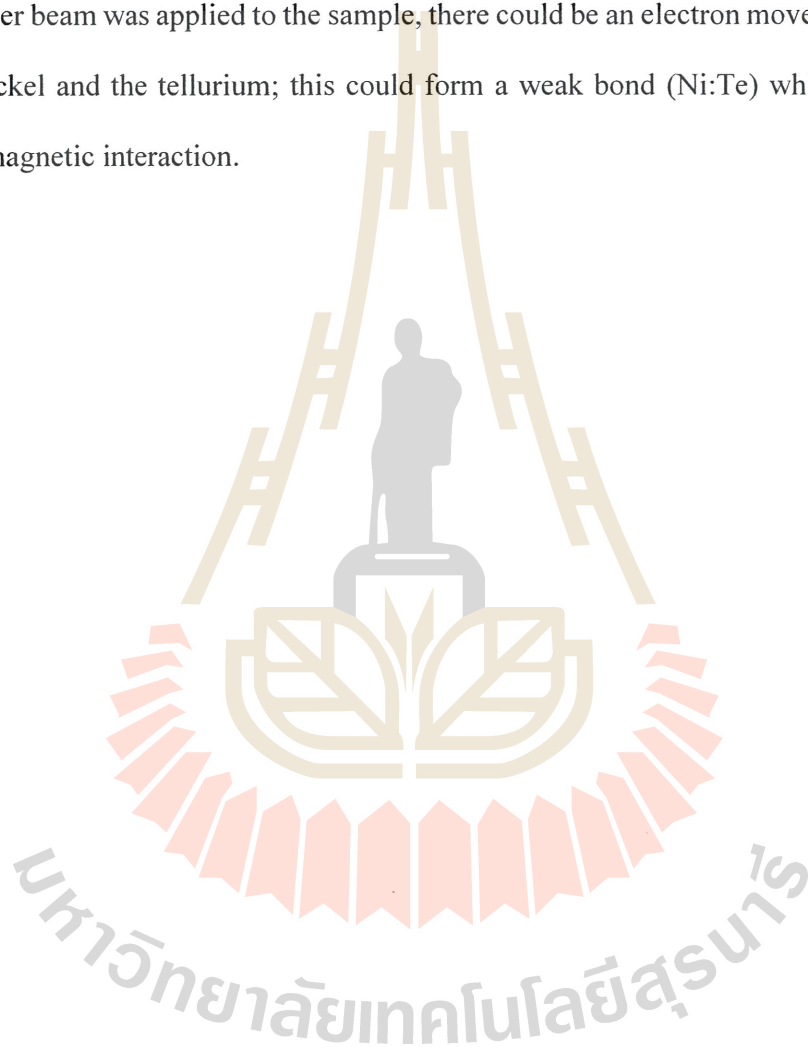
SIWAT POL-IN : MAGNETIC STUDY OF LIGHT SENSITIVE  
MATERIALS BY KERR EFFECT MEASUREMENT. THESIS ADVISOR :  
ASSOC. PROF. WORAWAT MEEVASANA, Ph.D. 143 PP.

BiFeO<sub>3</sub>/ MULTIFERROIC/MAGNETO OPTICAL KERR EFFECT/ELECTRONIC  
STRUCTURE/PHOTOEMISSION SPECTROSCOPY

This thesis aims to study magnetic properties that respond to light by measuring the Kerr effect. The researcher divided the study into two parts: part one focused on BiFeO<sub>3</sub> material with a multi-layer film structure (BiFeO<sub>3</sub> / SrRuO<sub>3</sub> / SrTiO<sub>3</sub>) to study the effect of single-wavelength laser irradiation on the change in Kerr angle of bismuth ferrite heterostructure. Interestingly, this part of the study found when the bismuth ferrite's Kerr angle rotation was significantly altered under illumination of laser with a wavelength of 405 nm. It is applied to build the optical Kerr state of bismuth ferrite by irradiating laser and applying an external magnetic field. Moreover, to understand the changing behavior of the hysteresis curves after irradiation. We examined the electronic structure of the substance while it was under the laser beam and found an electronic state which arose from oxygen vacancy. The accumulation of electrons in the state within the energy bandgap may be an essential factor which cause the electric field inside BiFeO<sub>3</sub> and reduce electrical ferroelectric polarization, resulting in a change in the rotation of Kerr angle.

The second part is a report on the light response study of 405nm of a nickel film on bismuth telluride (Ni/Bi<sub>2</sub>Te<sub>3</sub>) prepared by an electroless chemical deposition method. The magnetic hysteresis loop was studied to investigate the relation between

the external magnetic field and the Kerr rotation, which is proportional to the magnetism of the substance. The results showed that the light irradiation increased the saturation magnetization ( $M_s$ ) value. Moreover, the coercivity ( $H_c$ ) is significantly decreased. The results from In-situ XANES study of Ni charge state showed that while the laser beam was applied to the sample, there could be an electron movement between the nickel and the tellurium; this could form a weak bond (Ni:Te) which affects the ferromagnetic interaction.



School of Physics

Academic Year 2020

Student's Signature

Advisor's Signature


## ACKNOWLEDGMENTS

My thesis writing and research could not have happened without many individuals' assistance and support. First of all, I would like to express my sincere gratitude and appreciation to Prof. Dr. Worawat Meevasana, my advisor, for all his impressive help over the past five years, for the scientific discussions, and for giving me the opportunity to learn and do research in the Meevasana group and for the excellent suggestion when there are many problems with the research. His kind endurance, well support, and confidence were momentous in providing a familiarly environment for completing this thesis's final step.

I appreciate the guidance from Assoc. Prof. Dr. Panomsak Memon and Assoc. Prof. Dr. Prayoon Songsiriritthigul, as my thesis committee, was providing valuable comments and information during my thesis examination. I want to express my gratitude to Dr. Hideki Nakajima for providing assistance in using PES at BL3.2a, SLRI, and for his assistance as an examination committee. I would like to thank all staff at the School of Physics, Institute of Science, Suranaree University of Technology, to give me the useful information and inspire me to do the research. Special thanks go to Mrs. Phenkhae Petchmai, who helps me to complete all documents.

I appreciate all members of the BL3.2a staff, which includes Dr. Ratchadaporn Supruangnet, Mr. Surachet Rattanasuporn, Mr. Watcharapon Jenpiyapong and Mr. Siwat Chumsuk, who work at the center of scientific and technological equipment for their comments and discussion on my work. I also appreciate the person who always helps. It is impossible to say thank you to all my fellow graduate students here, who

were the well-wishes supporter during my Ph.D. study, for all the special moments we had together. Finally, I would like to thank my warm family for always standing by me and encourage me to endeavor to accomplish this research.

Siwat Pol-in



# CONTENTS

	<b>Page</b>
ABSTRACT IN THAI.....	I
ABSTRACT IN ENGLISH .....	II
ACKNOWLEDGMENTS .....	IV
CONTENTS.....	VI
LIST OF TABLES.....	X
LIST OF FIGURES .....	XI
LIST OF ABBREVIATIONS.....	XIX
<b>CHAPTER</b>	
<b>I INTRODUCTION.....</b>	<b>1</b>
1.1 Background and motivation .....	1
1.2 Research objective/Purposes of the study .....	3
1.3 Scope and limitations .....	3
1.4 Anticipated outcomes .....	4
1.5 Outline of thesis.....	4
<b>II THEORETICAL BACKGROUND.....</b>	<b>6</b>
2.1 Brief overview of magnetic properties in materials.....	6
2.1.1 Magnetic domains .....	6
2.1.2 Magnetic interaction.....	7
2.1.3 Exchange energy .....	8

## CONTENTS (Continued)

	<b>Page</b>
2.1.4 The magnetostatic energy .....	9
2.2 Magneto optic effect.....	10
2.2.1 Introduction to magneto optic effect .....	10
2.2.2 Macroscopic point of view of magneto optic effect.....	11
2.2.3 Waves and polarization of light – the Jones calculus.....	11
2.2.4 Microscopic model for optical response.....	17
2.2.4.1 The classical approach-Drude behavior and Lorentz model ...	17
2.2.4.2 Quantum mechanical derivation of MOKE.....	23
2.3 Photoemission spectroscopy.....	26
2.3.1 Photoelectric effect.....	27
2.3.2 The photoemission process.....	27
2.3.2.1 Three-step model.....	27
2.3.2.2 One-step model.....	28
2.3.2.3 Photoemission theory .....	30
2.3.3 Core level spectroscopy.....	34
2.3.4 Charging effect .....	36
2.3.5 Reciprocal lattice .....	38
2.3.6 Spin-orbit interaction.....	41
2.4 Single crystal x-ray diffraction: Laue method.....	41
2.5 Bismuth ferrite (BiFeO <sub>3</sub> ).....	44

## CONTENTS (Continued)

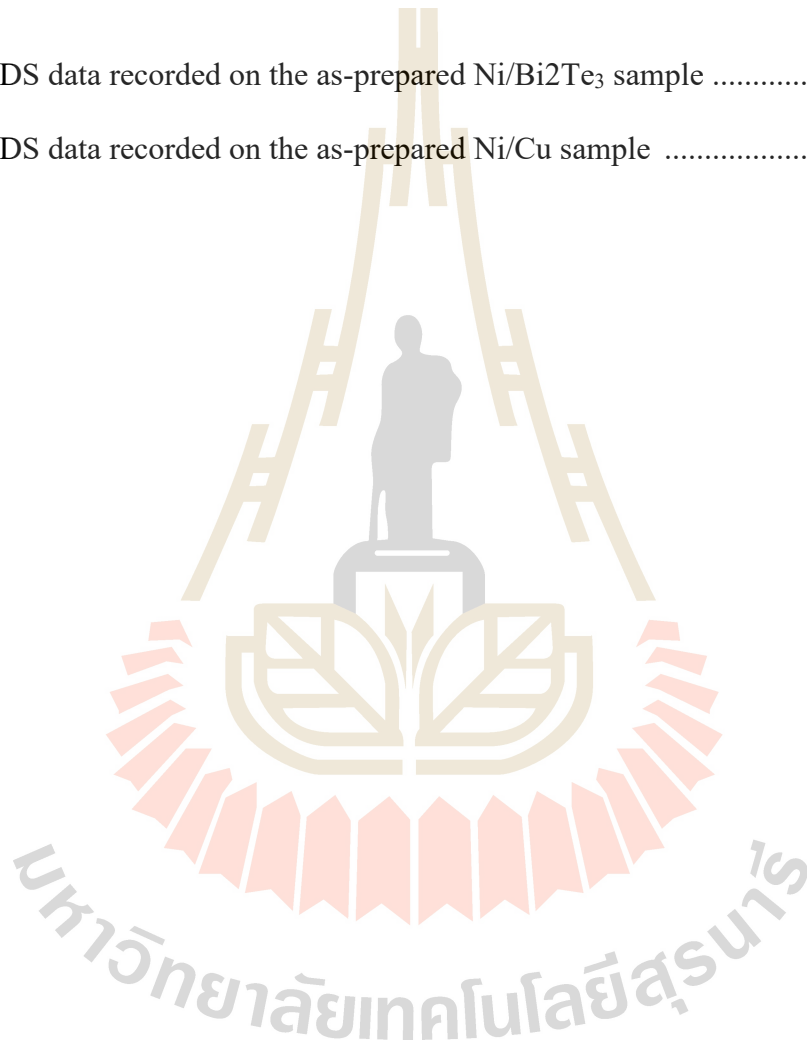
	<b>Page</b>
2.5.1 Crystal structure of BiFeO <sub>3</sub> .....	45
2.5.2 Magnetism of BiFeO <sub>3</sub> .....	46
2.5.3 Magnetic symmetry and spin cucloid of BiFeO <sub>3</sub> .....	47
<b>III RESEARCH METHODOLOGY .....</b>	<b>48</b>
3.1 Magneto-optical Kerr effect magnetometer (MOKE) set up .....	49
3.2 Sample preparation technique .....	55
3.2.1 Thin film fabrication.....	55
3.2.2 Molecular beam epitaxial (MBE).....	57
3.2.2.1 Deposition process of MBE .....	59
3.2.3 RF magnetron sputtering .....	60
3.2.4 Electroless-deposition (ELDP).....	63
3.3 Electrochemical measurement with cyclic voltammetry.....	65
3.4 Scanning electron microscopy (SEM).....	68
3.5 X-ray diffraction (XRD).....	70
3.6 In-situ X-ray absorption spectroscopy.....	71
<b>IV STUDY OF KERR ROTATION IN BISMUTH FERRITE (BIFEO3) .....</b>	<b>76</b>
4.1 Experimental investigation of MOKE.....	77
4.1.1 Magnetic hysteresis loop (M-H)-measurement.....	78
4.2 Characterization of the BiFeO <sub>3</sub> /SrRuO <sub>3</sub> /SrTiO <sub>3</sub> heterostructure.....	81
4.2.1 Details of BiFeO <sub>3</sub> /SrRuO <sub>3</sub> /SrTiO <sub>3</sub> fabrication.....	81

## CONTENTS (Continued)

	<b>Page</b>
4.2.2 Crystal structure characterization by X-ray diffractometer (XRD) ....	81
4.2.3 Surface structure analysis by atomic force microscope (AFM).....	83
4.2.4 Piezoresponse force microscope (PFM) analysis .....	85
4.3 Magneto-optical Kerr effect (MOKE) measurement.....	87
4.4 Summation of magnetic and electric (laser) fields via Kerr angle .....	92
4.5 In situ Kerr rotation measurement under external electric field and laser ...	93
4.6 Relaxation of photo-induced Kerr rotation in BiFeO <sub>3</sub> .....	97
4.7 In situ photoemission spectroscopy .....	101
<b>V THE STUDY OF PHOTO-ENHANCED IN Ni/Bi<sub>2</sub>Te<sub>3</sub>.....</b>	<b>106</b>
5.1 Electroless deposition of Ni on Bi <sub>2</sub> Te <sub>3</sub> .....	107
5.2 Morphology characterization .....	109
5.3 Chemical composition analysis by EDX .....	112
5.4 Magneto-optical Kerr effect measurement of Ni/Bi <sub>2</sub> Te <sub>3</sub> .....	113
5.4.1 Light-induced changes in coercivity.....	113
5.5 Ultraviolet photoemission spectroscopy (UPS) analysis of Ni/Bi <sub>2</sub> Te <sub>3</sub> .....	115
5.6 In-situ X-ray Absorption Spectroscopy (XAS) .....	118
<b>VI CONCLUSION .....</b>	<b>122</b>
REFERENCES .....	124
APPENDIX.....	138
CURRICULUM VATAE .....	143

## LIST OF TABLES

Table	Page
1 EDS data recorded on the as-prepared Ni/Bi <sub>2</sub> Te <sub>3</sub> sample .....	112
2 EDS data recorded on the as-prepared Ni/Cu sample .....	112



## LIST OF FIGURES

<b>Figure</b>	<b>Page</b>
2.1 Example of magnetic domains. The arrows indicate the direction of the magnetization .....	6
2.2 Rotation of the magnetization from one domain to the other domain through a wall. a) represents a Bloch wall whereas b) is a Néel wall .....	7
2.3 The vectorial diagram of polarization and their Jones vector. the upper row diagrams show a linearly polarized wave along the x-axis, a linear polarized wave with an azimuth angle $\theta$ relative to the x-axis, and a left circularly polarized wave. Diagram in the lower row shows the linearly polarized wave perpendicular to the wave in the upper row .....	14
2.4 On the left hand-side, the diagram shows an elliptically polarized wave with the ellipticity is $\epsilon$ and $\theta=0$ . On the right hand-side the same ellipse is inclined at an angle $\theta$ with respect to the positive x-axis .....	16
2.5 Illustration of three-step and one-step model crucially use for describing the possible photoemission process (Hufner, 1995) .....	29

## LIST OF FIGURES (Continued)

Figure	Page
2.6	a) Mirror plane emission from a $d_{x^2-y^2}$ orbital indicates the opposite sign of initial wave function from each direction. b) Sketch of the optical transition between atomic orbital with different angular momentum results to the intensity variation of outgoing electron. c) Calculated photoionization-cross-section of Cu 3d and O 2p as a function of photon energy (Damascelli, 2004) ..... 35
2.7	The standard 'Universal' electron-mean-free-path in solids as a function of kinetic energy (Damascelli, 2004)..... 36
2.8	a) Fermi edge broadening and the Fermi edge shift of gold as a function of sample current (Zhou et al.,2005)..... 37
2.9	a) A unit cell with three basis vectors $a$ ; $b$ , and $c$ with the respected angles of $\alpha$ , $\beta$ , and $\gamma$ . b) Illustration of reciprocal lattice vectors, $a^*$ , $b^*$ , and $c^*$ relating to the real space vectors ..... 40
2.10	Geometrical relationship between the position of the Laue spots and the reflecting plane (Kedesy, 1954) ..... 43
2.11	Crystal structure of BiFeO <sub>3</sub> shown (a) the pseudocubic-[110], (b) the pseudocubic-[111]-polarization, and (c) a isometric view of the structure. (d) G-type antiferromagnetic ordering and formation of the weak ferromagnetic moment (Martin et al., 2008) ..... 44

## LIST OF FIGURES (Continued)

<b>Figure</b>	<b>Page</b>
2.12 Crystal structure of bulk BiFeO <sub>3</sub> (Lubk et al., 2009) .....	45
2.13 Antiferromagnetic structure of BiFeO <sub>3</sub> , the vector of magnetic moments point in direction along a cycloid with period of 64 nm.....	47
3.1 Illustration of the basic components needed for a MOKE setup. Light source (L), polarizers (P), a sample (S), a detector (D), and electromagnets (E). OP naturally denotes the optical path.....	49
3.2 Schematic of the basic components needed for a SMOKE setup. Light source (L), polarizers (P), a sample (S), a detector (D), and electromagnets (E). OP naturally denotes the optical path.....	50
3.3 The electronics component of MOKE .....	52
3.4 Hysteresis loop of Fe film with 5 nm thickness shows coercive field, saturation field, remnant magnetization and saturation magnetization .....	54
3.5 The thin film general growth model .....	56
3.6 A molecular beam epitaxy growth chamber .....	57
3.7 Schematic figure of effusion cells currently used in MBE systems: (a) Knudsen Knudsen cell; (b) Two stage Cracking effusion cell (Courtesy of Prof. Klaus H.Ploog).....	58
3.8 Schematic of the surface processes occurring during MBE growth .....	59
3.9 Schematic of sputtering process.....	60
3.10 RF diode sputtering system.....	62

## LIST OF FIGURES (Continued)

Figure	Page
3.11 Schematic of electroless nickel deposition (a) and photography of electroless deposition set up (b).....	64
3.12 Cyclic voltammogram of redox reaction .....	66
3.13 The interaction of primary incident electrons with a sample. (a) Signals generated by electron-matter interactions (b) Absorption of SE, BSE, and X-rays by inelastic scattering within the interaction volume, determine the depth of electron escape (Inkson, 2016).....	69
3.14 Electron-induced X-ray emission. (a) Characteristic X-ray emission. Characteristics X-ray are emitted when outer shell electron moves to fill the empty electron energy level emptied by the secondary electron. (b) Schematic figure of an energy dispersive X-ray (EDX) spectrum of characteristic X-rays at several specific energies (Inkson, 2016).....	69
3.15 Bragg diffraction by crystal planes .....	71
3.16 Schematic processes stimulated by X-ray including photoemission, X-ray fluorescence and Auger electron emission where $h\nu$ is incident photon, $E_{ae}$ is energy of outgoing Auger electron ( $E_{ae} = E_K - E_L - E_M$ ), $E_p$ is energy of outgoing photoelectron or relaxation ( $E_p = h\nu - E_K -$ $E_M$ ), $E_{erf}$ is energy of outgoing fluorescence photon ( $E_{xrf} = E_K - E_M$ ) and $E_K$ , $E_L$ and $E_M$ are the energies of the K, L, and M orbitals.....	72
3.17 XAS spectrum of L3-edge measured in transmission mode.....	73

## LIST OF FIGURES (Continued)

Figure	Page
3.18 XAS measurement system at XAS beamline (BL-5.2), Synchrotron Light Research Institute (SLRI) of Thailand .....	75
4.1 Schematic illustration of longitudinal magneto-optical kerr effect measurements. The inset is photograph of L-MOKE.....	77
4.2 Field dependence of the magnetization $M$ in $B$ parallel to surface of Fe films in the external applied magnetic field -200G to 200G (a) and a partial enlarged curve (b) .....	78
4.3 Normalized hysteresis loops of film at the angles of $45^\circ$ , $53^\circ$ , $60^\circ$ , $90^\circ$ orientation.....	79
4.4 XRD spectra of BFO/SRO/STO (001) mono domain film.....	81
4.5 Surface morphology of the heterostructures. AFM images showing smooth surface morphology of both as-grown BiFeO <sub>3</sub> (RMS roughness $\sim 4.0$ nm). Scale bar equal to $1 \mu\text{m}$ . Step bunching occurs to accommodate structural relaxation during BiFeO <sub>3</sub> growth on miscut SrTiO <sub>3</sub> substrates in area $8 \times 8 \mu\text{m}$ (a), $4 \times 4 \mu\text{m}$ (b), and 3D image of morphology. (c).....	84
4.6 PFM image showing polarization domain structures of (001)-oriented BiFeO <sub>3</sub> film.....	85
4.7 Schematics of MOKE experiment configurations for magnetic field applied parallel to the surface .....	87

## LIST OF FIGURES (Continued)

Figure	Page
4.8 Magneto-optical hysteresis loop measured for BFO/SRO/STO film, measured in external range -1600G to 1600G at RT .....	87
4.9 Angle of analyzer setting(a) right (b) left of Kerr angle measurement under ultraviolet illumination.....	89
4.10 Restoration of Kerr rotation variation after turning off UV laser.....	90
4.11 (a) Utilization of Kerr angle rotation. (b) magneto optical coupling at constant external magnetic field -200G and 200G .....	92
4.12 Schematics of MOKE experiment configurations for magnetic field applied perpendicular to the BFO/SRO/STO surface (a). electric-optic coupling of BFO/SRO/STO measured Kerr angle (b) .....	93
4.13 The time resolve Kerr rotation of BFO which respond to the external electric field at different external electric field.....	94
4.14 The Kerr rotation behavior in terms of four different power density ( $\leq 140 \text{ mW/mm}^2$ ) in time resolve Kerr rotation of BFO respond to the ultraviolet stimuli at different power density.....	95
4.15 PFM of BFO/SRO/STO under light and dark condition .....	96
4.16 (a)-(g) show time-resolved Kerr rotation with alternatively laser-on and off conditions upon uv illumination with $70 \text{ mW/mm}^2$ to $600 \text{ mW/mm}^2$ power density on for 300s.....	98

## LIST OF FIGURES (Continued)

Figure	Page
4.17 Schematic diagram model of photo- induce depolarization in macroscopical perspective.....	99
4.18 Relaxation of Kerr rotation as a function of time (a), remanence Kerr rotation depending on laser power density (b).....	101
4.19 Evolution of the valance band (VB) spectra of BFO mono domain film measured from the initial surface to the exposed surface. The shift in the binding energy of $O_{2p}$ valance electrons state while the $C_{1s}$ (inset) is located at the same energy.....	102
4.20 XPS spectra for valance of the samples and the Gaussian fitting, upon laser irradiation time is a) 0s, b) 10s, c) 20s, d) 30s, e) 60s, and f) 90s, respectively.....	104
5.1 Cyclic voltammogram of $Bi_2Te_3$ in 1 mM HCl (curve 1) and 1mM HCl/1 mM $NiCl_2$ (curve 2 to 6) solutions, $dE/dt = 30 \text{ mV s}^{-1}$ .....	108
5.2 Chronoamperometry of Ni electroless deposition on $Bi_2Te_3$ at $V_{bias} = -0.86V$ .....	109
5.3 SEM of surface morphologies of (a) $Bi_2Te_3$ substrate before Ni Electrodeposition, (b)-(c) $Ni/Bi_2Te_3$ after Ni electrodeposition for 60s and 300s, (d) $Ni/Cu$ after electrodeposition for 60s, and (e) Cross-sectional SEM of electroplated Ni layers with 300s deposition time on (e) $Bi_2Te_3$ , and (f) Cu substrate.....	110

## LIST OF FIGURES (Continued)

Figure	Page
5.4 Chemical composition analysis of as-prepared Ni/Bi <sub>2</sub> Te <sub>3</sub> and Ni/Cu shown in SEM image. (a) SEM image of as prepared Ni/Bi <sub>2</sub> Te <sub>3</sub> sample. (b) The SEM image of Ni/Cu sample. (c) Cross-section SEM image of Ni/Bi <sub>2</sub> Te <sub>3</sub> sample. Table 1 EDS data of Ni/Bi <sub>2</sub> Te <sub>3</sub> sample. Table 2 EDS data of Ni/Cu sample.....	112
5.5 Magnetization versus applied magnetic fields as measured in the dark and light states of Ni/Bi <sub>2</sub> Te <sub>3</sub> with deposition time 60s.....	113
5.6 Magnetization versus applied magnetic fields as measured in the dark and light states of Ni/Cu with deposition time 60s.....	115
5.7 UPS spectra of Ni/Bi <sub>2</sub> Te <sub>3</sub> sample. (a),(b),(c) and (d) Bi5d, Te4d, O1s and Ni3p spectra, respectively .....	117
5.8 In situ Ni L-edge fluorescence measurement setup (a) schematic and, (c) the photograph of measurement system setup.....	118
5.9 In situ Ni L-edge fluorescence XANES spectra under dark and light illuminations .....	119
5.10 Differentiation of Ni K-edge XANES for pure Ni foil(black), Ni/Bi <sub>2</sub> Te <sub>3</sub> sample under UV laser illumination .....	120
5.11 FT EXAFS structures of Ni/Bi <sub>2</sub> Te <sub>3</sub> electroless deposition at 60s under dark and light illumination.....	121

## LIST OF ABBREVIATIONS

2DEG	Two-Dimensional Electron Gas
BE	Binding energy
CV	Cyclic voltammetry
EIS	Electrochemical impedance spectroscopy
eV	Electron volt
EXAFS	Extended X-ray absorption fine edge structure
EDS	Energy Dispersive spectroscopy
FE-SEM	Field-emission Scanning electron microscopy
HER	Hydrogen evolution reaction
OER	Oxygen evolution reaction
PES	Photoemission spectroscopy
UHV	Ultra-high vacuum
UV	Ultraviolet light
UV-vis	UV-Visible spectroscopy
VBM	Valence band maximum
XANES	X-ray absorption near edge structure
XAS	X-ray absorption spectroscopy
XPS	X-ray photoelectron spectroscopy
XRD	X-ray diffraction

# CHAPTER I

## INTRODUCTION

### 1.1 Background and motivation

The possibilities and methods of using a non-magnetic field to control the magnetism of material are widely interesting topic because of potential impact to information technology. Instead of using electric currents or electric fields, the new idea of using light to enhance or control magnetism may be possible method (Chu et al., 2008). It has been reported about using ultrashort laser pulses to manipulated magnetic properties (including sub-picosecond magnetization reversal) are possible and consume low energy (Lambert et al., 2014; Stanciu et al., 2007). Optical generated coherent magnetic precession (Kim et al., 2015) and laser-induced spin reorientation (Kalashnikova et al., 2015) was studied. In fact, according to literature review, some group studied the spin states modification by nonpolarized light for a long time. Moreover, the magnetic permeability can be modified under infrared radiation in silicon-doped yttrium iron garnet at 20K (Teale and Temple, 1967) which is caused by the charge transfer from  $Fe^{2+}$  to  $Fe^{3+}$ .

The photo-induced ferromagnetic properties was investigated in p-(In,Mn) As/GaSb and metal-organic assemblies, at low temperatures (Ohkoshi et al., 2011; Ohkoshi et al., 2006). They described this effect using model of the carrier-mediated ferromagnetic interaction of the Mn ions which is enhanced by light (Munekata, 2005).

The room temperature ferromagnetism in oxide materials such as undoped ZnO (Banerjee et al., 2007) caused by the oxygen defects, especially singly ionized oxygen vacancies (Liu et al., 2013; Zhan et al., 2012). Furthermore, nonpolarized ultraviolet or violet light can control ferromagnetic properties of ZnO film on Pt substrate at room temperature. This effect was described that the oxygen vacancies and the built-in electric field across the heterostructured ZnO/Pt might be main determinant of the light-induced ferromagnetic variation. (Xie et al., 2017)

Moreover, there is one possibility which ferromagnetism can be controlled via magnetoelectric and photovoltaic effect. Many research efforts on magnetoelectric effects in recent years (Eerenstein et al., 2006a; Spaldin and Fiebig, 2005) have motivated the research of light induced magnetism in many materials, Bismuth ferrite ( $\text{BiFeO}_3$ ) get attention because of it is compound with ferroelectricity together with antiferromagnetism at room temperature. In the viewpoint of applications, BFO has a great potential in spintronics devices namely using an electric field to control a magnetization via the magnetoelectric effect.

Classical spintronic device are based on metallic materials which can not interact with photons. Functionalities with light require materials that have a bandgap which photons can generate charge carriers such as semiconductors and Schottky barriers. Therefore, multiferroic materials also offer this possible opportunity along with magnetoelectricity, which couples magnetism to ferroelectricity and also elasticity. Moreover, because of the material possess the ferroelectricity are insulators, it can be enhanced the photoconduction or photovoltaic effects under light illumination (Choi et al., 2009; Yang et al., 2010). According to literature review, it was found that visible-

light can induce the dimensional variation of  $\text{BiFeO}_3$  crystals at room temperature, was called the light-induced photostrictive effect which is in the order of  $10^{-5}$  with response times below 0.1 s. These reported results imply that in multiferroic material, magnetism can be induced by light, but until now, coupling of light with magnetism has been elusive, although magnetoelectric effect is a well-known property of many materials.

In this work, we intend to focus on the observation and study of a substantial light-induced change in the magnetic properties of light sensitive materials at room temperature.

## **1.2 Research objective/Purposes of the study**

In this work, we aim to study the origin of change of magnetism in light sensitive material. The objectives listed as follows.

- (I) To set up magneto-optical Kerr effect measurement system (MOKE)
- (II) To study the magnetic property of the light sensitive materials using MOKE
- (III) To investigate the application of light/ electric field enhance magnetism relative to the Fermi level ( $E_F$ ) in the photoemission measurements.

## **1.3 Scope and limitations**

(I) Install magneto-optical Kerr measurement kit from the existing devices. To be able to measure the longitudinal magnetic phenomenon of volumetric and film samples or Kerr angle rotation in non-magnetic materials.

(II) Study the effect of laser on Kerr angle rotation in  $\text{BiFeO}_3$

(III) Study the laser enhanced magnetism in  $\text{Ni/Bi}_2\text{Te}_3$  and report the study result.

## 1.4 Anticipated outcomes

- (I) To successfully set up the L-MOKE.
- (II) To present potential ways of utilization of Kerr rotation in materials.
- (III) To understand the fundamental of light-induced magnetism/Kerr angle rotation.

- (IV) Publications in ISI journals.

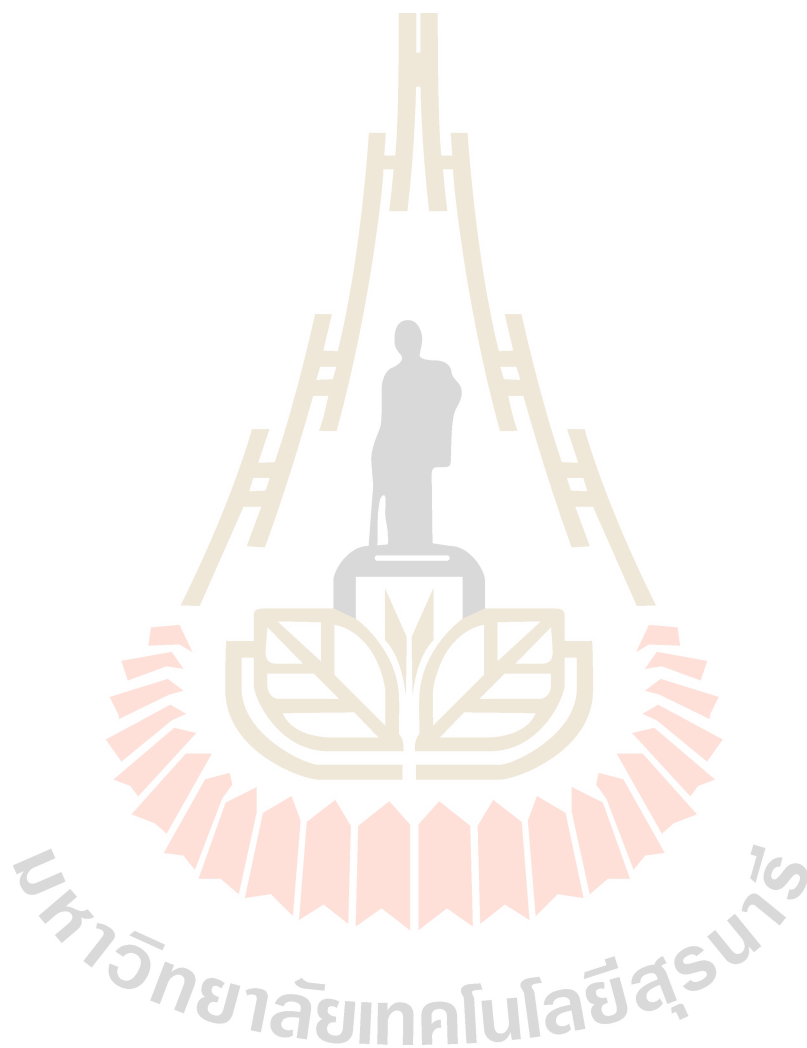
## 1.5 Outline of thesis

This thesis is organized as following. The Chapter II describes a brief theoretical concept overview of magneto optical Kerr effect, technical background of photoemission spectroscopy, Bismuth ferrite ( $\text{BiFeO}_3$ ) have also been demonstrated in this chapter. In chapter III, the technical details of Magneto-optical Kerr effect magnetometer (MOKE) set up will be discussed. The overview of sample preparation technique is described with an emphasis on electroless deposition technique which was setup to prepared the magnetic film. Moreover, all measurement techniques used in this work are also summarized in this chapter.

Chapter IV represents my work on  $\text{BiFeO}_3$ . In this chapter, the effect of laser irradiation on the Kerr angle rotation will be presented. Application to create a substance that contains the state of Kerr rotation has been proposed. Furthermore, the experimental observation of electronic structure and the implication of electric field inside substance will be discussed in this chapter.

Chapter V represents my work on  $\text{Ni/Bi}_2\text{Te}_3$ . In this chapter, the effect of laser enhanced magnetism of Ni film on  $\text{Bi}_2\text{Te}_3$  substrate will be reported. The experimental results of morphology, chemical concentration analysis and electronic structure will be

reported. Finally, conclusions and suggestions are described, and future works are proposed in Chapter VI.



## CHAPTER II

### THEORITICAL BACKGROUND

#### 2.1 Brief overview of magnetic properties in materials

##### 2.1.1 Magnetic domains

Magnetic materials were of interest to researchers for centuries, until in the 19th century, theories were developed that attempted to explain their magnetic properties on a macro scale. Weiss was the first to question what happened at the microscopic level scale. He hypothesized that the magnetization inside the material is irregular. But, on the contrary, it consists of regions of self-magnetization,  $M_i$  (Figure 2.1). organized in such a way that the resulting magnetic moment  $M$  vanishes, i.e.  $\sum_i M_i$  is zero (for ferromagnetic materials). The magnetic moments that lie in each region cancel each other out.

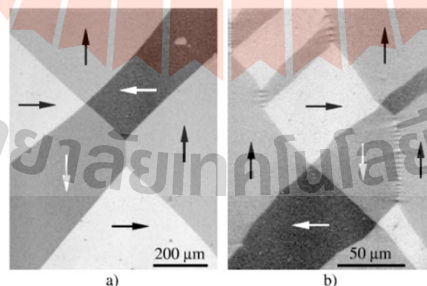


**Figure 2.1** Example of magnetic domains. The arrows indicate the direction of the magnetization.

These areas are named magnetic domains. They are separated by the wall, which is called Bloch or Néel walls depending on material properties. Within the

domain wall, the magnetization rotates from the direction of magnetization within the first domain to the second domain orientation. For the Bloch wall, magnetization rotated from the wall plane. In contrast, for the Néel wall, it is rotated in the plane, as shown in Figure 2.2. To get a deeper understanding of the formation or even the presence of domains, we need to look at the various energies.

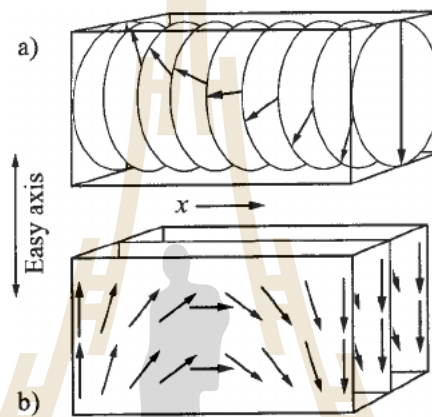


**Figure 2.2** Rotation of the magnetization from one domain to the other domain through a wall. a) represents a Bloch wall whereas b) is a Néel wall.

### 2.1.2 Magnetic interaction

The formation of magnetic domains corresponds to a minimization of the total energy of the system. The total energy is a sum of several magnetic interactions,

$$E_{tot} = E_{ex} + E_{mstatic} + E_{mca} + E_z + E_{mstriction} \quad 2.1$$

The three terms consist of,  $E_{ex}$  is the exchange energy,  $E_{mstatic}$  is the magnetostatic and  $E_{mcrystalline}$  is the magneto-crystalline anisotropy (for crystals) energy are the main energies to describe the ground state domain configuration. The first two terms will be described in detail. The magneto-crystalline anisotropy describes the tendency of the magnetization to align along the easy axis of the crystal. And  $E_{mstriction}$ , the magnetostriction energy, describes the ability of change its dimensions depending on the magnetization. Applying an external field change, the magnetization and thus the magnetostriction. And  $E_z$  is the Zeeman energy or external field energy, corresponds to the energy of a magnetized body in external magnetic field.

### 2.1.3 Exchange Energy

In deeply understanding the exchange energy, we have looked at the atomic scale. Because the magnetization is related to the behavior of spins, or roughly speaking, the magnetization is the average of spin moments direction. The exchange energy describes the interaction between neighboring spins.

$$E_{ex} = -2 \sum_{\langle ij \rangle} J_{ij} \vec{S}_i \cdot \vec{S}_j \quad 2.2$$

In this equation, the summation is over all pairs of neighboring atoms  $ij$ . And  $J_{ij}$  is the exchange parameter, for ferromagnetic coupling  $J > 0$ , mean neighboring spins tend to be aligned in the same direction. While  $J < 0$  causes antiferromagnetic coupling, which neighboring spin rotated in the opposite direction. Assume that the exchange parameter is the same from a couple of neighbors to the next one, giving  $J_{ij} = J$ . And that  $|\vec{S}_i| = S$  (1) can then be rewritten as:

$$E_{ex} = -2JS^2 \sum_{\langle ij \rangle} \cos\theta_{ij} \quad 2.3$$

Where  $\theta_{ij}$  is the angle between two spins. If  $\theta_{ij}$  is small, we can approximate it as

$\cos \theta_{ij} = 1 - \frac{\theta_{ij}^2}{2}$ . Then equation 2.2 becomes:

$$E_{ex} \approx -2JS^2 \sum_{\langle ij \rangle} 1 - \frac{\theta_{ij}^2}{2} = -2JS^2 + JS^2 \sum_{\langle ij \rangle} \theta_{ij}^2 \quad 2.4$$

The first constant term corresponding to the case where all spins are aligned is dropped. Finally the exchange energy for one couple is :

$$E_{ij} = JS^2 \theta_{ij}^2 \quad 2.5$$

#### 2.1.4 The magnetostatic energy

The magnetostatic energy can be called demagnetizing energy, magnetic dipole interaction or stray field. We use the magnetostatic energy to explain the formation of magnetic domain. This energy is made up of the wall energy  $E_w$  and the magnetostatic self-energy  $E_m$ . Since a domain of materials that possesses a magnetization  $M_i$  naturally reveal the poles at the surface of the domain, these magnetic charges generate a demagnetizing field.  $E_m$  is the integral over the volume of the sample of the product between the demagnetizing field and the magnetization. Which gives the following equation,

$$E_m = \frac{1}{2} \int_V \mu_0 \vec{H}_d \cdot \vec{M} dV \quad 2.6$$

Where  $H_d$  is the self-internal demagnetizing field,  $\mu_0$  is the vacuum permeability and  $M$  is the spontaneous magnetization. The integral of this equation is volume integral over the volume of magnetic domain, it takes into account the whole demagnetized energy which can extend outside the sample. The demagnetizing field is opposite to the magnetization  $M$ , can be written a

$$\vec{H}_d = -N\vec{M} \quad 2.7$$

where  $N$  is a demagnetizing tensor.

Then  $E_m$  is

$$E_m \propto N \quad 2.8$$

## 2.2 Magneto optic effect

The magneto-optic effect is introduced followed by establishing a model for the propagation of light in a magnetic multilayer structure. The Kerr angle is derived and a basic setup which utilizes the effect to measure hysteresis loops of metallic surface structures is presented.

### 2.2.1 Introduction to magneto optic effect

The theoretical concept of the magneto-optic effect is described in many perspectives. From a macroscopical viewpoint, ascribed by the effect to the antisymmetric off-diagonal elements of the dielectric tensor. However, to get the complete explanation of this effect, one must use quantum mechanics to describe the effect through a coupling between the electrical field of the light and the spin of the electron, namely, the spin-orbit interaction. First of all, in this section the microscopical explanation is discussed and later on a more thorough description using the dielectric function is introduced.

### 2.2.2 Macroscopical view point of magneto optic effect

Generally, we describe the optical properties of single crystal solid by complex dielectric tensor or optical conductivity tensor,  $\tilde{\epsilon}_{ij}$  and  $\tilde{\sigma}_{ij}$ , respectively. Some optical properties can be investigated using polarization modulation techniques. In section 2.2.3, we will explain the Jones calculus, which can use to calculate the transfer function of an optical system. Next, the relationship of the conductivity tensors and the components of the dielectric are shown, and the Kerr effect can be expressed in terms of the optical conductivity. We explain the electromagnetic response of a medium in the macroscopic description with the Kramers-Kronig relations and also explain the Kerr effect, the optical conductivity, and the dielectric function.

### 2.2.3 Waves and polarization- the Jones calculus

In order to generalize the derivation, our explanations are done using monochromatic waves. In the case of an anharmonic wave, it is split into monochromatic components by using Fourier analysis. Because of Maxwell's equations indicate that electromagnetic waves are transverse, consider the case of a uniform transverse-electric field plane wave which the electric field are uniform in every plane that are perpendicular to the direction of wave propagation. The electric field vector of such wave varies with respect to position  $\vec{r}$  and time  $t$  according to

$$\vec{E}(\vec{r}, t) = \vec{E}_0 e^{i(\vec{k} \cdot \vec{r} - \omega t)} \hat{e} \quad 2.9$$

where  $\vec{k}$  is the propagation (or wave) vector and  $\hat{e}$  is the polarization vector (unit vector). For example, consider a wave propagating along the z-axis in a medium (refractive index  $\tilde{n} = n - ik$ ), we get

$$\vec{k} \cdot \vec{r} = k_z z = \frac{2\pi n}{\lambda_0} z \quad 2.10$$

where  $\lambda_0$  is the vacuum wavelength,  $n$  is the index of refraction and  $k$  is the absorption coefficient. In real experiment, If we rotate the z-axis to point along the propagation vector, an arbitrary linearly polarized wave which travel along z direction, we can write Eq. 2.12 as

$$\vec{E}(z, t) = \tilde{E}_0 e^{i(kz - \omega t)} \hat{e} \quad 2.11$$

$$\vec{E}(z, t) = (\tilde{E}_x \hat{x} + \tilde{E}_y \hat{y}) e^{i(kz - \omega t)} \quad 2.12$$

For the complex phase of the field component, we represent the complex term  $e^{i\phi_x}$  and  $e^{i\phi_y}$  in Eq. 2.13 as

$$\vec{E}(z, t) = (|E_x| e^{i\phi_x} \hat{x} + |E_y| e^{i\phi_y} \hat{y}) e^{i(kz - \omega t)} \quad 2.13$$

rearrange the Eq. 2.13 as follows

$$\vec{E}(z, t) = E_{eff} (A \hat{x} + B e^{i\delta} \hat{y}) e^{i(kz - \omega t)} \quad 2.14$$

where

$$E_{eff} = \sqrt{|E_x|^2 + |E_y|^2} e^{i\phi_x} \quad 2.15$$

$$A = \frac{|E_x|}{\sqrt{|E_x|^2 + |E_y|^2}} \quad 2.16$$

$$B = \frac{|E_y|}{\sqrt{|E_x|^2 + |E_y|^2}} \quad 2.17$$

$$\delta = \phi_y - \phi_x \quad 2.18$$

We can get the Jones vector in the column matrix form as follows

$$\begin{bmatrix} A \\ B e^{i\delta} \end{bmatrix} \quad 2.19$$

This vector describes the polarization state of plane wave. For example, Jones vector

linearly polarized along x direction is  $\begin{bmatrix} 1 \\ 0 \end{bmatrix}$

linearly polarized along y direction is  $\begin{bmatrix} 0 \\ 1 \end{bmatrix}$

linearly polarized at angle  $\theta$  (measured from the x-axis) is  $\begin{bmatrix} \cos \theta \\ \sin \theta \end{bmatrix}$

Right circularly polarized is  $\frac{1}{\sqrt{2}} \begin{bmatrix} 1 \\ -i \end{bmatrix}$

Left circularly polarized is  $\frac{1}{\sqrt{2}} \begin{bmatrix} 1 \\ i \end{bmatrix}$

Consider the general direction of electric field vector in the wave front plane, at an azimuth angle  $\theta$  to the x-axis, namely the polarization of wave is in the xy plane and wave propagate along the z-axis. The exponential term in eq. 2.9 indicate the time dependence and the phase information as well as the z-component.

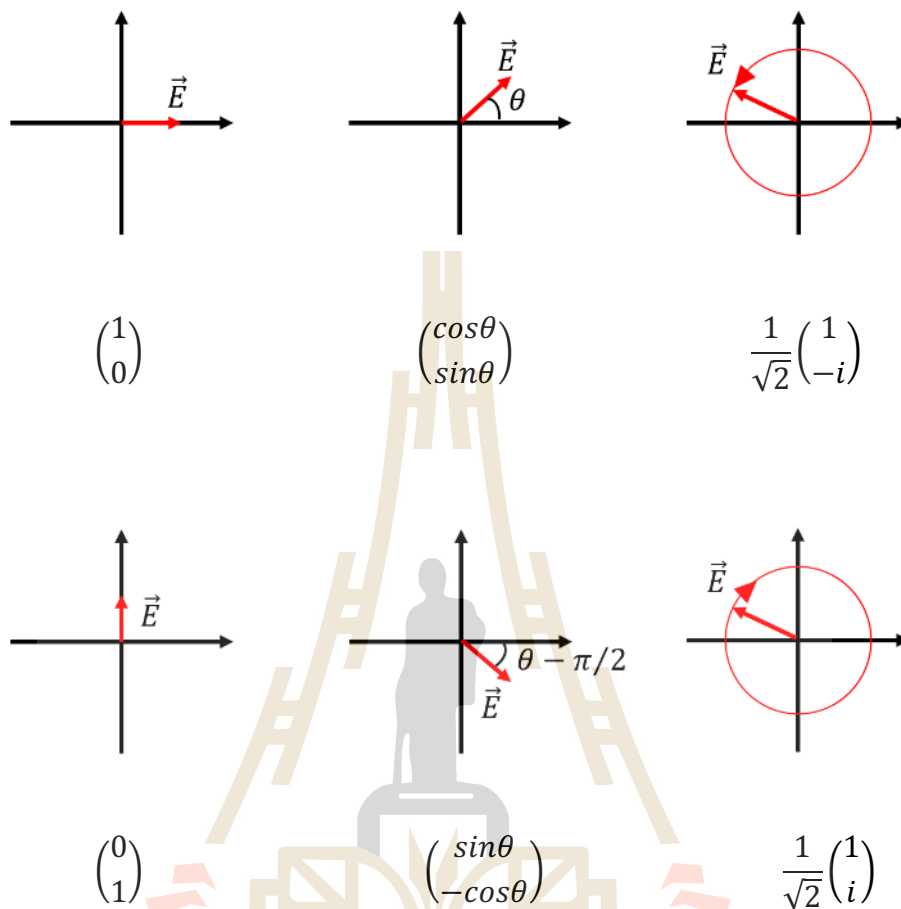


**Figure 2.3** The vectorial diagram of polarization and their Jones vector. The upper row diagrams show a linearly polarized wave along the x-axis, an inclined linear polarized wave with an azimuth angle  $\theta$  relative to the x-axis, and a left circularly polarized wave. The diagram in the lower row shows the linearly polarized wave perpendicular to the wave in the upper row.

For example, an elliptically polarized wave with ellipticity  $\epsilon$  and the major axis of ellipse is tilted at an azimuth angle  $\theta$  is described by the Jones vector as follows

$$\begin{pmatrix} \cos \theta & -\sin \theta \\ \sin \theta & \cos \theta \end{pmatrix} \begin{pmatrix} \cos \epsilon \\ i \sin \epsilon \end{pmatrix} = \begin{pmatrix} \cos \theta \cos \epsilon - i \sin \theta \sin \epsilon \\ \sin \theta \cos \epsilon + i \cos \theta \sin \epsilon \end{pmatrix} \quad 2.20$$

The Jones vector of a wave is written as follow

$$\begin{pmatrix} \vec{E}_x \\ \vec{E}_y \end{pmatrix} \quad 2.21$$

which  $E_x$  and  $E_y$  are complex amplitudes along x and y-axis, respectively. The intensity of a wave can be calculated from the sum of the squared amplitudes of the electric field component along two orthogonal direction as follow

$$I = |E_x|^2 + |E_y|^2 = E_x^* E_x + E_y^* E_y \quad 2.22$$

where  $E_i^*$  is the complex conjugate of  $E_i$

Optical elements (e.g. polarizers, modulator, sample) has its own transfer characteristics (Jones matrix). The transfer function of an optical system can be determined by Jones calculus which starting from the initial state of polarization or the incident electric wave  $\vec{E}_{in}$  multiply with Jones matrix of element to form a series of optical components  $J_1, \dots, J_n$ . The Jones vector of light passing through the optical system is determined by

$$\vec{E}_{out} = J_n \cdot J_{n-1} \cdot \dots \cdot J_1 \cdot \vec{E}_{in} \quad 2.23$$

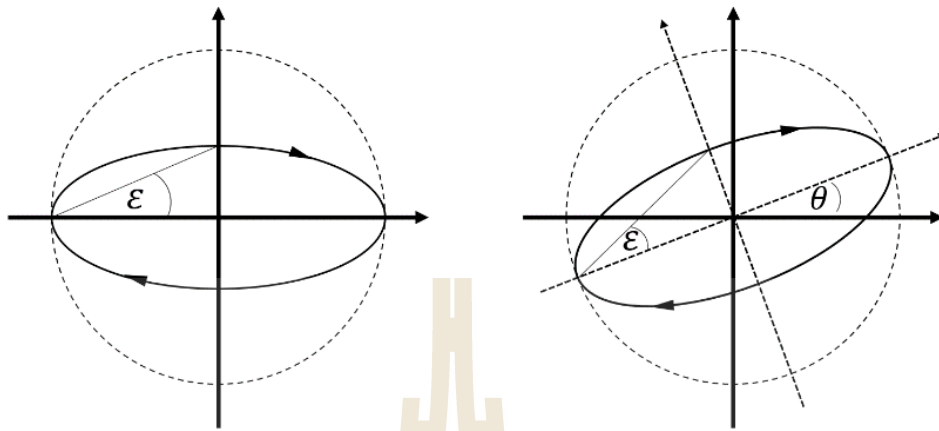


**Figure 2.4** On the left hand-side, the diagram shows an elliptically polarized wave with the ellipticity is  $\epsilon$  and  $\theta = 0$ . On the right hand-side the same ellipse is inclined at an angle  $\theta$  with respect to the positive x-axis.

The Jones matrix of a linear polarizer with its transmission axis tilted at an angle  $\theta$  to the x-axis is represented by

$$J_P = \begin{pmatrix} \cos^2 \theta & \sin \theta \cos \theta \\ \sin \theta \cos \theta & \sin^2 \theta \end{pmatrix} \quad 2.24$$

A linear retarder incurs a phase shift  $\delta$  between components of a wave polarized along its two mutually perpendicular optical axes. Jones matrix of linear retarder is written follow as

$$J_R = \begin{pmatrix} 1 & 0 \\ 0 & e^{i\delta} \end{pmatrix} \quad 2.25$$

## 2.2.4 Microscopic model for the optical response

### 2.2.4.1 The classical approach – Drude behavior and Lorentz model

Free carrier can cause a change in the Kerr rotation by changing two components of the optical conductivity tensor,  $\tilde{\sigma}_{xx}$  and  $\tilde{\sigma}_{xy}$ . In this section, the optical conductivity  $\tilde{\sigma}_{xx}$  will be derived from the free electron approximation. an incident electro-magnetic plane wave induces the current in metal. To calculate it start from the Lorentz force as

$$\vec{F} = e\vec{E} + \frac{e}{c}\vec{v} \times \vec{B} \quad 2.26$$

Which  $\vec{F}$  is acting on the charge moving under the field of radiation consisting of electric field and magnetic field. Since typically the electron velocity in metal is much less than light  $v \ll c$ , we can neglect the term originating from the magnetic field.

The understanding of traditional conductivity is based on the concept of the Drude model. This builds on the hypothesis that material consist of stationary nucleus and electrons move freely at random speeds. The electrons have periodic scattering. The mean time of the collision is called the mean free time  $\tau$  and given the mean of the distance in the collision called mean free path  $\lambda$

In this model, it is considered natural drift velocity of electron  $\vec{v}_d$  is equal to zero when there is no external electric field

$$\vec{v}_d \equiv \langle \vec{v} \rangle = 0 \quad 2.27$$

current density of electrons can be found from the equation

$$\vec{j} = n(-e)\vec{v}_d = 0 \quad 2.28$$

which  $n$  is number of electrons per volume or number density of electrons.

When an external electric field is applied, we have to consider electrons that begin to move at random speeds from time  $t = -t_0$ . In this situation, the force exerted by an electric field on an electron is equal to  $\vec{F} = (-e)\vec{E}$ . The equation for the motion of one electron at the initial time  $t = 0$  can be written as follows

$$m \frac{d\vec{v}}{dt} = (-e)\vec{E} \quad 2.29$$

the velocity of an electron can be found as follows

$$m \int_{\vec{v}_0}^{\vec{v}} d\vec{v} = (-e)\vec{E} \int_{-t_0}^0 dt \quad 2.30$$

$$m(\vec{v} - \vec{v}_0) = (-e)\vec{E}(0 - (-t_0)) \quad 2.31$$

$$\vec{v} = \vec{v}_0 - \frac{e\vec{E}t_0}{m} \quad 2.32$$

To find the drift velocity, all the figures must be averaged. Taking into account the probability that electrons begin to move without scattering until that time  $t = 0$  There is the following probability  $P(t_0) \propto e^{-t_0/\tau} = e^{-t_0/\tau}/\tau$ . And in addition, the probability distribution of the initial velocity must be taken into account. Probability distribution of initial velocities is in accordance with the equation

$$\int d\vec{v}_0 P(\vec{v}_0) = 1 \quad 2.33$$

$$\int d\vec{v}_0 P(\vec{v}_0)\vec{v}_0 = 0 \quad 2.34$$

the drift velocity, which is equal to the average velocity of all electrons, can be obtained from

$$\begin{aligned}
\vec{v}_d &= \langle \vec{v} \rangle \\
&= \int d\vec{v}_0 P(\vec{v}_0) \int_0^\infty dt_0 P(t_0) \left( \vec{v}_0 - \frac{e\vec{E}t_0}{m} \right) \\
&= \int d\vec{v}_0 P(\vec{v}_0) \vec{v}_0 \int_0^\infty dt_0 P(t_0) - \int d\vec{v}_0 P(\vec{v}_0) \int_0^\infty dt_0 P(t_0) \frac{e\vec{E}t_0}{m} \\
&= 0 \cdot 1 - 1 \cdot \int_0^\infty dt_0 \frac{e^{-t_0/\tau}}{\tau} \frac{e\vec{E}t_0}{m} \\
&= -\frac{e\vec{E}}{m\tau} \cdot \int_0^\infty t_0 dt_0 e^{-t_0/\tau} \\
&= -\frac{e\vec{E}}{m\tau} \cdot \tau^2 \left( \int_0^\infty x^n dx e^{-ax} = \frac{n!}{a^{n+1}} \right) \\
&= \frac{-e\vec{E}\tau}{m}
\end{aligned} \tag{2.35}$$

hence, the current density of the electron in the event of an electric field can be found as follows

$$\vec{j} = n(-e)\vec{v}_d = n(-e) \left( -\frac{e\vec{E}\tau}{m} \right) = \frac{ne^2\tau}{m} \vec{E} \tag{2.36}$$

from this equation, the conductivity that follows Ohm's law can be expressed as follows

$$\sigma = \frac{ne^2\tau}{m} \tag{2.37}$$

we can write the equation of motion for the electron under a force as

$$\vec{p}(t + dt) = \left( 1 - \frac{dt}{\tau} \right) (\vec{p} + \vec{F}dt). \tag{2.38}$$

$$\frac{d\vec{p}}{dt} = -\frac{\vec{p}}{\tau} - e\vec{E} \quad 2.38$$

where  $\vec{p}$  is momentum of electron. This equation is called the Drude electron transport equation. The steady state solution to this equation yields a frequency-dependent conductivity follow,

$$\tilde{\sigma}(\omega) = \frac{\sigma_0}{1-i\omega\tau} \quad 2.39$$

equation 2.28 show a quantity called the Drude conductivity which can reduce to the dc conductivity,  $\sigma_0 = ne^2\tau/m$ , at  $\omega = 0$ . We can get the equation of intra-band dielectric function

$$\epsilon_{xx}^{intra} = 1 - \frac{\omega_p^2}{\omega^2 + i\omega\gamma} \quad 2.40$$

where the scattering frequency is  $\gamma = \tau^{-1}$  and unscreened plasma frequency is

$$\omega_p = \sqrt{\frac{4\pi ne^2}{m^*}} \quad 2.41$$

which  $n$  is the free carrier density and  $m^*$  is effective mass. This model can be used to explain interband transitions, which must be improved by the harmonic approximation.

In order to derive the equation of interband transition, we add a term  $\omega_0^2\vec{r}$  which describes a harmonically bound charge,  $\omega_0$  is the eigenfrequency of the system

$$m \left( \frac{d^2\vec{r}}{dt^2} + \gamma \frac{d\vec{r}}{dt} + \omega_0^2\vec{r} \right) = e\vec{E} \quad 2.42$$

Basically, there are many electrons in atom that absorb light. If  $N$  is the electron density and  $f_k$  the fraction of electrons with eigenfrequency  $\omega_k$ , we get the interband dielectric function as follows

$$\tilde{\epsilon}_{xx}^{inter} = 1 + \frac{4\pi N e^2}{m} \sum_k \frac{f_k}{\omega_k^2 - \omega^2 - i\gamma\omega} \quad 2.43$$

where  $f_k$  is an oscillator strength

Consider the free carrier which affect to  $\tilde{\sigma}_{xy}$  in diamagnetic and paramagnetic materials. However, the classical Drude theory is enough to explain the magneto-optical behavioral response of free carriers. Let's start by considering the equation of motion which has the Lorentz force and set  $\omega_0 = 0$ , that is we work with free electrons

$$m \left( \frac{d^2 \vec{r}}{dt^2} + \gamma \frac{d\vec{r}}{dt} \right) = e \vec{E} + \frac{e}{c} \frac{d\vec{r}}{dt} \times \vec{B} \quad 2.44$$

instead, this general solution into the equation

$$\vec{r}_{\pm}(t) = r_{\pm} \hat{e}_{\pm} e^{i(\omega t - \vec{k} \cdot \vec{r})} \quad 2.45$$

After substitute an electric field of the form 2.9, we obtain the dielectric function for the states of right and left-circular polarization

$$\tilde{\epsilon}_{\pm} = 1 + \frac{4\pi N e}{E_{\pm}} r_{\pm} = 1 + \frac{\omega_p^2}{\omega(-\omega + i\gamma \pm \omega_c)} \quad 2.46$$

where  $\omega_p$  is the plasma frequency and  $\omega_c = e B / m^* c$  is the cyclotron frequency. The dielectric function which depend on right and left-circular polarization also cause a splitting of the plasma edge in paramagnetic materials, which can lead to relatively large Kerr rotations of several  $10^{-3}$  degrees, as observed by Schnatterly on paramagnetic silver.

The conduction electrons of ferromagnetic metals contribute to the off-diagonal conductivity and orders of magnitudes of this effect is larger than for

paramagnetic metals. The spin-orbit interaction is an important phenomenon that drives large magneto-optic effects in ferromagnets. Spin-orbit interaction couples the spin of an electron to its momentum. As a result, the circularly polarized light wave couple to the magnetization of the materials. The skew scattering theory which was developed by Erskine and Stern and has been improved to be more accurate by Reim et al. to explain intraband transitions contribute to the off-diagonal absorption,  $\sigma_{2xy}$  with two different frequency dependencies include  $\sigma_{2xy} \propto \omega^{-1}$  and  $\sigma_{2xy} \propto \omega^{-3}$ . Erskine and Stern consider the responsive behavior of free carrier in an electric field of the form  $E_0\delta(t)\hat{x}$ . Using the relaxation-time approximation

$$-\frac{d\vec{k}}{dt} = \frac{\vec{k}}{\tau} + \frac{\vec{s} \times \vec{k}}{\tau_s} \quad 2.47$$

where  $\tau$  is a normal scattering lifetime and  $\tau_s$  is a skew scattering lifetime, which explain spin-orbit asymmetric scattering in ferromagnet metals , the off-diagonal optical conductivity is given by

$$\tilde{\sigma}_{xy} = \frac{\omega_p^2}{4\pi} \langle \sigma_z \rangle \left\{ \frac{\Omega}{(\omega - i\gamma)^2 - \Omega^2} + \frac{|\vec{P}_0|}{ev_F} \left( 1 - \frac{\omega(\omega - i\gamma)}{(\omega - i\gamma)^2 - \Omega^2} \right) \right\} \quad 2.48$$

where  $\omega_p$  is the unscreened plasma frequency,  $\Omega = \tau_s^{-1}$  is the skew scattering frequency,  $v_F$  is the Fermi velocity, and  $|\vec{P}_0|$  is the maximum electric dipole moment per unit cell. The off-diagonal conductivity is proportional to the net spin polarization

$$\langle \sigma_z \rangle = \frac{n_\uparrow - n_\downarrow}{n_\uparrow + n_\downarrow} \quad 2.49$$

If we identify  $\langle \sigma_z \rangle \Omega$  with the cyclotron frequency  $\omega_c$ , the first term in eq. 2.49 is formally identical with our result obtained from the Drude model for diamagnetic and

paramagnetic materials, i.e. for  $\omega \gg \Omega, \gamma, \sigma_{2xy}$  shows the same  $\omega^{-3}$  frequency dependence.

#### 2.2.4.2 Quantum mechanical derivation of magneto-optical Kerr effect.

The content in this section is the derivation of the optical conductivity in the quantum mechanics viewpoint. The understanding of this section should begin with the unperturbed one-electron Hamiltonian

$$H_0 = \frac{\vec{p}^2}{2m} + V(\vec{r}) \quad 2.50$$

We introduce the vector potential  $\vec{A}(\vec{r}, t)$  and the scalar potential  $\phi(\vec{r}, t)$ . And to make it convenient, we choose the Coulomb gauge, in which

$$\phi = 0 \quad \nabla \cdot \vec{A} = 0 \quad 2.60$$

To study the motion of a charge  $-e$  in an external field by replacing the electron momentum operator

$$\vec{p} \rightarrow \vec{p} + \frac{e}{c} \vec{A} \quad 2.61$$

Substituting this momentum into the unperturbed Hamiltonian and expand  $H_0$ . Neglect a quadratic term of  $\vec{A}$  and get approximately Hamiltonian as

$$H = H_0 + \frac{e}{mc} \vec{A} \cdot \vec{p} = H_0 + H_I \quad 2.62$$

where  $H_I$  is the electron-radiation interaction Hamiltonian. In the limit of small wave vector  $\vec{k}$  may approximate  $H_I$  by

$$H_I = -e\vec{r} \cdot \vec{E} \quad 2.63$$

which is known as the electric dipole approximation which does not include higher order terms (magnetic dipole, electric quadrupole, etc.) According to Fermi's Golden Rule, the electric dipole transition probability,  $\Gamma_{\alpha\beta}$ , of absorption per unit time is

$$\Gamma_{\alpha\beta} = \frac{2\pi}{\hbar} \left( \frac{e}{m\omega} \right) \left| \frac{E(\omega)}{2} \right|^2 \sum_{\vec{k}} |P_{\alpha\beta}|^2 \delta(E_{\beta}(\vec{k}) - E_{\alpha}(\vec{k}) - \hbar\omega) \quad 2.64$$

which  $|\alpha\rangle$  and  $|\beta\rangle$  are the occupied initial and empty final states of the transition, respectively.  $E(\omega)$  is the amplitude of the radiation field and  $E_{\alpha}$ ,  $E_{\beta}$  are the energies of the initial and final states, respectively.  $P_{\alpha\beta}$  is the dipole matrix element

$$|P_{\alpha\beta}|^2 = |\langle\beta|H_I|\alpha\rangle|^2 \quad 2.65$$

Consider the power loss function which is the transition probability per unit volume multiplied by the energy of the photon. This function can be expressed in the imaginary part of the dielectric function,  $\epsilon_{2xx}$  which can be seen as the link between microscopic theory and macroscopic phenomena,

$$\hbar\omega\Gamma_{\alpha\beta} = \frac{\omega|E(\omega)|^2}{8\pi} \epsilon_{2xx} \quad 2.66$$

consider the dielectric function in terms of matrix elements

$$\epsilon_{2xx} = \left( \frac{2\pi e^2}{m\omega} \right)^2 \sum_{\vec{k}} |P_{\alpha\beta}|^2 \delta(E_{\beta}(\vec{k}) - E_{\alpha}(\vec{k}) - \hbar\omega) \quad 2.67$$

according to the Kramers-Kronig relations, we obtain  $\epsilon_{1xx}$

$$\epsilon_{1xx} = 1 + \frac{4\pi e^2}{m} \sum_{\vec{k}} \frac{2}{m\hbar\omega_{\alpha\beta}} \frac{|P_{\alpha\beta}|^2}{\omega_{\beta\alpha}^2 - \omega^2} \quad 2.68$$

where  $\hbar\omega_{\beta\alpha} = E_{\beta}(\vec{k}) - E_{\alpha}(\vec{k})$ . Equation 2.48 show the sharp limit, i.e., the lift time of the excited state is infinite or the broadening (damping) term is zero,  $\gamma = 0$ . After comparing this expression with the result obtained from the Lorentz model. we get

$$Nf_k = \frac{2|P_{\alpha\beta}|^2}{m\hbar\omega_{\alpha\beta}} \quad 2.69$$

where  $Nf_k$  is the number of oscillators vibrating with frequency  $\omega_{\beta\alpha}$ . and  $f_k$  is oscillator strength of the optical transition which is proportional to the transition matrix element.

Later, consider the absorptive part of the off-diagonal conductivity,  $\sigma_{2xy}$ . We neglect the contribution of spin flip transitions and write  $\sigma_{2xy}$  as the sum of contributions from spin-up ( $\uparrow$ ) and spin-down ( $\downarrow$ ) state,

$$\sigma_{2xy}(\omega) = \sigma_{2xy\uparrow}(\omega) + \sigma_{2xy\downarrow}(\omega) \quad 2.70$$

which the contributions of spin-up states is given by

$$\sigma_{2xy\uparrow}(\omega) = \frac{\pi e^2}{4\hbar\omega m^2 V} \sum_{\alpha\beta} \{ |\langle \beta \uparrow | \pi^+ | \alpha \uparrow \rangle|^2 - |\langle \beta \uparrow | \pi^- | \alpha \uparrow \rangle|^2 \} \delta(\omega_{\alpha\beta\uparrow} - \omega) \quad 2.71$$

where the operators

$$\pi^{\pm} = \tilde{\pi}_x \pm i\tilde{\pi}_y \quad 2.72$$

are linear combinations of the kinetic momentum operator

$$\vec{\pi} = \vec{p} + \frac{\hbar}{4mc^2} \hat{\sigma} \times \vec{\nabla}V(r) \quad 2.73$$

where  $\vec{p}$  is the canonical momentum operator and  $\hat{\sigma} \times \vec{\nabla}V(r)$  represents the spin-orbit term. In principle, the contribution of spin-orbit coupling behavior could change spin-

up to spin-down state therefore be included in eq. 2.73. However, this spin-flip contribution is of second order in the spin-orbit interaction and is ignore compared to contribution of spin conservation. The spin-down states contribution is identical to Eq 2.73, but spin-up states replaced by spin-down ones. We multiply eq. 2.73 by  $\omega$  and replacing the sum over all states by an integral

$$\omega\sigma_{2xy} = \frac{\pi e^2}{4\hbar m^2} \frac{1}{(2\pi)^3} \int F_{\alpha\beta}(\omega) \delta(\omega_{\beta\alpha} - \omega) d\vec{k} \quad 2.74$$

where

$$F_{\alpha\beta}(\omega) = |\langle\beta \uparrow | \pi^+ | \alpha \uparrow\rangle|^2 - |\langle\beta \uparrow | \pi^- | \alpha \uparrow\rangle|^2 + |\langle\beta \downarrow | \pi^+ | \alpha \downarrow\rangle|^2 - |\langle\beta \downarrow | \pi^- | \alpha \downarrow\rangle|^2$$

Eq. 2.74 show that optical and magneto-optical spectra of metals consist of the contributions from intra-band and inter-band transitions.

### 2.3 Photoemission spectroscopy

Photoemission spectroscopy have unique advantage of directly probing band structure of materials which widely used to study the single crystal solid materials. The introduction of PES with the original view of photoelectric effect and some simple equations will be provided. Then, the simple physical pictures of photoemission process called three- and one- step model are presented. The intensive explanation of photoemission theory is described in section 2.4.

### 2.3.1 Photoelectric effect

Photoemission spectroscopy (PES) is an effective technique used to probe the electronic structure of materials through the photoelectric effect. The photoelectric effect was discovered by Hertz (Hertz, 1887) and explained using the point of view of the quantum nature of light by Einstein in 1905. By exposing the light with photon energy ( $h\nu$ ) on the material, the electrons are emitted out from the surface of the material with the minimum kinetic energy ( $E_{kin}$ ) when the photon energy is greater than the work function ( $\phi$ ). The kinetic energy ( $E_{kin}$ ) of photo-electron depends on its binding energy ( $E_B$ ) and  $\phi$ , where their relationship can be written as

$$E_B = h\nu - \phi_A - E_{kin} \quad 2.75$$

Normally, the work function of the analyzer ( $\phi_A$ ) exceeds the work function of sample. Therefore,  $\phi_A$  is usually respected as the reference work function relating to the Fermi level in all experiments (using the same analyzer).

### 2.3.2 The photoemission process

The photoemission process can simply be described as following; after shining the light on the sample surface, electrons are ejected out to the vacuum described by the photoelectric effect. In this part, the appropriate and necessary description including three-step model and the more realistic of one-step model will be discussed.

#### 2.3.2.1 Three-step model

The three-step model is commonly used to describe the simple view of the photoemission process. The three important steps and description of this model is displayed in figure 2.1 (left). The three steps of photoexcitation, transport, and

escape of photoelectron are shown below.

#### I) Photoexcitation of electron inside the sample

This step occurs when an occupied electronic state (initial state) is excited by the photon to an unoccupied state. Then, the photon is adsorbed, and an electron-hole pair is created inside the crystal with the transition probability ( $\omega$ ) given by the Fermi golden rule. This rule will be explained in the next section. As photons have very little momentum, the electron momentum is also unchanged in this state.

#### II) Transport of photoelectron to the surface

This process can be described in terms of a selective-mass-mean-free-path of any materials. This term relates to the probability of the excited electron travel through the surface without scattering. In this process, some inelastic scattering electrons give some needless background continuous spectra which is usually subtracted.

#### III) Escape of the photoelectron into the vacuum:

The excited electron in the surface requires the energy which is higher than work function of the materials to escape from the surface. In this process, the momentum perpendicular to the surface is not conserved depending on excited energy and the sample surface. Consequently, this step provides the information of the transmission probability out of the surface depending on the excited energy and work function.

#### 2.3.2.2 One-step model

One-step model considers the whole photoemission process as one single step. The whole process can be described as; the excited electron from an initial Bloch state go to a damped final state near the surface. This damping state of electron takes care the whole process traveling through the surface of solid with a short

mean free path. In contrast to the three-step model, the one-step model replaces three artificial steps of three-step model as a single coherent process shown in figure 2.1 (right).

Correction of the photoemission process is based on Fermi's Golden rule with proper function for initial and final state. This problem cannot be solved rigorously. However, the key to attempt the solution is the simplification within the sudden approximation which is extensively used in many body calculation of the photoemission spectra. This approximation works by assuming no post-collisional interaction between photoelectron and system left behind and no relaxation from the excitation. This approximation serves well for relatively high kinetic energy photoelectrons.

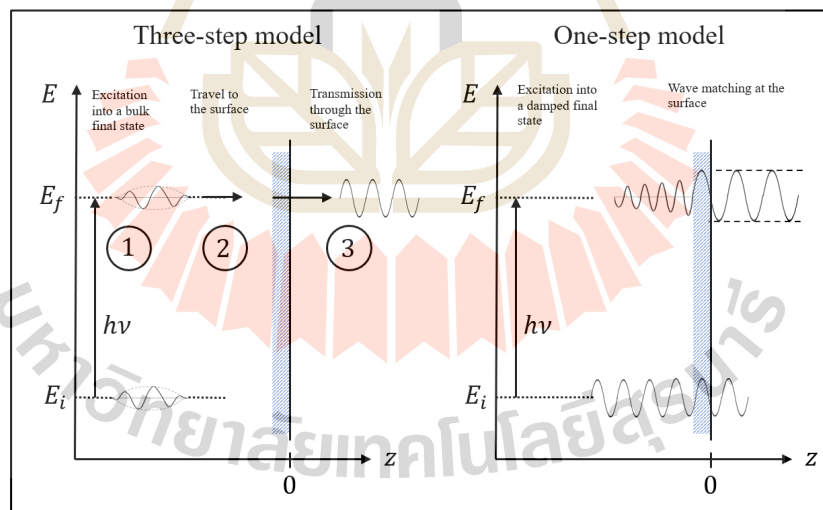


**Figure 2.5** Illustration of three-step model and one-step model that use for describing the possible photoemission process (Hufner, 1995).

### 2.3.2.3 Photoemission theory

More intensive interpretation of photoemission will be discussed in this section. Firstly, consider the Fermi's golden rule which is the probability approximation about the transition from the N-electron ground state into one of the possible final states by photoexcitation using the perturbation theory. The Fermi's golden rule has the general formula as

$$\omega_{f,i} = \frac{2\pi}{\hbar} |\langle \psi_f^N | H_{int} | \psi_i^N \rangle|^2 (E_f^N - E_i^N - h\nu) \quad 2.76$$

where  $\psi_i^N$  and  $\psi_f^N$  are the initial state and final state energies of the N-particle system. The photon field gives rise to photoemission process via a perturbing term in the Hamiltonian given by

$$H_{int} = -\frac{e}{2mc} (2A \cdot p - i\hbar \nabla \cdot A) \quad 2.77$$

where  $p$  and  $A$  are the electronic momentum operator and the electromagnetic vector potential, respectively. In the bulk or continuous region, where  $A$  is constant over atomic dimension and therefore  $\nabla \cdot A = 0$ . Then, the direct transition term ( $A \cdot p$ ) exhibits dominant contribution to the photoemission intensity preserving the crystal momentum of the electron during the photoexcitation while the second term ( $\nabla \cdot A$ ) is ignored. However, at the surface, we should concern about  $\nabla \cdot A$  term which is important where the electromagnetic field may have a strong spatial dependence and can be compared to the direct transition term. Next, the initial state wave function is assumed to be the product of one-electron orbital ( $\phi_i^k$ ) and an (N-1)-particle term from the single determinant. This relation can be expressed as

$$\psi_i^N = A \phi_i^k \psi_i^{(N-1)} \quad 2.78$$

where  $A$  is the properly  $N$ -electron wave function antisymmetric operator,  $\phi_i^k$  is the wave function of the initial state with momentum  $k$  before photoexcitation, and  $\psi_i^{(N-1)}$  is the wave function of the remaining  $(N-1)$  electrons.

By the sudden approximation, the final state can also be written as

$$\psi_f^N = A\phi_f^k\psi_f^{(N-1)} \quad 2.79$$

here,  $\phi_f^k$  is the wave function after photoexcitation, and  $\psi_f^{(N-1)}$  is the final state wave function of the  $(N-1)$  electrons left behind. Two equations above are substituted into Eq. 2.5 and the solution can be then written as

$$\langle \psi_f^N | H_{int} | \psi_i^N \rangle = M_{f,i}^k \langle \psi_s^{N-1} | \psi_i^{N-1} \rangle \quad 2.80$$

By looking into this immediate formula. The  $\langle \phi_f^k | H_{int} | \phi_i^k \rangle \equiv M_{f,i}^k$  term is the one-electron matrix element (resulted from eq. 2.79 and 2.80). The second term is the  $(N-1)$ -electron overlap integral, and the  $\psi_f^{(N-1)}$  is replaced by the eigenstate  $(\psi_s^{(N-1)})$ . To define the real system, considering the ejected electron from  $\phi_i^k$  to  $\phi_s^k$  scatters with the remaining  $(N-1)$  electrons system. The system organizes to reach its minimum energy allowing many possible transitions from wave functions  $(\psi_s^{(N-1)})$  and energies  $(E_s^{N-1})$  to the final state of  $(N-1)$ -electrons system. Then, the total photoemission intensity measured as a function of  $E_{kin}$  at any  $k$ , namely  $I(k, E_{kin}) = \sum_{f,i} W_{f,i}$  is equal to

$$I(k, E_{kin}) = \sum_{f,i} |M_{f,i}^2| \sum_s |c_s^2| \delta(E_{kin} + E_s(N-1) - E_N^i - h\nu) \quad 2.81$$

where  $|c_s^2| = |\langle \psi_s^{N-1} | \psi_i^{N-1} \rangle|^2$  is the probability that electron from initial state  $i$  can be removed from  $(N-1)$  electrons systems into excited state  $s$ . In noninteracting system with  $\psi_i^{N-1} = \psi_{s_0}^{N-1}$  and for one particular  $s = s_0$ , where  $|c_{s_0,i}|^2$  and all others are vanished, the ARPES spectra is formed as a delta function at the Hartree-Fock orbital energy. In contrast, for strongly-correlated systems, many of the  $|c_{s,i}|^2$  are non-zero because any  $\psi_i^{N-1}$  overlaps with many of the eigenstates  $\psi_s^{N-1}$ . Hence, the ARPES spectra is not only the single but also many delta functions according to the number of excited state created in the process. By invoking sudden approximation, we can now obtain the ARPES intensity for a 2D single-band system which can be written as

$$I(k, \omega) = I_0(k, \nu, A) f(\omega) A(k, \omega) \quad 2.82$$

where  $k = k_{\parallel}$  is the in-plane electron momentum,  $\omega$  is the electron energy respect to the Fermi level,  $\nu$  is the electron energy, and  $A$  is the polarization of incoming photon. Term of  $I_0(k, \nu, A)$  is proportional to the squared one-electron matrix element  $|M_{f,i}^k|^2$ . The Fermi Dirac function ( $f(\omega) = (e^{\omega/k_B T} + 1)^{-1}$ ) can probe only occupied states. The  $A(k, \omega)$  term will be introduced later as spectral function. In some cases, for example, in many 2D systems, the  $I_0(k, \nu, A)$  is slowly varying respect to the energy and momentum. Hence, photoemission can directly probe the spectral function which is directly related to the Green's function introduced by

$$A(k, \omega) = \frac{\text{Im}G(k, \omega)}{\pi} \quad 2.83$$

In strongly-correlated-electron system, the correction of the Green's function ( $G(k, \omega)$ ) may be described in terms of electron self-energy  $\Sigma(k, \omega) = \Sigma(k, \omega) + i \Sigma(k, \omega)$ . The real and imaginary parts of the self-energy carry

the information of the energy renormalization and lifetime of an electron with noninteracting band ( $\epsilon_k$ ) and  $k$ . Thus, the Green's function can be expressed in term of self-energy as

$$G(k, \omega) = \frac{1}{\omega - \epsilon_k - \Sigma(k, \omega)} \quad 2.84$$

substituting eq. 2.63 to eq. 2.64, the corresponding spectral function is

$$A(k, \omega) = \frac{1}{\pi} \frac{\text{Im} \Sigma(k, \omega)}{[\omega - \epsilon_k - \text{Re} \Sigma(k, \omega)]^2 + [\text{Im} \Sigma(k, \omega)]^2} \quad 2.85$$

Note that  $\epsilon_k$  is the bare band of the electron, we can see that when  $\Sigma(k, \omega) = 0$ , the spectral function is a delta function, or assuming no electron-electron correlation, the function will distribute as a Lorentzian function.

In general, many systems always have electron- electron correlation but remain at equilibrium itself. Disturbing the system by adding one extra electron into Bloch state causes the excitation into the whole system. This process will then result in the creation of additional electron-hole pairs. Hence, all of energy and electron lifetimes are changed because of the Fermi sea (discontinuous of momentum distribution). To simplify this matter, we introduce namely quasiparticle to describe that the correlated electrons are dressed by virtual excitations and move coherently with the electron through the crystal. Thus, the spectral function in the correlated electron system will be determined by Lorentzian function based on energy and lifetime of introduced quasiparticle.

### 2.3.3 Core level spectroscopy

Core level spectroscopy is a proper tool which is used to investigate the chemical composition and assign a chemical state in any elements on the material surfaces. Soft x-ray photoemission spectroscopy (XPS) is used as a basic technique to investigate the elemental compositions on the sample surfaces by irradiating soft x-rays to the sample. The photoelectrons are ejected out of the surfaces and will be analyzed respect to their kinetic energies. Because each element has a characteristic set of binding energies, the peak positions can be used to identify the elements with respect to the surface of detected material. The concentration of particular element can be determined by integrating area under significant peaks based on the Shirley background (inelastic scattering event) which already has the standard ratio used to compare in any individual element. There will be some small shifts of the binding energies of a particular peak containing information of the chemical state of atoms. Apart of the photoemission process, this process may excite the Auger electrons caused by empty state filled by electron from higher shell, particularly in the core level. However, the Auger electrons manifest the same kinetic energy so they can be clarified by changing the photon energy during experiment.

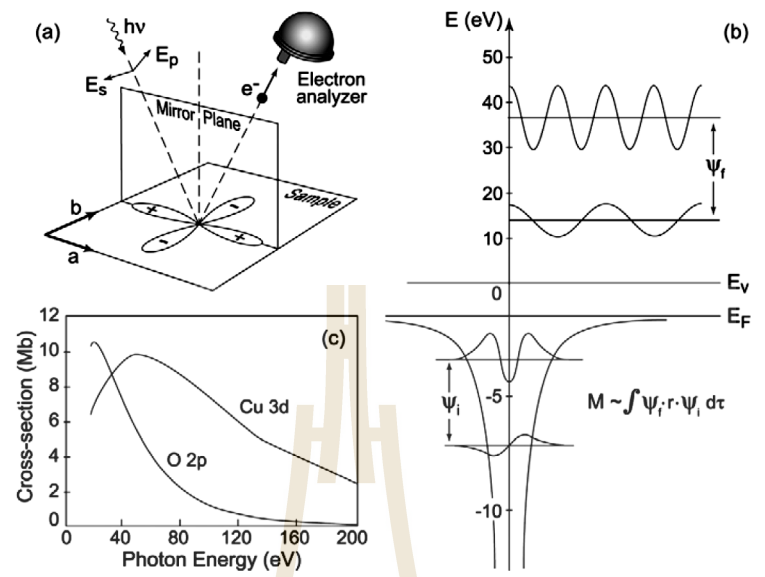


**Figure 2.6** a) Mirror plane emission from a  $d_x^2 - d_y^2$  orbital indicates the opposite sign of initial wave function from each direction. b) Sketch of the optical transition between atomic orbital with different angular momentum results to the intensity variation of outgoing electron. c) Calculated photoionization-cross-section of Cu 3d and O 2p as a function of photon energy (Damascelli, 2004).

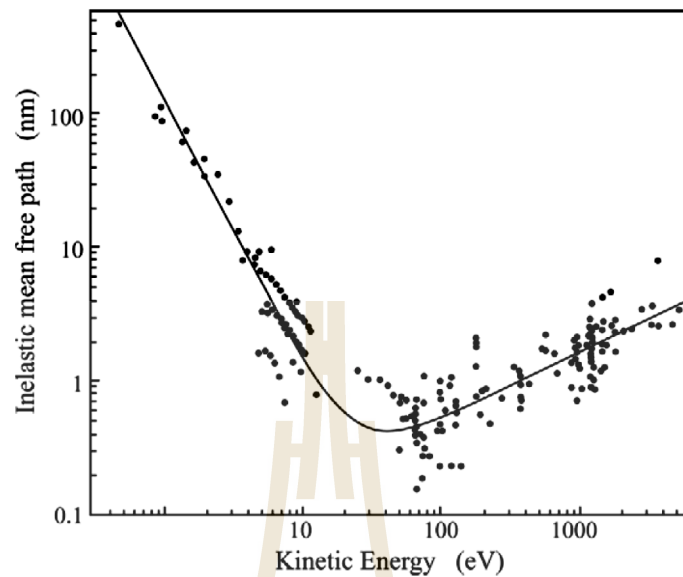


**Figure 2.7** The standard 'Universal' electron-mean-free-path in solids as a function of kinetic energy (Damascelli, 2004).

### 2.3.4 Charging effect

In photoemission process, after the light irradiates the sample, the escaping photoelectrons will experience the energy redistribution from the Coulomb interaction. This effect is named the charging effect, which causes the energy shifting and broadening of 10 meV for conducting sample in high-resolution synchrotron light source. Figure 2.8(a) shows the Fermi edge broadening and shifting of gold as a function of sample current (Zhou et al., 2005). This indicates a large uncertainty caused by charging effect even measuring in good conducting environment. This might be the main obstacle for fundamental studies especially in high-temperature-superconductors or strongly-correlated system (Damascelli, 2004) In the present, to aid such studies requires very high resolution in range of few meV. Because of the Coulomb interaction between each electron, the fast electrons are pushed by the electrons behind them while

the slow one is being retarded. This reason will distort the intrinsic information by broadening the distribution of electrons. The energy shifting is strongly dependent on the kind of accumulation on the surface. The typical accumulation is introduced as hole accumulation which drive the valence band to lower binding energy.

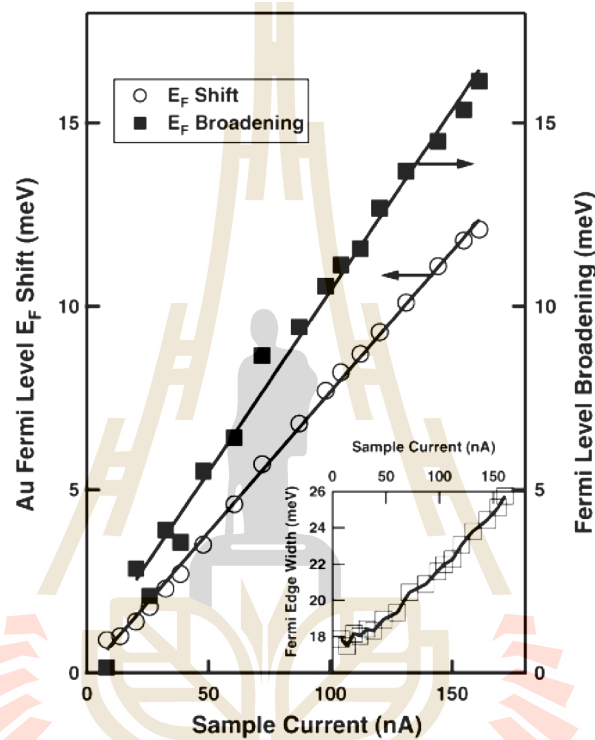


**Figure 2.8 a)** Fermi edge broadening and the Fermi edge shift of gold as a function of sample current (Zhou et al., 2005).

According to a large number of materials can be measured using ARPES. From the previous report, the minimum of 10 meV resolution is introduced by charging effect in the third-generation synchrotron. However, in fact, charging effect is one of the major problem in ARPES especially in non-conducting materials. This effect may give the energy shift up to hundreds meV caused by charge accumulation on the surface. In conducting material, this should not be a problem because the electrons move freely in the sample and fill the missing electron. However, for non-conducting

material, the electrons are accumulated on the sample surface induced the electric field (summarized in figure 2.8). This electric field will block the photoemission process and sometimes interrupt all information. Grounding is the best way to prevent the sample from charging effect. The sample has to be mounted with conducting holder (copper is typically used) by conducting glues. Commonly, the bounding process can be done by spraying the graphite covering all the sample to ensure that the sample is electrical contacted with the holder. During the measurement, some charging evidence like unsteady binding energy or blurred spectrum may happen. There are two typical techniques to suppress the charging effect. Firstly, reducing the light exposure will help to decrease the number of photoelectron (reducing the surface accumulation.) Secondly, increasing the temperature which help the sample to be more conducting by its nature. Anyway, the data quality may be worse because lower photoelectrons are ejected out compared with the presence of Fermi-Dirac distribution. Adding the alkali ions such as  $K^+$  may help to restore the charged surface with electron donation as well.

### 2.3.5 Reciprocal lattice

To understand the real space lattice structure or electronic structure requires the knowledge of reciprocal lattice. Methods such as XRD can be built and understood by exploiting the knowledge of reciprocal lattice. Because light behaving like matter-wave, this leads to the relation between spatial and momentum space through the de Broglie relation (previously explained in section 2.5.2). This condition is well known as Bragg's law (further information provided in XRD section). In crystal, atoms are periodically arranged in three-dimensional real space lattice.

The characters of the lattice have been defined as unit vectors  $a$ ,  $b$ , and  $c$  with angles  $\alpha$ ,  $\beta$ , and  $\gamma$  respectively (see figure 3.2(a)). All atoms in the perfect lattice are equivalent in one reference point. The neighboring atoms can be expressed in term of translation vector ( $T$ ) given by

$$T = n_1a + n_2b + n_3c \quad 2.86$$

where  $n_1$ ,  $n_2$ , and  $n_3$  are integers. We can define the plane and direction of the real space lattice by using this translation vector (eq. 3.5). The defined plane is generally used to indicate the sample orientation. The direction of sample plane can be written in the format of integer triplet  $[n_1 \ n_2 \ n_3]$ . For example, the chosen translation vector ( $T_1 = 1a + 1b + 1c$ ) refers to the integers  $n_1 = n_2 = n_3 = 1$ . The plane of vector is denoted by  $[111]$ . The plane orientation can be specified by the interception of the number straight up to the basis vectors. In case of the  $[001]$  plane of cubic lattice, the plane is cut through  $z$ -axis giving the  $xy$ -plane normal to  $z$ -axis.

To understand the relationship between real and reciprocal lattice, we have introduced the reciprocal lattice vector  $G(hkl)$  to describe the lattice behavior. The real space lattice vector ( $R$ ) is equivalent to  $T$ . The condition of periodic structure will always satisfy the following equation,

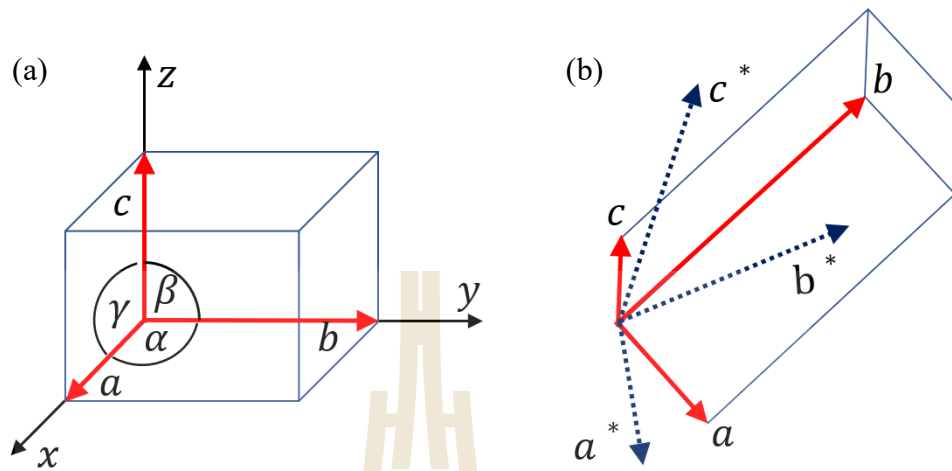


**Figure 2.9** a) A unit cell with three basis vectors  $a$ ,  $b$ , and  $c$  with the respected angles of  $\alpha$ ,  $\beta$ , and  $\gamma$ . b) Illustration of reciprocal lattice vectors,  $a^*$ ,  $b^*$ , and  $c^*$  relating to the real space vectors.

$$e^{iG \cdot R} = 1 \quad 2.87$$

where  $G \cdot R = 2\pi n$

therefore, the reciprocal lattice is commonly defined as

$$G(hkl) = ha^* + kb^* + lc^* \quad 2.88$$

where  $h$ ,  $k$ , and  $l$  are the Miller indices of a crystal plane. The  $(hkl)$  is referred to the reciprocal unit vector illustrated in figure 2.9(b). By mathematical satisfaction, the reciprocal lattice vectors must be in the form of

$$a^* = 2\pi \frac{b \times c}{a \cdot (b \times c)}, \quad b^* = 2\pi \frac{c \times a}{a \cdot (b \times c)}, \quad c^* = 2\pi \frac{a \times b}{a \cdot (b \times c)} \quad 2.89$$

In the simple hexagonal lattice, the xy- and z-plane are denoted by a and c. The reciprocal lattice is still in hexagonal form, but its axis is substituted by  $\frac{4\pi}{a\sqrt{3}}$  and  $\frac{2\pi}{a}$  a rotating  $30^\circ$  around c-axis respected to the real space lattice. The high symmetry points are generally given to simplify the direction respect to the hexagonal shape shown later in figure 5.1(a). The electronic structure of the materials is described through the points in reciprocal space.

### 2.3.6 Spin-orbit interaction

An interaction between orbital angular momentum (L) and spin (S) of the particle is called spin-orbit interaction (SOI). When electron moves around the nucleus, resulted in the interaction between spin and the magnetic field generated by the electron's orbit around the nucleus. This interaction causes many effects in electronic structure such as shifts of spectral lines in atomic energy level and momentum splitting in 2DEG materials (Rashba effect). SOI plays an important role in manipulating the electron's spin in the materials.

## 2.4 X-ray diffraction of single crystal: Laue method

The x-ray diffractometer or x-ray diffraction (XRD) is a common technique to determine the crystal structure in solid. The well-known equation for XRD is Bragg's law which describes the relation between diffraction angle and the point position in the reciprocal space which can be expressed as

$$2d\sin\theta_x = n\lambda \quad 2.90$$

where  $n$  is the integer according to the number of scattering planes which is usually denoted as 1,  $d$  is the plane spacing in the atomic lattice,  $\lambda$  is wavelength of incident x-ray wave and Bragg angle ( $\theta_x$ ) is the angle between incident and the reflection plane.

On the other hand, the oldest x-ray diffraction method is Laue method (LM) which serves as a powerful tool to study the layered materials, single crystals, and polycrystalline. This technique is very helpful in my work as it is used to check the perfection of our single crystal before the MOKE measurement. LM uses the graphical method to determine the Laue spots on the photograph. LM have been divided into transmission and back- reflection modes. The perfection of the crystal can be determined by the spots on the photograph. The spots from perfect crystal are sharp while the spots are diffused or elongated for the imperfect or polycrystalline. The practical formula of LM introduced by E. Schiebold (Schiebold, 1932) expresses how to calculate the important value for the standard setup as shown in figure 2.10.

The position of any spots away from the center of the incident light can be determined using the geometry in figure 2.10. In the simplest case, if the incident x-ray beam is perpendicular to the principal crystal plane and the photographic plane (c-axis or (001) plane). A distance of Laue spot on the film ( $r$ ) can be expressed according to the  $\theta_x$  as

$$r = D \cdot \tan 2\theta_x \quad 2.90$$

where  $D$  is the distance between the crystal and the photographic plate. The azimuthal angle ( $\psi$ ) and  $\theta_x$  are independent of the wavelength and can be expressed in terms of unit cell dimension. The  $\psi$  represents the possible spot away from the reference orientation related to the angle between a- and b-axis while the reflection

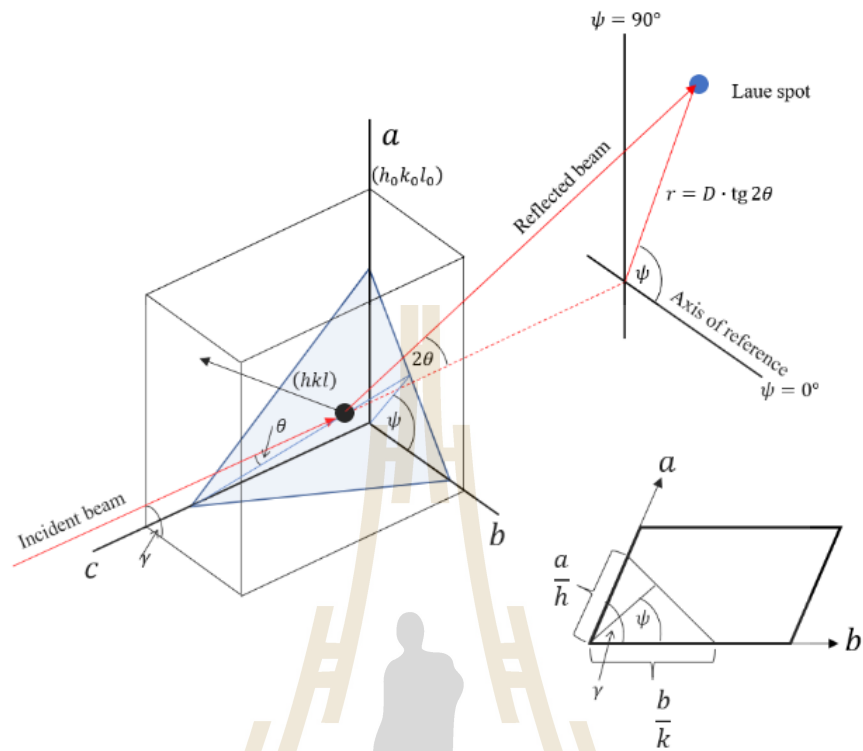


**Figure 2.10** Geometrical relationship between position of the Laue spots and the reflecting plane (Kedesy, 1954).

angle ( $\gamma$ ) represents the distance away from the center. The relation between  $\psi$  and  $\gamma$  can be given by

$$\tan \psi = \frac{1}{\sin \gamma} \left( \frac{b}{a} \cdot \frac{h}{k} - \cos \gamma \right) \quad 2.91$$

If the ratio between  $h$  and  $k$  is the same, this condition gives the discrete spots lining straight from the center of the pattern.

## 2.5 Bismuth ferrite (BiFeO<sub>3</sub>)

A single-phase multiferroic material (Fiebig, 2005) is a material that simultaneously possesses more than one ferroic order parameters, including ferroelectricity, ferromagnetism, and ferroelasticity. Relevance between the magnetic properties and electrical properties of the material, namely the magnetoelectric coupling which is the linear magnetoelectric effect or the induction of magnetization by an electric field or polarization by a magnetic field. (Eerenstein et al., 2006b). At present, the interestingness of coupling between magnetic and electronic order parameters and the manipulation one through the other stimulates the eagerness of researchers. The ultimate goal of studying multiferroic materials is to produce device functionality in a single-phase multiferroic with strong coupling between ferroelectric and ferromagnetic order parameters, making it easy to control the magnetic behavior with an electric field.

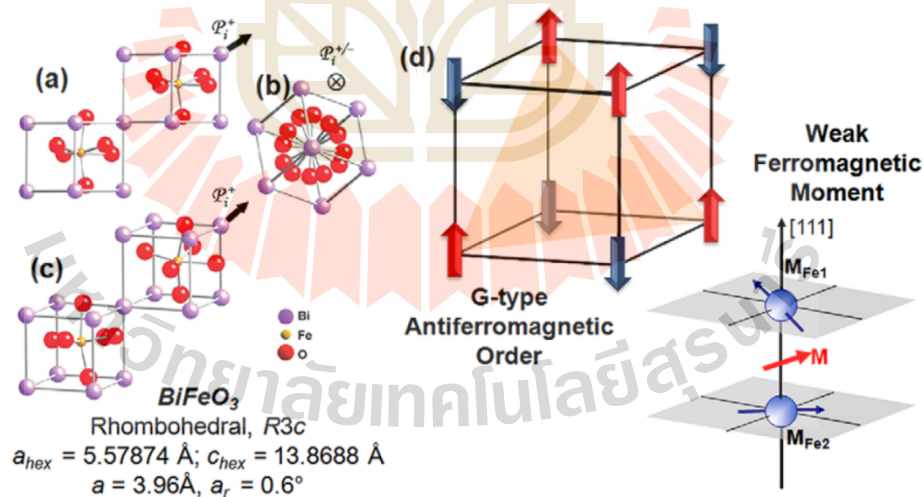


**Figure 2.11** Crystal structure of BiFeO<sub>3</sub> shown (a) the pseudocubic-[110], (b) the pseudocubic-[111]-polarization, and (c) isometric view of the structure (d) G-type antiferromagnetic ordering and the formation of the weak ferromagnetic moment (Martin et al., 2008).

### 2.5.1 Crystal structure of Bismuth Ferrite (BiFeO<sub>3</sub>)

At room temperature, BiFeO<sub>3</sub> is in rhombohedral phase belonging to the space group R3c (Moreau et al., 1971). Lattice parameter of a rhombohedral structure of BiFeO<sub>3</sub> consist of  $a_{rh} = 3.965 \text{ \AA}$  and a angle of  $\alpha = 89.3-89.4^\circ$  at room temperature. The ferroelectric polarization point along [111] pseudocubic (Catalan and Scott, 2009).

Simultaneously, we can characterize the rhombohedral structure in a hexagonal viewpoint by connecting two perovskite cubes along with their body diagonal, i.e.,  $[001]_{hexagonal} \parallel [111]_{pseudocubic}$ . The hexagonal lattice parameters consist of  $a_{hex} = 5.58 \text{ \AA}$  and  $c_{hex} = 13.90 \text{ \AA}$ . In figure 2.11(c), two pseudo cubic unit cells are connected together in order to illustrate that successive oxygen octahedra along the polar [111] axis rotate with opposite sense around [111] direction. The magnetic moments of Fe atoms is oriented in the (111) plane indicated by the red arrow (Lubk et al., 2009).

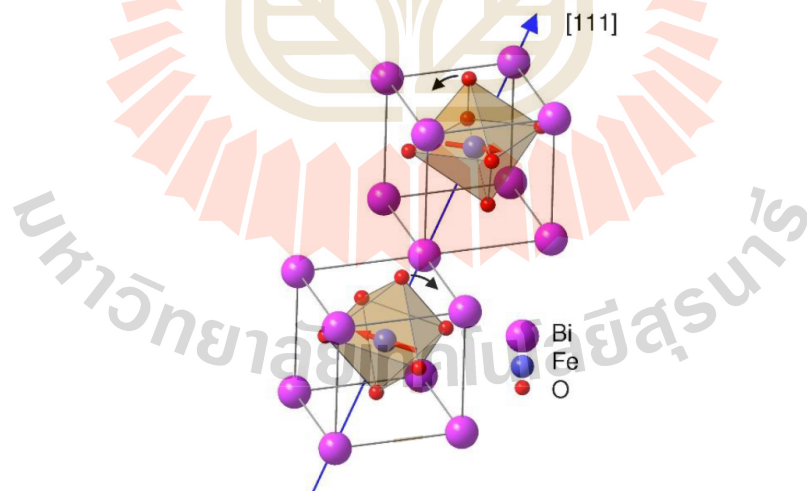


**Figure 2.12** Crystal structure of bulk BiFeO<sub>3</sub> (Lubk et al., 2009).

### 2.5.2 Magnetism of Bismuth ferrite (BiFeO<sub>3</sub>)

The BiFeO<sub>3</sub> possesses a ferroelectric polarization ordering with a high Curie temperature  $T_c$  of 1103 K and antiferromagnetic ordering with a magnetic transition temperature  $T_N$  of 643 K (Fiebig, 2005). In [111] pseudo-cubic planes, the Fe magnetic moments are ferromagnetically coupled while they are antiferromagnetically coupled between the near planes. this is called the G-type antiferromagnetic order. In the event that the magnetic moments of Fe atom are oriented perpendicularly to the [111] direction, the symmetry of structure cause a canting of spin in the antiferromagnetic sublattices, cause a macroscopic magnetization called weak magnetism (Yan et al., 2015). The spontaneous polarization of BiFeO<sub>3</sub> depend on the crystal structure, that is the tetragonal structure (Space group: P4mm) evince the polarization about  $150\mu C/cm^2$  in the [001] direction, and the rhombohedral structure (Space group: R3c) evince the polarization about  $100\mu C/cm^2$  in the [111] direction without strain (Waterfield Price et al., 2019). The octahedral turn  $11-14^\circ$  around the polar [111] axis (Catalan and Scott, 2009). And in addition, Fe-O-Fe angle is  $154-156^\circ$  and it has been found that the Fe-O-Fe angle of BiFeO<sub>3</sub> can controls both the magnetic ordering temperature and the conductivity via the magnetic exchange and orbital overlap between Fe and O.

### 2.5.3 Symmetry of magnetism and spin cycloid in BiFeO<sub>3</sub>

Magnetism of bismuth ferrite (BiFeO<sub>3</sub>) is a result of both short- and long-range magnetic orderings. G-type antiferromagnetism causes the local short-range magnetic ordering in BiFeO<sub>3</sub> sub-domain. Because of a spin of Fe<sup>3+</sup> which is surrounded by six antiparallel spins on the neighbor of Fe<sup>3+</sup> ion and the structural distortion, the arrangement of the neighboring spins is not perfectly antiparallel. However, the canted spins in the antiferromagnetic domain give a weak magnetic moment which can couple with the ferroelectric polarization. Overlap of spin canting takes place in a long-range superstructure which consists of an incommensurate spin cycloid of the antiferromagnetically ordered sublattices (Catalan and Scott, 2009). This cycloid of spin canting has a very long period of 64 nm (Lebeugle et al., 2008). Figure 2.13 shows the magnetic easy plane that is the plane of the spins rotation, which is defined by the cycloid propagation vector (black) and the polarization vector (red). The total of canted antiferromagnetic spins (blue and green arrows) is a net magnetic moment (purple arrows) that is normally averaged out to zero due to the cycloidal rotation.

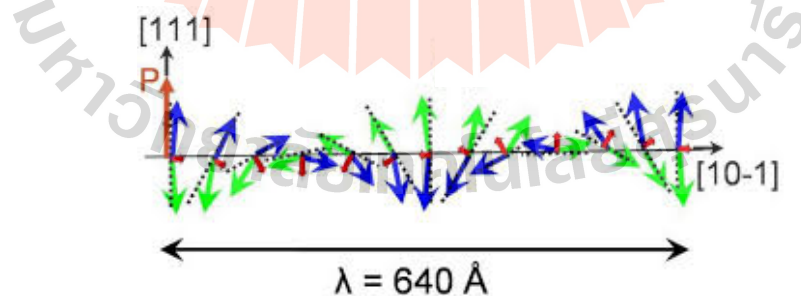


**Figure 2.13** Antiferromagnetic structure of BiFeO<sub>3</sub>, the vector diagram of magnetic moments points in the direction along a cycloid with a period of 64 nm.

## **CHAPTER III**

### **RESEARCH METHODOLOGY**

In chapter III, we intend to describe the experimental method which were categorized into the following two main section.

(I) Experimental method in the study of Bismuth Ferrite ( $\text{BiFeO}_3$ ).

- Magneto-optical Kerr effect Magnetometer (MOKE) set up and calibration with Fe thin which prepared by Molecular beam epitaxy (MBE).
- Details of sample preparation techniques: synthesis of  $\text{BiFeO}_3/\text{SrRuO}_3/\text{SrTiO}_3$  heterostructure by RF magnetron sputtering.
- Kerr rotation measurement: Magneto-optical Kerr effect Magnetometer
- Material characterizations techniques: X-ray diffraction (XRD), Atomic force microscope (AFM) and piezo force microscope (PFM), and X-ray photoemission spectroscopy (XPS).

(II) Experimental method in the study of  $\text{Ni}/\text{Bi}_2\text{Te}_3$ .

- Sample preparation techniques: Electroless deposition technique
- Magnetic measurement: Magneto-optical Kerr effect Magnetometer
- Material characterizations: electrochemical measurement by cyclic voltammetry (CV), X-ray photoemission spectroscopy (XPS), X-ray absorption spectroscopy (XAS).

### 3.1 Magneto-optical Kerr effect (MOKE) magnetometer set up

In the study of bismuth ferrite, due to the sample has a very high smoothness, MOKE is basically only a few components are necessary when trying to construct a MOKE setup. A light source (L), two polarizers (P<sub>1</sub>, P<sub>2</sub>), Faraday cell (F), a sample (S), Len(L), a detector (D), and means of creating a magnetic field across the surface of the sample. This is illustrated in Figure 3.1

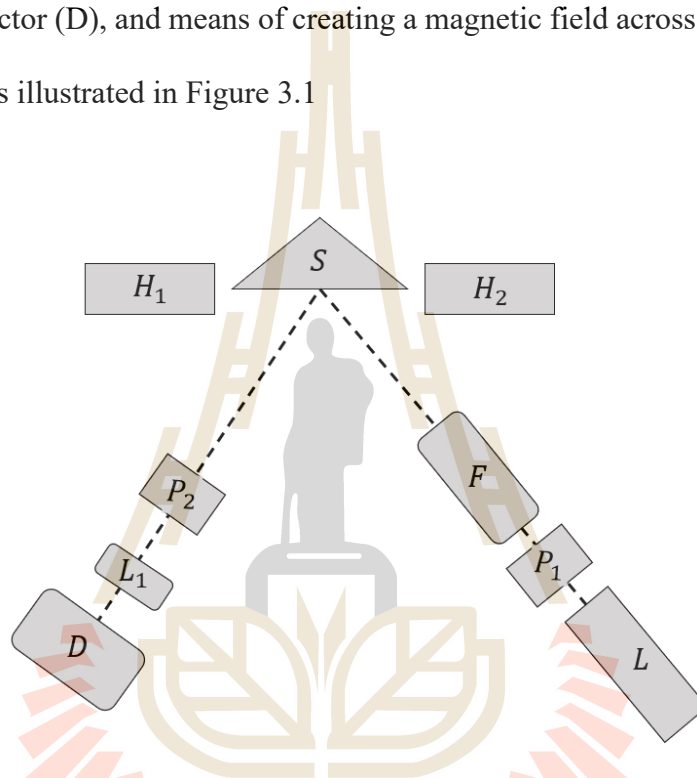


**Figure 3.1** Schematic of the basic components needed for a MOKE setup. Light source (L), polarizers (P), a sample (S), a detector (D), and electromagnets (E). OP naturally denotes the optical path.

In the same way, because of the surface of the Ni/Bi<sub>2</sub>Te<sub>3</sub> sample has a lower macroscopic smoothness the reflected light has been flared to be a cone-shaped beam. A more complicated MOKE setup was performed, following figure 3.2.

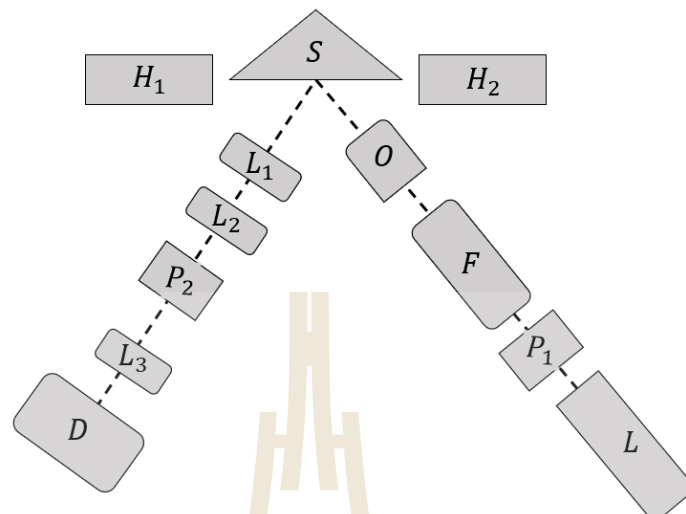


**Figure 3.2** Schematic of the basic components needed for a MOKE setup. Light source (L), polarizers (P), a sample (S), a detector (D), and electromagnets (E). OP naturally denotes the optical path.

The figure illustrates the relatively simple geometry used for obtaining hysteresis loops or Kerr rotation of surface structures in free air. In the figure 3.2 (LD) signifies the optical path beginning at the laser (L) and ending at the detector (D). In between are two polarizers (P<sub>1</sub> and P<sub>2</sub>), Faraday cell (F), Objective lens(O), Lens (L<sub>1</sub>, L<sub>2</sub>, L<sub>3</sub>) and a sample holder (S). The current optical setup employed in this measurement use Glan-Thompson prisms with an extinction ratio of 100,000:1 to produce precisely polarized light. The light source is a 640 nm Thorlab stabilized HeNe laser with intensity stabilization of 0.2%. To magnetize the surface two pole electromagnets (E<sub>1</sub> and E<sub>2</sub>) are used. The electromagnets are placed with the smallest possible distance between the cores to obtain the largest, most homogeneous field in a gap of 50mm the electromagnets produce a magnetic field of 1800G with a maximal current of 20A. Electromagnet was able to apply a large current to create a magnetic field, which can change the direction of magnetic field by switching the direction of the applied current

in bipolar power supply. A computer controls the bipolar power supply via a general-purpose interface bus (GPIB) which can continuously control the applied magnetic field. Gaussmeter is attached to the computer via USB cable, the applied magnetic field can be accurately measured. Although we can do the in-situ measurements of the applied magnetic field, the accuracy of measurement is diminished due to the off-position of the detector. Therefore, a calibration was performed. We place the gaussmeter probe in the same position as the sample and record the magnetic field versus the applied voltage. this method can create an accurate representation of the magnetic field at the same location as sample surface.

We placed our sample at the center of the applied magnetic field on a xy translation stages with rotating platform that allows to rotate 180 degrees with respect to the plane of incidence. We observed the Kerr angle by measuring the light polarization rotation induced by the sample and compare them to each other based on the change in intensity seen after the analyzer. In our experiment, we use a Thorlab photodiode detector (DET36A) to detect the brightness of laser which pass through the analyser. The voltage from the detector is read using a lock-in amplifier, which is then recorded by the computer using a GPIB interface and a LabView control program. The power supply used for delivering the current is a BOP100-2M power supply from Kepco, a detailed description is presented in Appendix A. It is possible to operate the power supply by manually adjusting the current or using an analogue signal. The electronics surrounding the optical equipment is illustrated in figure 3.3

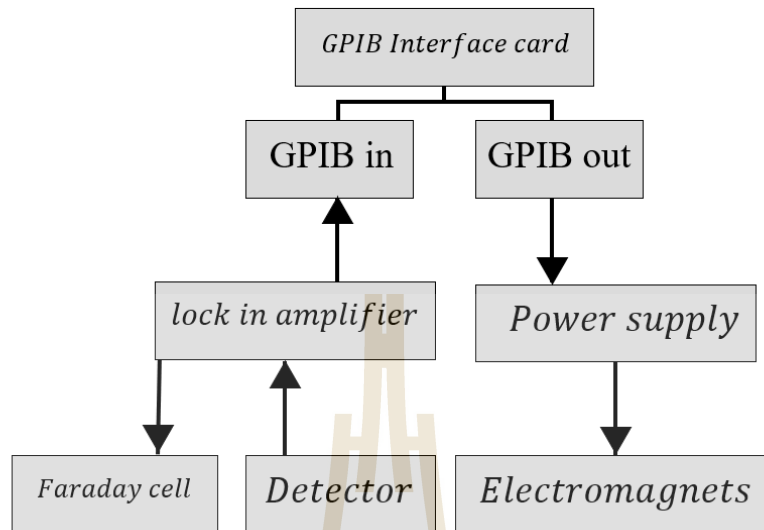


**Figure 3.3** The electronics component of MOKE.

To extract a signal from a highly noisy environment, we used a lock-in amplifier to apply a known carrier waveform to a faraday cell to modulate the laser's polarization. Using this method, the signals up to 1 million times smaller than noise, reasonably close by in frequency, can be reliably detected. However, depending on the dynamic reserve of the instrument. Moreover, signal recovery at low signal-to-noise ratios requires a clean reference signal that is the same frequency as the received signal.

A lock-in amplifier relies on the principle of the sinusoidal functions orthogonality. For example, consider the two in-phase sinusoidal function, when multiplying two sinusoidal function with frequency  $f_1$  and  $f_2$  which not equal to  $f_1$  and then integrated over a time that is longer than the period of the two functions, the result will be zero. On the other hand, if  $f_1$  is equal to  $f_2$ , the integrated value is equal to half of the product of the amplitudes. A lock-in amplifier gets the input signal from the detector and multiplies it by the reference signal, and integrates this signal over the time

that generally on the order of milliseconds to a few seconds. The result signal is a DC signal, where consist of any signal that is not at the same frequency as the reference signal is devalued to zero. The out-of-phase component of the signal that has the same frequency as the reference signal is also devalued, namely a lock-in detection is a phase-sensitive detector. Consider a sine wave reference signal and an input waveform  $W_{in}(t)$ , the integral in eq 3.1 show the DC out put signal  $W_{out}(t)$  that can be calculated for an analog lock-in amplifier as

$$W_{out}(t) = \frac{1}{T} \int_{t-T}^t \sin [2\pi f_{ref} \cdot t + \varphi] W_{in}(t) dt \quad 3.1$$

where  $\varphi$  is a phase of the reference signal is set on the lock-in amplifier (default value is zero).

The averaging time  $T$  or integral time should be wide enough (generally much larger than the period) to reduce all unwanted signal i.e. noise and the variations at twice the reference frequency, the output is

$$W_{out} = V_{sig} \cos\theta \quad 3.2$$

where  $V_{sig}$  is the signal amplitude at the reference frequency and  $\theta$  is the phase difference between the signal and reference.

Our measurement of the lock-in detection only requires recovering the signal amplitude rather than relative phase to the reference signal. For a single-phase lock-in-amplifier procedure, have to adjusted the phase difference to be zero to get the clear signal. But in another advanced system, namely two-phase lock-in-amplifiers have a second detector, calculate as before with a different 90-degree phase shift. Thus, the result consist of two outputs values including  $X = V_{sig} \cos\theta$  is named the in-phase com-

ponent and  $Y = V_{sig} \sin \theta$  is named the 'quadrature' component. These both quantities represent the signal in a vector form relative to the lock-in reference signal. By calculating the magnitude ( $R$ ) of this vector, the phase dependence value is removed and give the pure signal value as

$$R = \sqrt{X^2 + Y^2} = V_{sig} \quad 3.3$$

The phase can be calculated from

$$\tan \theta = Y/X \quad 3.4$$

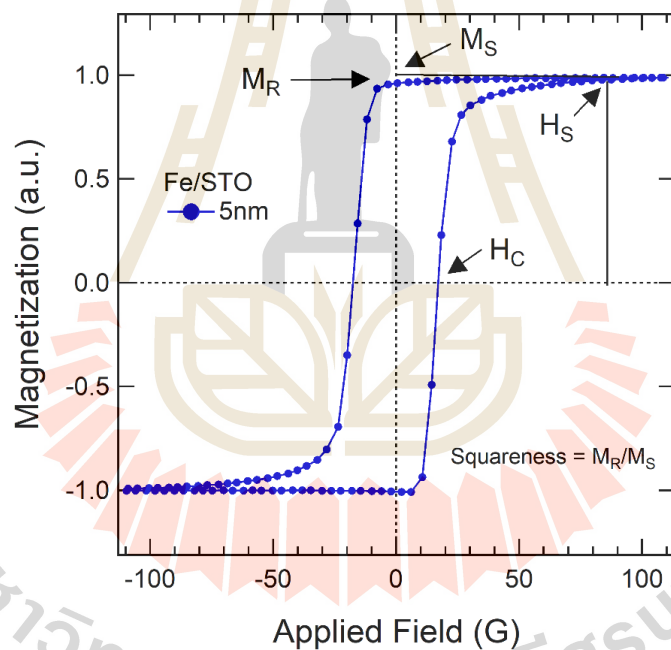


**Figure 3.4** The hysteresis loop of Fe film with 5 nm thickness shows the coercive field, the saturation field, the remnant magnetization and the saturation magnetization.

In our measurement, we used LabView program to record the data from the detector and creates a plot of Kerr rotation versus applied field. According to the theory of the total Kerr rotation in ferromagnetic material, Kerr angle linearly depend on the magnetization on the material surface. Therefore, the plot of Kerr rotation versus applied magnetic field can indicate the M-H hysteresis loop. However, we cannot determine the absolute magnetization of sample, but the saturation field, coercive field, and squareness of sample can be obtained, as shown in figure 3.4. Since the sample can rotated, the same measurements can be taken at several angles of the sample with respect to the plane of incidence. The easy and hard axis can be obtained from these rotations. For a magnetically anisotropic sample, the easy axis is defined as the axis which is energetically favorable to magnetize. If the data is taken for small increments, one can create a polar plot of the coercive field or saturation field as a function of the angle, giving insight into the magnetic anisotropy of the sample. Our MOKE system using a method known as AC-MOKE, which can determine the values of the Kerr rotation and ellipticity for a given sample. By using a faraday cell as an oscillating retarder, one can create an AC signal that can be read by a lock-in amplifier. By analyzing the AC intensity using Jones matrix analysis, it can be shown that the Kerr rotation and ellipticity can be measured separately.

## 3.2 Sample preparation techniques

### 3.2.1 Thin film growth process

In this thesis, we prepared thin films by the deposition of atoms on a substrate using chemical deposition and plasma deposition technique. Typically, the growth process of thin film is often following this process,

- (I) Firstly, a random nucleation process occurs, followed by nucleation and growth process.
- (II) The nucleation and growth process depend on deposition conditions, for example growth rate, temperature of substrate, flux rate and substrate surface chemistry.
- (III) The nucleation process can be modified by external stimuli, such as electron or ion bombardments.
- (IV) Formation of film microstructure and associated defect structure. At this stage there will be the film stress depending on the deposition condition.
- (V) Formation of crystal phase and orientation.

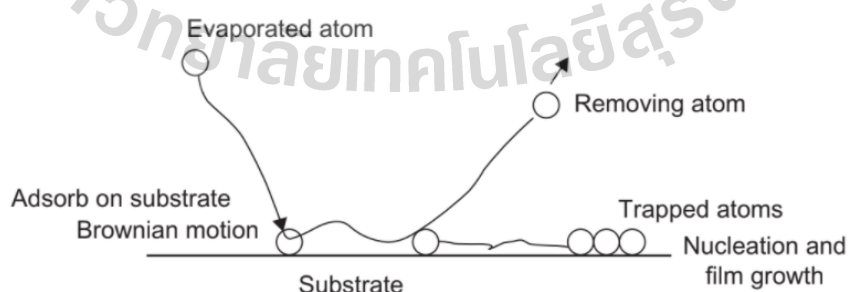


**Figure 3.5** The thin film general growth model.

### 3.2.2 Molecular Beam Epitaxial (MBE) technique

Molecular Beam Epitaxy (MBE) is a technology of growing thin film that can precisely control composition by using a process involved in thermodynamic equilibrium. The MBE growth process has extremely low deposition rates (approximately a few Å per second) caused by the accumulation of the vapor of highly pure solid elements heated in separate effusion cells or called Knudsen cell. The ultra-pure material in solid state is sublimated into gas state by heating. The gas particles move into the vacuumed space and reach the substrate, then the condensation process takes place at the surface of substrate. After that, the epitaxial arrangement takes place and the crystalline structure form depending on the flux rate. The epitaxial growth is performed in Ultra-High-Vacuum (UHV) conditions (lower than  $10^{-10}$  Torr) to reduce the impurity levels in the growing layers. A standard MBE system is shown schematically in figure 3.6

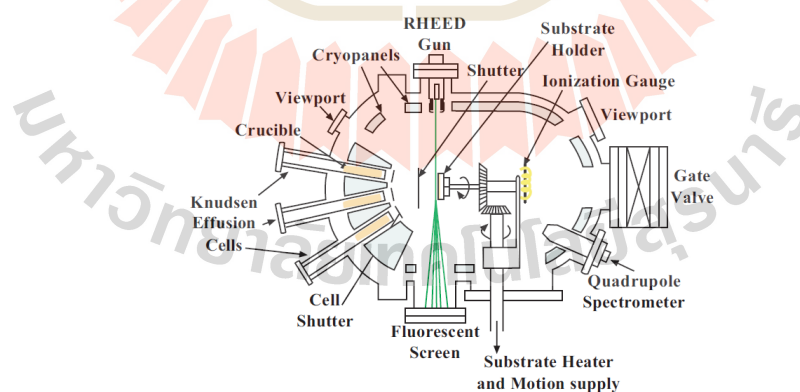


**Figure 3.6** A molecular beam epitaxy growth chamber.

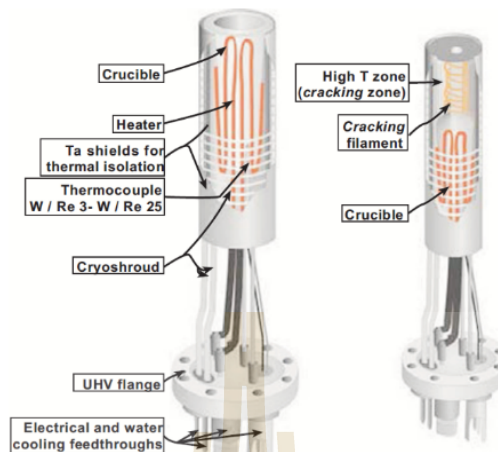


**Figure 3.7** Schematic figure of effusion cells currently used in MBE systems: (a) Knudsen cell; (b) Two stage Cracking effusion cell (Courtesy of Prof. Klaus H. Ploog).

Figure 3.7 shows the two types of effusion cells that used in general MBE system. Usually, the crucible in the effusion cell is made of pirolytic boron nitride (PBN), which can tolerate high temperatures up to 1500 °C without contamination to the prepared film. This type is named high range effusion cell. Our MBE system consist of high range effusion cell and medium range effusion cells can operate at a medium temperature lower than 1100 °C. Heater in effusion cell made from Ta filament and Ta foils is used to shield the heater to improve both the temperature stability and the thermal efficiency. The W-Re (5% and 26% Re) thermocouple is attached to measure the temperature inside the effusion cell.

### 3.2.2.1 Deposition process of MBE

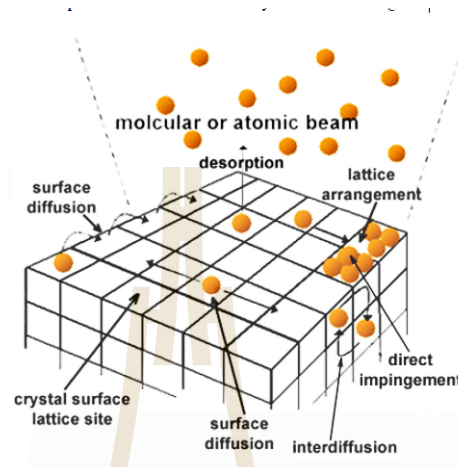


**Figure 3.8** Schematic illustration of the surface processes occurring during MBE growth.

In the epitaxial growth, there are the processes including: a) the evaporated atoms collide the surface are adsorbed on the substrate; b) the adsorbed atoms diffuse and dissolve on the surface of substrate; c) the atoms on the surface arrange themselves into the crystal lattice; d) desorption of the atoms not arranged into the lattice. In the process which the adsorbed atoms combine to form a critical size and then become stable nuclei (or clusters). the substrate temperature, the flux rates and the affinity are the important factor.

In the following section the fabrication of the Fe sample with different thickness was growth using MBE technique. The Fe sample was used to calibrate MOKE magnetometer in free air. The sample is desired to consist of a nonmagnetic silicon (100) substrate with a iron material deposited on top. This is naturally to isolate the magneto-optic response from the deposited material as much as

possible. this substrate is used merely because it is available in abundance. As a ferromagnetic material Fe is evaporated on top of the Si substrate following a standard physical vapor deposition (PVD). The thickness was calibrated by using quartz crystal microbalance (QCM).

### 3.2.3 RF Magnetron sputtering

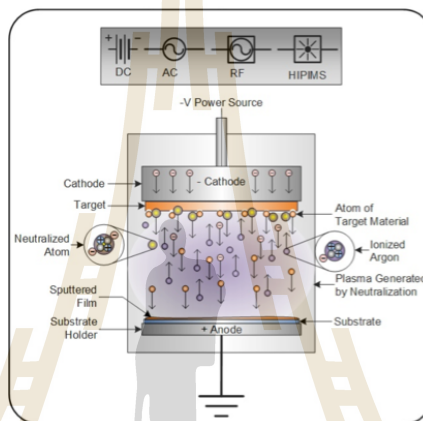


**Figure 3.9** Schematic of sputtering process (adapted from <http://www.semicore.com/news/92-what-is-rf-sputtering>)

Magnetron sputtering show the good disadvantages compare to thermal evaporation or electron-beam evaporation in case of the alloys and insulator thin film coating, because of differences in alloy constituent vapor pressures and their high melting points. The advantages of magnetron sputtering are (1) ability to give high deposition rates, (2) ability to sputter any metal, alloy, or compound, (3) the resulting film has a high purity, (4) the resulting film has a very high adhesion strength, (5) able to coat heat-sensitive substrates, (6) provide film with good uniformity on large scale area.

DC magnetrons sputtering are not suitable for an insulating target, because of the rapid formation of a positive surface charge on the front side of the insu-

lator target resulting in gradually decreasing current through it, and then the sputtering glow discharge cannot be sustained. The system named a radio frequency (RF) sputtering system, use an alternating current at radio frequency to generate plasma, can sustain the glow discharge with an insulator target. In this system, the DC voltage power supply is replaced by an RF power supply. Moreover, RF sputtering system requires an impedance-matching network between the power supply and discharge chamber. The impedance of the RF power supply is almost always  $50\Omega$ . The impedance of the glow discharge is of the order  $1 - 10\text{ k}\Omega$ . In RF diode sputtering, the cathode current density is  $i_s$  given by

$$i_s = C \, dV / dt \quad 3.5$$

where  $C$  is capacitance of discharge plasma and the target, and  $dV/dt$  is the time variations of the target surface potential.

In the RF magnetron sputtering system, the pressure should be lower than  $1\text{ mTorr}$ , because the RF electrical field increases the collision probability between secondary electrons and gas molecules. The target area is smaller than the grounded anode and the chamber wall namely asymmetric electrode configuration which induces negative DC bias on the target, and causes sputtering in the RF system. The quadrupole magnetic field increases ion current density at cathode cause an increase in deposition rate.

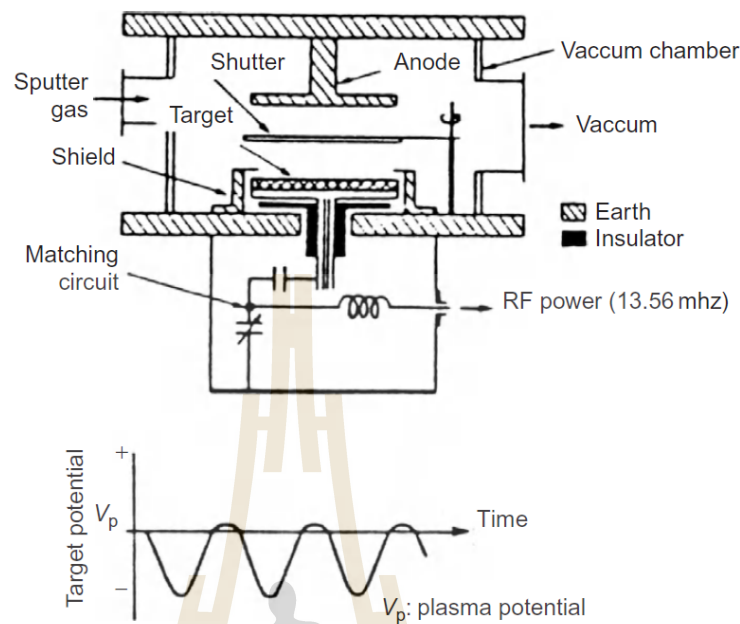


**Figure 3.10** RF diode sputtering system.

In our study,  $\text{BiFeO}_3/\text{SrRuO}_3/\text{SrTiO}_3$  heterostructure were prepared starting with (001)  $\text{SrTiO}_3$  single-crystal substrates with  $4^\circ$  miscut toward  $[110]_{\text{pc}}$  direction are used for domain formation control of  $\text{BiFeO}_3$  thin films (Baek et al., 2010). A 35-nm- thick  $\text{SrRuO}_3$  (SRO) bottom electrode layer is first deposited by  $90^\circ$  off-axis sputtering (Eom et al., 1989) at  $600^\circ\text{C}$  followed by 400 nm of  $\text{BiFeO}_3$  films grown by double-gun off-axis sputtering at  $750^\circ\text{C}$  with Ar:O<sub>2</sub> ratio of 4: 1 at a total pressure of 400 mTorr (Das et al., 2006). We used  $\text{BiFeO}_3$  target which contains 5% excess  $\text{Bi}_2\text{O}_3$  to compensate the bismuth volatility (Das et al., 2006). In the sputtering process, the substrate miscut constrain the crystal growth resulting in the growth of a single ferroelastic domain variant, at the same time the  $\text{SrRuO}_3$  bottom electrode induce an electrical boundary condition favoring the ferroelectric down (r1) state (Baek et al., 2010) since the depolarization field can be screened by free charge in the electrode dur-

ing growth (Fong et al., 2006). 71° switching leads to the monodomain up r3 + state (Saenrang et al., 2017).

### 3.2.4 Electroless-deposition (ELDP) technique

Electroless or autocatalytic plating is the chemical coating that utilize a chemical reducing agent in solution to reduce metallic ions to the metal. Instead of making the metal anode move to coat the substrate at cathode, the metal is supplied by the metal ion in the solution. ELDP is performed by adding metal salt in the solution, a substrate serving as the cathode, while the electrons are provided by a reducing agent. ELDP occurs on catalytic surfaces rather than through the entire solution, but if the process is not adequately controlled, the reduction can occur on particles of dust or of catalytic metals in entire solution.

In the solution, a chemical reducing agent supplies the electrons for converting metal ions to the metal, following this



when the metal start to deposit on a surface, the deposited metal must also be catalytic for the deposition to continue. It has been demonstrated by Marton and Schlesinger (Marton and Schlesinger, 1968) that the deposition of Ni-P on a sensitized-activated surface starts at specific activation sites and continues on these points only. This specific behavior makes the islands of material are formed around these nucleation sites, until they gather to become a continuous film. In fact, the surface of a dielectric substrate is not all activated but the activation stimulates small catalytic sites dispersed on the surface, namely the nuclei formation.

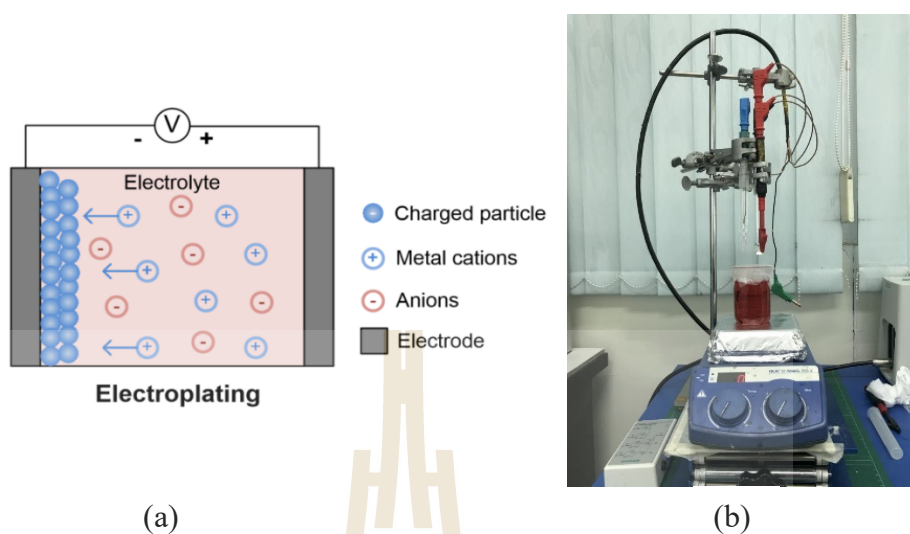


**Figure 3.11** Schematic of electroless nickel deposition (a) and photography of electroless deposition set up (b).

In our study of Ni/Bi<sub>2</sub>Te<sub>3</sub>, we performed the electroless-deposition of Nickel metal on Bismuth telluride (Ni/Bi<sub>2</sub>Te<sub>3</sub>) heterostructure. Materials that used in our process consist of analytic grade Nickel chloride ( $NiCl_2 \cdot 6H_2O$ ), Sodium chloride ( $NaCl$ ), Hydrochloric acid ( $HCl$ ) were purchased from Sigma Aldrich and were used without any further purification. Ultra-pure deionized water was used as the electrolyte solution for electrodeposition. Nickel thin films were electrodeposited from an aqueous of 40mM Nickel chloride containing 5mM NaCl as supporting electrolyte. In order to electrodeposition Ni, consider the Pourbaix diagram (Basharat et al., 2015) show that the pH of electrolyte solution should be  $\leq 9$ . Hence, the pH of solution was determined to maintain at 3 by adding appropriate amount of HCl. Deposition temperature was maintained at 40-60 °C. A lower temperature than this range showed formation of nickel oxide layer in addition to the Ni.

In our experiment, we prepared the solutions using high purity chemicals (HCl, NiCl<sub>2</sub>, NaCl) and ultra-pure water ( $> 18 M\Omega cm$ ). Before the deposition, the sol-

utions were purged with high purity argon gas for 1 h to displace the dissolved oxygen in solution. The oxide layer on  $\text{Bi}_2\text{Te}_3$  surface, which is naturally formed in the atmosphere, is removed by peeling off with capton tape before install it into the electrochemical cell. A Pt plate was used as a counter electrode (CE) and Ag/AgCl was used as a reference electrode (RE). After mounting the substrate into the electrochemical cell, we routinely performed an electrochemical characterization of the  $\text{Bi}_2\text{Te}_3$  surface in a pure supporting electrolyte. Furthermore, after deposit nickel overlayers at a negative potential, the sample was rinsed with ultra-pure water. And the next step, MOKE measurements have been performed at room temperature.

### 3.3 Electrochemical measurements

In the second part of this thesis, the electrochemical properties of the prepared Ni/ $\text{Bi}_2\text{Te}_3$  sample were studied using a Autolab potentiostat galvanostat (PGSTAT 302N). The cyclic voltammetry (CV) techniques were used to investigate the appropriate bias potential for nickel deposition. We use three-electrode configuration which consists of the  $\text{Bi}_2\text{Te}_3$  substrate, a platinum wire (Pt) and silver/silver chloride (Ag/AgCl) electrodes used as working, counter, and reference electrodes, respectively. We used Nova software from Metrohm Autolab in measurement.

Cyclic Voltammetry (CV) is an effective technique to detect the reversibility of the electrochemical reaction, capacitance and its voltage dependence (Zheng, 2003). By applying a linear voltage ramp to an electrode and simultaneously measure the current. During the electrode potential (the potential difference between the reference electrode and working electrode) is scanned from initial value to final

value, the current passing between the working electrode and the counter electrode is recorded. Both current and potential are plotted as a typical fashion plot shown in figure 3.12. is named the voltammogram, which shows oxidation and reduction reaction or called redox reaction.

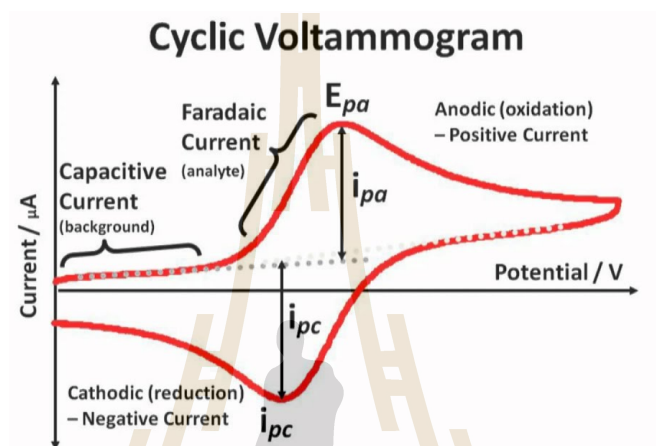


**Figure 3.12** Cyclic voltammogram of redox reaction (Adapted from <http://urrjaa.blogspot.com/2013/08/cyclic-voltammetry-urrjaa-p0110-2013.html>).

Another parameter of interest in all electrochemical systems is the reversibility. By using cyclic voltammetry, we can investigate the degree of reversibility of an electrochemical reaction. The electron transfer process in an electrochemical reaction is divided into three types: reversible, irreversible and quasi-reversible. In a reversible process, the rate of the electron transfer is higher than the rate of the mass transport. The ratio between the reverse peaks (cathodic peaks,  $I_{p,c}$ ) and the forward peaks (anodic peaks,  $I_{p,a}$ ) is constant and proportional to the concentrations of the active species. The current peak ( $i_p$ ) is described by the Randles-Sevcik equation (Brownson and Banks, 2014).

$$i_p^{rev} = 2.687 \times 10^{-5} n^{3/2} A C D^{1/2} \nu^{1/2} \quad 3.6$$

where  $n$ ,  $A$ ,  $C$ ,  $D$ , and  $\nu$  are the number of electron transferred/ molecule, the electrode surface area ( $\text{cm}^2$ ), the concentration ( $\text{mol}/\text{cm}^3$ ), the diffusion coefficient ( $\text{cm}^2/\text{s}$ ), and the potential scan rate ( $\text{V}/\text{s}$ ), respectively.

The potential of anodic ( $E_{p,a}$ ) and cathodic peak ( $E_{p,c}$ ) are not depend on the scan rate. The difference potentials between the forward and reverse peaks (named peak-to-peak separation),  $\Delta E_p$ , at all scan rates is equal to

$$\Delta E = E_{p,a} - E_{p,c} = \frac{0.059}{n} V \quad 3.7$$

In an irreversible process, the mass transport is higher than the electron transfer and the electron transfer rate of the reverse scan is very slow. The current and potential of peak are given by

$$i_p^{irrev} = 0.4958 n F A C D^{1/2} \left( \frac{\alpha n_a F}{RT} \right)^{1/2} \nu^{1/2} \quad 3.7$$

$$E_p = E^0 - \frac{RT}{\alpha n_a F} \left[ 0.78 - \ln \frac{K^0}{D^{1/2}} + \ln \left( \frac{\alpha n_a F \nu}{RT} \right)^{1/2} \right] \quad 3.8$$

where  $\alpha$  is the transfer coefficient and  $n_a$  is the number of electrons in the charge transfer process.  $\alpha$  is transfer coefficient,  $R$  is gas constant ( $8.3145 \text{ J}/\text{mol K}$ ),  $F$  is faradays constant ( $96,500 \text{ C}/\text{mol}$ ) and  $T$  is temperature ( $\text{K}$ ).

In this work, the cyclic voltammetry measurement was performed at a potential window in the range of  $-1.0 \text{ V}$  to  $0.3 \text{ V}$  at scan rates of  $30 \text{ mV}/\text{s}$  were applied in an aqueous of  $40 \text{ mM}$  Nickel chloride containing  $5 \text{ mM}$   $\text{NaCl}$  at  $50 \text{ }^\circ\text{C}$ . To study and identify the suitable potential difference for electroless deposition of  $\text{Ni}$ .

### 3.4 Scanning electron microscopy (SEM)

The scanning electron microscopy (SEM) technique utilizes a focus electron beam to generate signals electron at the surface of a specimen, as shown in figure 3.13. The signals electron caused by electron-sample interaction reveals the surface morphology of the specimen, chemical composition and crystalline structure. The electrons beam that is produced by a field emission source are accelerated in a field gradient. The beam passes through electromagnetic lenses, focusing onto the specimen resulting in bombardment. The result of bombardment cause different types of electrons are emitted from the specimen include secondary electron (SE), backscattered electron (BSE), diffracted backscattered electrons (EBSD). The most common signals used for imaging are secondary electrons, backscattered electrons, and characteristic X rays. Moreover, the secondary electrons depend on the incidence angle, and generate topographic information. The electron detector gains the secondary electrons to construct the image of surface by comparing the intensity of secondary electrons with the scanning primary electron beam (Yu et al., 2013) (Frackowiak, 2007). In this work, the morphologies of samples were obtained using scanning electron microscope (SEM. JSM-7800F).

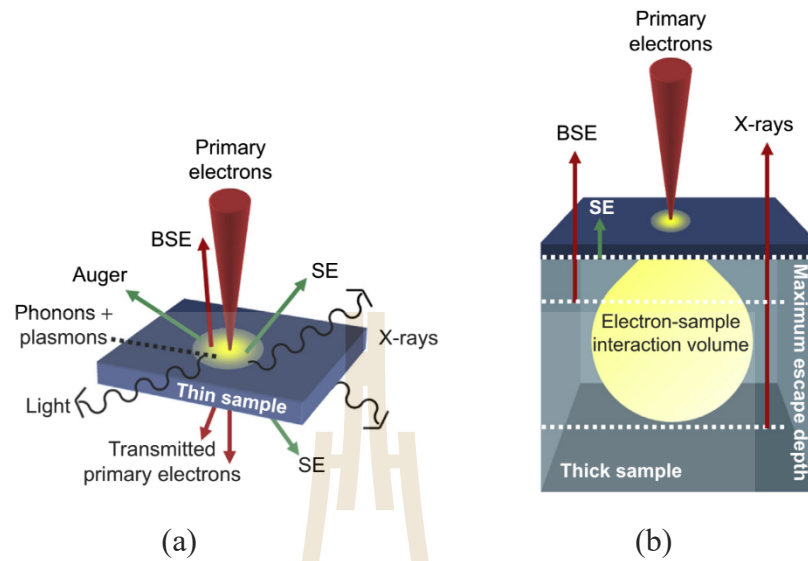


**Figure 3.13** The interaction of primary incident electrons with a sample. (a) Signals generated by electron-matter interactions (b) Absorption of SE, BSE, and X-rays by inelastic scattering within the interaction volume, determine the depth of electron escape (Inkson, 2016).

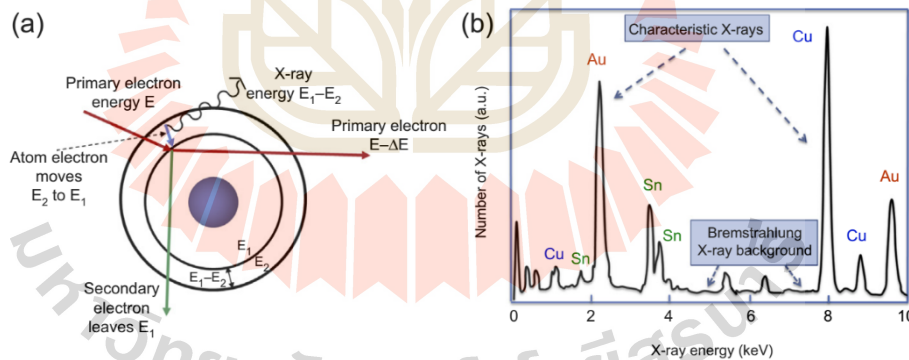


**Figure 3.14** Electron-induced X-ray emission. (a) Characteristic X-ray emission. Characteristics X-ray are emitted when outer shell electron moves to fill the empty electron energy level emptied by the secondary electron. (b) Schematic figure of an energy dispersive X-ray (EDX) spectrum of characteristic X-rays at several specific energies (Inkson, 2016).

### 3.5 X-ray diffraction (XRD)

X-ray diffraction (XRD) is used to determine the crystal structure of materials. An X-ray diffractometer can detect X-ray diffraction pattern of materials and the diffraction intensity as a function of the diffraction angle ( $2\theta$ ). When X-ray beams incident on a crystalline solid, it is reflected at atom in the crystallographic planes, as illustrated in figure 3.15. The constructive and destructive interferences occur if a phase difference is equal to  $n\lambda$  (in phase) and  $n\lambda/2$  (out of phase) resulting in diffraction. The following relationship of diffraction is satisfied by Bragg equation

$$2d\sin\theta = n\lambda \quad 3.9$$

Where  $d$  is the spacing between the parallel crystal planes,  $\theta$  is the angle of incident beam,  $\lambda$  is the wavelength of the incident X-ray beam and  $n$  is an integer. The various of peaks located at different  $2\theta$  position compared as a 'fingerprint' of a crystalline solid. Crystallinity and phases identification of a specimen is determined by comparing the spectra of known crystalline substances with our specimen diffraction spectrum (Leng, 2013).

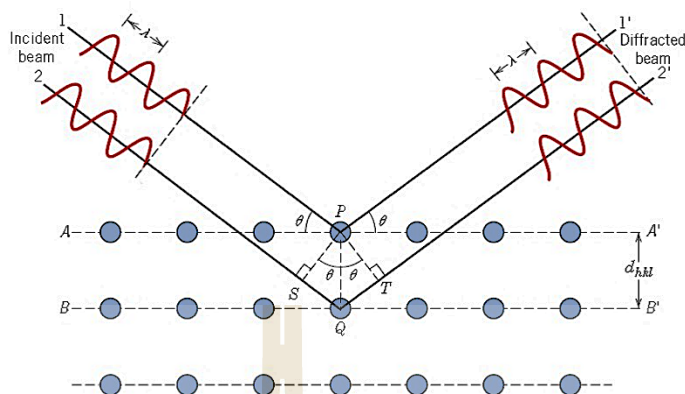


**Figure 3.15** Bragg diffraction by crystal planes.

In this thesis, we used X-ray diffractometer to analyse the structure of the BiFeO<sub>3</sub> sample. X-ray diffractometer is XRD (D2 Advance Bruker) with Cu K $\alpha$  at  $\lambda = 0.15406$  nm. The XRD pattern were recorded in the  $2\theta$  of  $10^\circ$ - $70^\circ$  with the step size of  $0.02$  degree and the time step of  $0.5$ s. The crystallinity and phase identification was performed by comparing with the data of the Joint Committee on Powder Diffraction Standards (JCPDS) diffraction.

### 3.6 In-situ X-ray absorption spectroscopy

X-ray absorption spectroscopy technique is an effective technique for study the electronic structure and local structure. The principle of XAS can be described simply as using the efficiency photon energy of X-ray to reject a core electron from an original electronic level and measure the signal emitted.

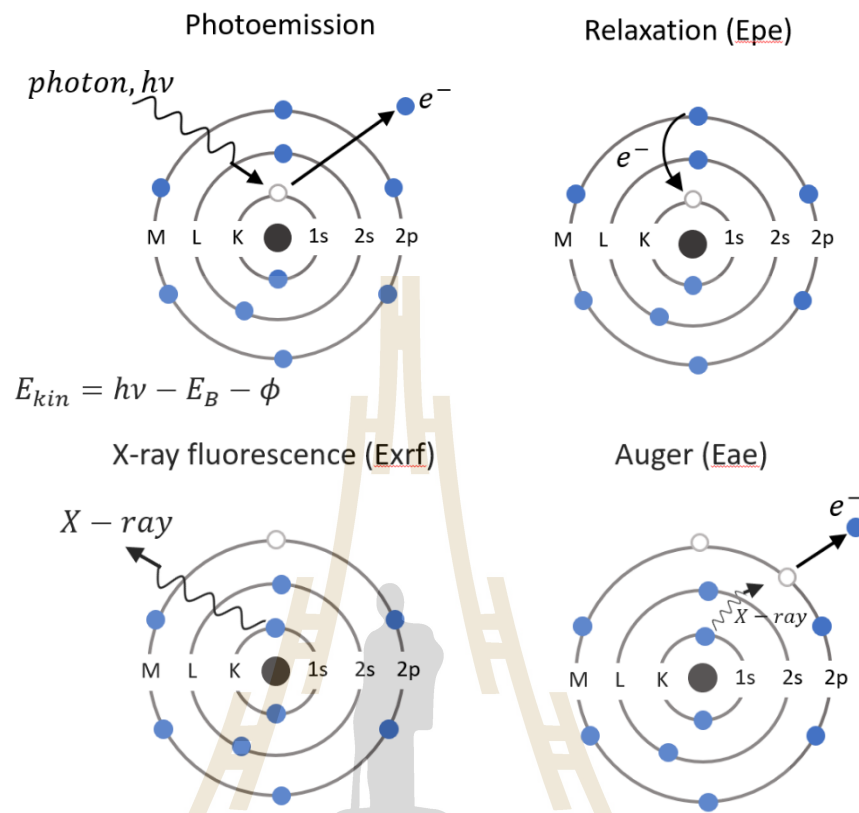


**Figure 3.16** The schematic processes stimulated by X-ray which include photoemission, X-ray fluorescence and Auger electron emission where  $h\nu$  is the incident photon,  $E_{ae}$  is the energy of the outgoing Auger electron ( $E_{ae} = E_K - E_L - E_M$ ),  $E_p$  is the energy of the outgoing photoelectron or relaxation ( $E_p = h\nu - E_K - E_M$ ),  $E_{erf}$  is the energy of the outgoing fluorescence photon ( $E_{xrf} = E_K - E_M$ ) and  $E_K$ ,  $E_L$  and  $E_M$  are the energies of the K, L, and M orbitals respectively.

In this technique, a parallel monochromatic X-ray beam of intensity  $I$  passing through a sample of thickness  $x$ . The intensity is reduced to be  $I$  following the equation.

$$I = I_0 e^{-\mu x} \quad 3.10$$

where  $I_0$  is the incident X-ray intensity and  $\mu$  is the linear absorption coefficient namely it is the probability of absorption.

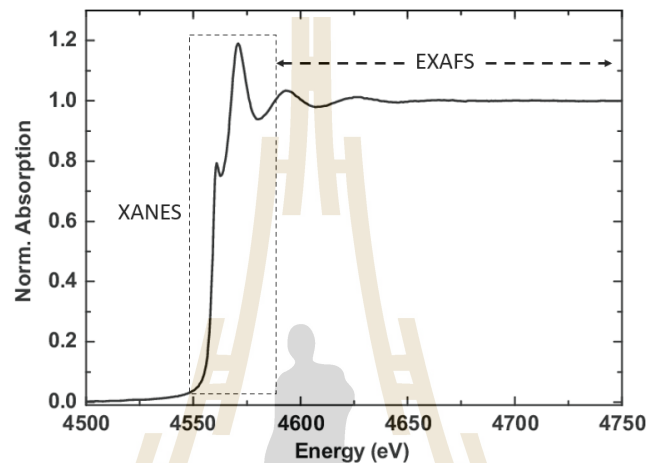


**Figure 3.17** XAS spectrum of L3-edge measured in transmission mode.

The X-ray absorption at constant energy increases dramatically when the photon energy corresponds to the electrons binding energy. Furthermore, at the same time results in a decrease of the transmitted X-ray intensity. The absorption edge appear when the incident photon energy is sufficient to excite a core electron to a higher energy. When we analyze the XAS spectrum, it can be separated into three main regions. In figure 3.17 show that the first region is at around 20-50 eV below the absorption edge, is called pre-edge structure. The pre-edge peak arised from the transition of electron to the lowest empty bound state near is the Fermi level. It indicates the local structure and electronic structure around absorber atom including the neighbor atoms or valence state.

The second region occurs when the photon energy of incident X-ray is sufficient to excite electrons of atomic core level to final states. This region is in the higher energy range, about 40- 100 eV above an absorbed atomic core level of ionization energy. We call this region that X-ray absorption near edge structure (XANES). The absorption edge in XANES spectra can provide information on the oxidation state and the absorbing atoms coordination number.

The third region is the region of the oscillation above the edge, which is known as the Extended X-ray absorption fine structure (EXAFS) (see in figure 3.17). In this region, the incident photon energy is enough to excite the core electron because of energy is equal or higher than the edge energy. Because many atoms around the absorber atom behave as scattering centers of the photoelectrons wave, the final state of photoelectrons is contributed by the original and single scattered waves from the nearest neighboring atoms. We can extract the information of the interatomic distance, coordination number and species of neighboring atoms from EXAFS spectrum. The EXAFS is described as a function of the wave vector  $k$  as:

$$\chi^{(k)} = \sum_j \frac{S_0^2 N_j}{k R_j^2} |f_j(k, \pi)| \sin[2kR_j + \phi_j(k)] e^{-2\delta_j^2 k^2} e^{-2R_j/\lambda(k)} \quad 3.11$$

where  $N_j$  is the number of neighbors in  $j$  shell of surrounding atoms,  $k$  is photoelectron wave vector,  $f_j$  is the scattering amplitude,  $S_0^2(k)$  is the amplitude reduction term due to many-body effect,  $R_j$  is radial distance from absorbing atom to  $j$  shell,  $S_0^2(k)$  is electron mean free path,  $\sigma_j$  is the Debye-Waller factor and  $\phi(k)$  accounts for the total phase shift of the curve wave scattering amplitude along the scattering trajectory.

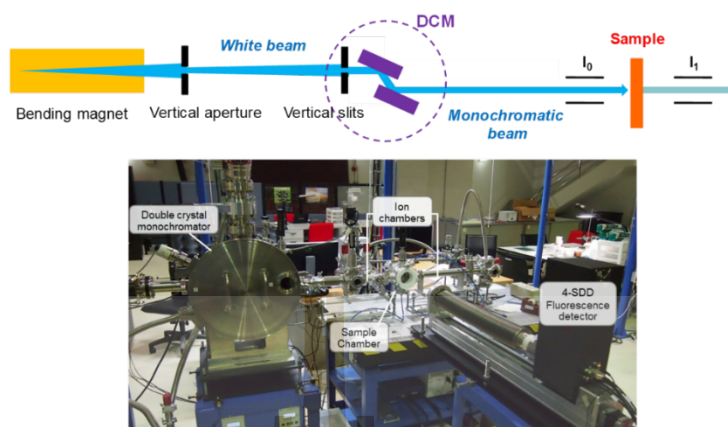


**Figure 3.18** XAS measurement system at SUT-NANOTEC-SLRI XAS beamline (BL-5.2), Synchrotron Light Research Institute (SLRI) of Thailand.

In this thesis, the XANES and EXAFS spectrum were collected at the SUT-NANOTEC-SLRI XAS beamline (BL-5.2), Synchrotron Light Research Institute (SLRI) of Thailand. We install the laser with wavelength 405 nm to illuminate the sample while measurement. All spectra of Ni K-edge were collected in fluorescent mode. The EXAFS spectra were transformed by Fourier transform to real space using  $k^3$ -weighting factor and a Hanning window.

# **CHAPTER IV**

## **THE STUDY OF KERR ROTATION IN BISMUTH FERRITE (BIFEO<sub>3</sub>)**

The results of experiment and discussion on the study of light sensitive materials are reported in this chapter. This chapter is divided into three sections: the first section presents the results of the instrument installation and the analysis of the instrument to confirm the measurement accuracy. The second section is the characterization of BiFeO<sub>3</sub>/SrRuO<sub>3</sub>/SrTiO<sub>3</sub> heterostructure. In this section, the experiment is devoted to characterizing BiFeO<sub>3</sub> sample and explaining the Kerr rotation of BiFeO<sub>3</sub> upon UV illumination. The BiFeO<sub>3</sub> film morphology are evaluated by scanning probe microscope (AFM) and piezoresponse force microscope (PFM) is used to investigate the piezoelectric response. The third section is the study of the light induced Kerr effect in BiFeO<sub>3</sub> film. The electronic structure of BFO which was placed upon ultra-violet illumination can be determined by using In-situ ultraviolet spectroscopy (UPS).

## 4.1 Experimental Investigation of MOKE

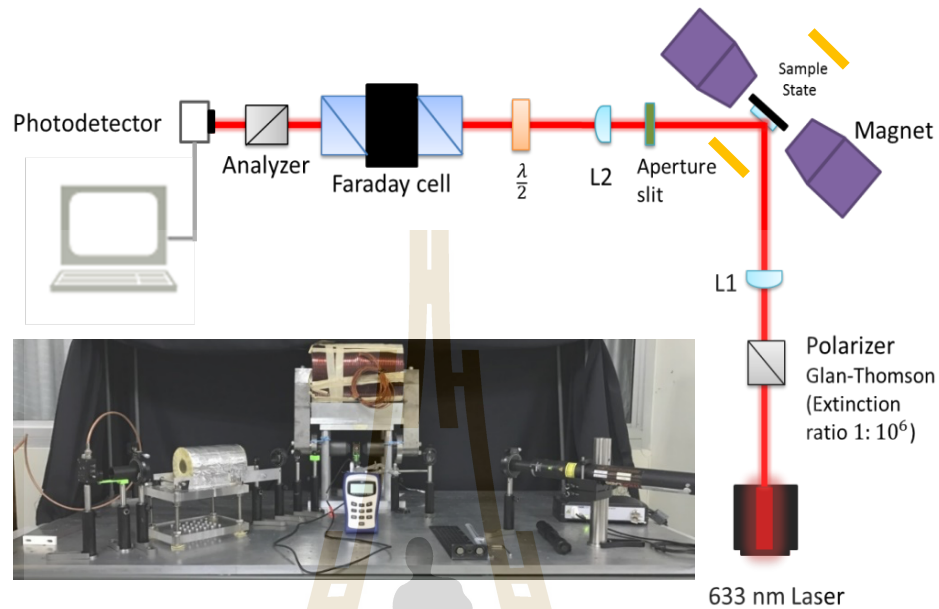


**Figure 4.1** Schematic illustration of longitudinal magneto-optical kerr effect (L-MOKE) measurements. the inset is photograph of L-MOKE.

One of the main objectives of this thesis is to set up a functional and reliable system to measure the magneto-optic Kerr effect. The standard method began with the MOKE arrangement, which forms the arrangement closest to Kerr's original experiment. Measurements to test this system were done on Fe films of different thicknesses. The hysteresis loops were confirmed by comparing with other works. These results were compared the shape and the hysteresis loop's coercive field with literary works. It showed that our MOKE setup was accurate in the measurement of normalized magnetization and the coercive field.

#### 4.1.1 Magnetic hysteresis loop measurement

The Fe film with different thicknesses was deposited using Molecular Beam epitaxial (MBE) techniques by controlling the thickness to equal 20 nm and 5 nm. The MOKE measurement was performed with four different angles using the methods described earlier. The result indicates the magnetic anisotropy, remnant magnetization, saturation field, coercive field, and the measured samples' squareness (see figure 4.2 and 4.3). The MOKE system's main testing was to compare the two films deposited with the same target to confirm the similarity and coercive fields. The results of the comparison show that the films produced similar hysteresis loops corresponding to the literature reports.

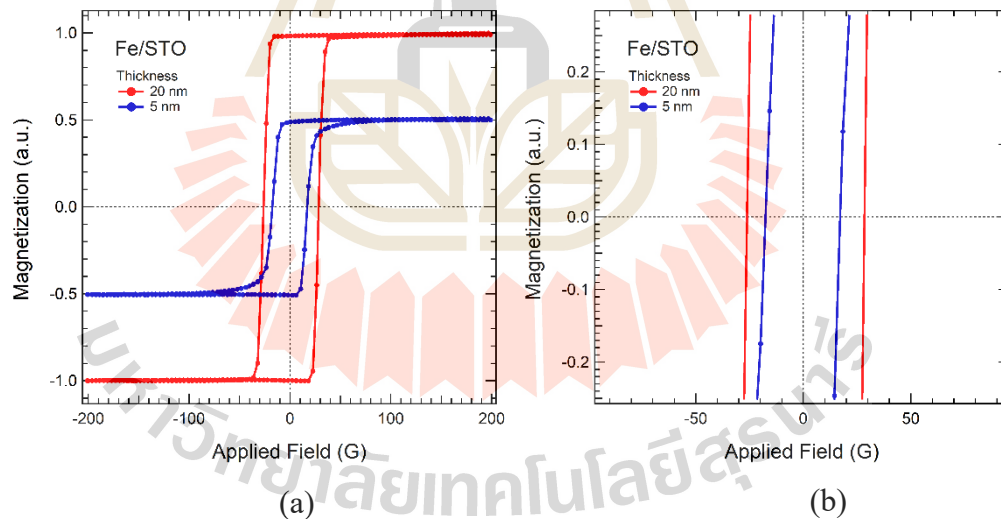


**Figure 4.2** Field dependence of the magnetization  $M$  in  $B$  parallel to surface of Fe films in the external applied magnetic field -200G to 200G (a) and a partial enlarged curve (b).

We compared the two films which consist of the same composition to confirm the similarity and optical alignment. The comparison between the  $0^\circ$  or indentation of the first Fe film and of the  $45^\circ$ ,  $53^\circ$ ,  $60^\circ$ ,  $90^\circ$  incident angle show similar hysteresis loops. We used LabView program to control the electronics component of MOKE system and collect high-resolution data through several loops measurement and sum over the intensity. This method gives a normalized hysteresis loop without loss of the detail. The magnetic hysteresis loop of several angular orientations of the Fe films with respect to the plane of incidence show in figure 4.3.

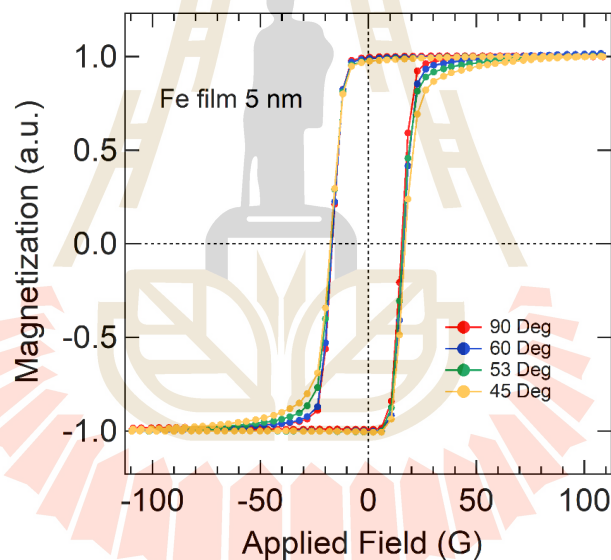
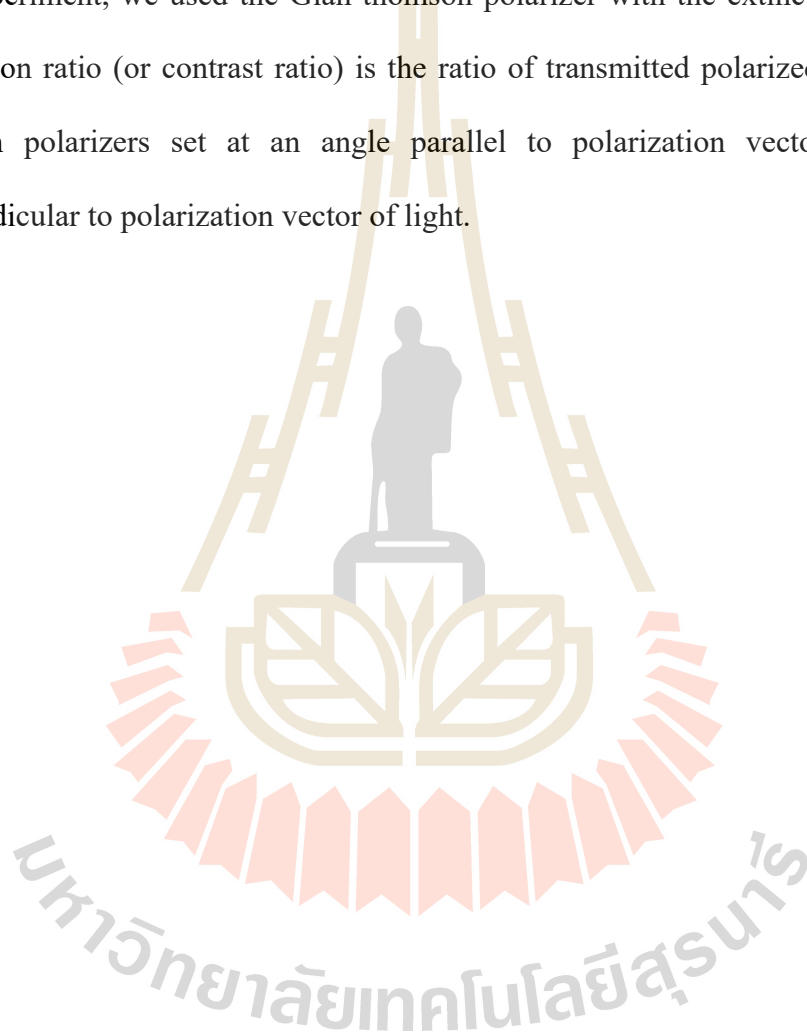


**Figure 4.3** Normalized hysteresis loops of Fe film at the angles of  $45^\circ$ ,  $53^\circ$ ,  $60^\circ$ ,  $90^\circ$  orientation.

According to the theoretical description, the DC curves are a direct result of the Kerr effect, therefore we get enough estimate of the Kerr rotation using Malus' law, which used to calculate the angle between two polarizers and estimate the DC Kerr effect. However, in our experiment, instead of calculating the angle between two polarizers, the angle between the polarizer and the analyzer is determined using the

calibration curve. By carefully measuring intensity versus the analyzer angle through manual rotation, the angle of the analyzer at the maximum variation was set. This measurement however is just an estimate but enough to study the magnetism of thin films. It was found to be highly dependent upon the extinction ratio of the analyzer. In our experiment, we used the Glan-thomson polarizer with the extinction ratio  $1:10^6$ , extinction ratio (or contrast ratio) is the ratio of transmitted polarized light intensity through polarizers set at an angle parallel to polarization vector to an angle perpendicular to polarization vector of light.

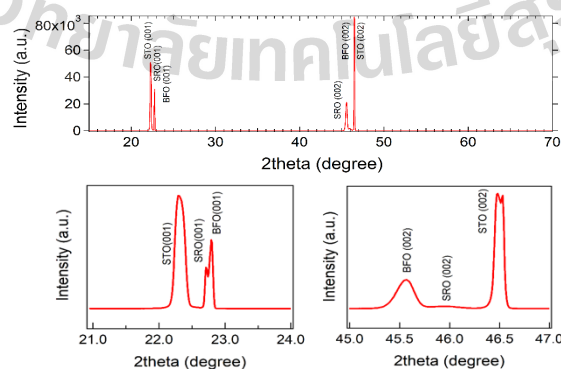


## 4.2 Characterization of BiFeO<sub>3</sub>/SrRuO<sub>3</sub>/SrTiO<sub>3</sub> heterostructure

### 4.2.1 Details of BiFeO<sub>3</sub>/SrRuO<sub>3</sub>/SrTiO<sub>3</sub> fabrication

In this experiment, we took the example given by Dr. Wittawat Saenrang, BiFeO<sub>3</sub>/SrRuO<sub>3</sub>/SrTiO<sub>3</sub> were prepared starting with (001) SrTiO<sub>3</sub> single-crystal substrates with 4° miscut toward [110]<sub>pc</sub> direction (Baek et al., 2010). A 35 nm thick SrRuO<sub>3</sub> (SRO) bottom electrode layer is deposited by 90° off-axis sputtering (Eom et al., 1989) at 600 °C followed by 400 nm of BiFeO<sub>3</sub> (BFO) films grown by double-gun off-axis sputtering at 750 °C with Ar:O<sub>2</sub> ratio of 4:1 at a total pressure of 400 mTorr (Das et al., 2006). In sputtering process, we used BiFeO<sub>3</sub> target contains 5% excess Bi<sub>2</sub>O<sub>3</sub> to compensate for bismuth volatility (Das et al., 2006). The substrate miscut caused the growth of a single ferroelastic domain variant, while the SrRuO<sub>3</sub> bottom electrode induced an electrical boundary condition caused the ferroelectric down r1 – state (Baek et al., 2010) because of the depolarization field can be screened by free charge at the electrode during film growth (Fong et al., 2006).

### 4.2.2 Crystal structure characterization by X-Ray diffractometer (XRD)



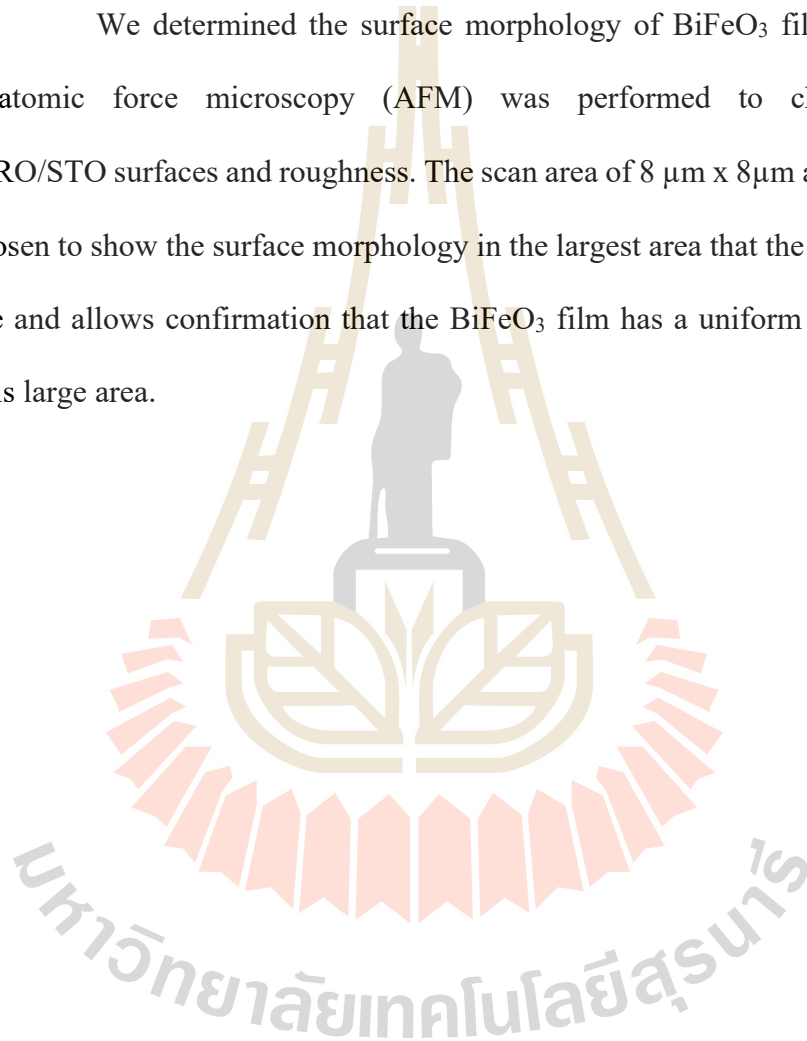
**Figure 4.4** The XRD spectra of BFO/SRO/STO (001) mono domain film.

Figure 4.4(a) shows X-ray diffraction pattern scanned in the  $\theta$ - $2\theta$  range of BFO film grown on SRO film with sputtering technique on (001) - STO substrate. The sample's primary diffraction peak indicates (001) - and (002) - the STO surface. The BFO film shows the peaks (001) and (002) corresponding to the substrate without any secondary phase. This reveals the BFO film has a direction (001) along with the normal orientation of the substrate in BFO film on SRO (001) / STO (001). Moreover, we can distinguish (002) the BFO, SRO, and STO peak due to the SRO off-plane lattice parameters, which grow by sputtering equal to 0.399 nm in pseudocubic symmetry. This result indicates the relationship between epitaxial cube-on-cube as follows: BFO (001)/SRO(001)/STO(001). Clearly, the XRD peaks are good agreement with previous work (Yuan et al., 2009). Moreover, the stain in the BFO/SRO/STO heterostructures was extracted from XRD patterns. According to literature review, no epitaxial strain SRO ( $\delta \sim 0$ ) thick film film has the pseudocubic crystal lattice equal to  $\sim 0.3922$  nm, STO( $\delta \sim 0$ ) crystal substrate  $\sim 0.3906$  nm, and  $\sim 0.3965$  nm for BFO ( $\delta \sim 0$ ) crystal (Chu et al., 2006; Wang et al., 2003; Zhao et al., 2006). Figure 4.2(b) show that 002 diffraction peaks of BFO film are slightly higher than (or close to) the  $45.770^\circ$  expected for BFO ( $\delta \sim 0$ ) crystal, indicating that our BFO films are weakly strained (namely is relaxed by a higher  $\delta$ ). To analyze the evidence of small compressive strain in BFO/SRO/STO, the 002 diffraction peaks of BFO films was fitted by a peak with  $2\theta_{002} \leq 45.57^\circ$  yield c axis is larger than  $0.3979$  nm, which close to c-axis of BFO crystal mean that the relaxation of compressive strain between the BFO film and the SRO layer. We suggest that this effect may be induced by the density of oxygen vacancy

( $V_{Os}$ ) that is enough to relax the compressive strain and when  $V_{Os}$  diffused to SRO, it induced the lightly expanded c axis.

#### 4.2.3 Surface Structure Analysis by Atomic Force Microscope

We determined the surface morphology of  $\text{BiFeO}_3$  film in the virgin state, atomic force microscopy (AFM) was performed to characterize the BFO/SRO/STO surfaces and roughness. The scan area of  $8\ \mu\text{m} \times 8\ \mu\text{m}$  and  $2\ \mu\text{m} \times 2\ \mu\text{m}$  was chosen to show the surface morphology in the largest area that the microscope can observe and allows confirmation that the  $\text{BiFeO}_3$  film has a uniform domain at least over this large area.



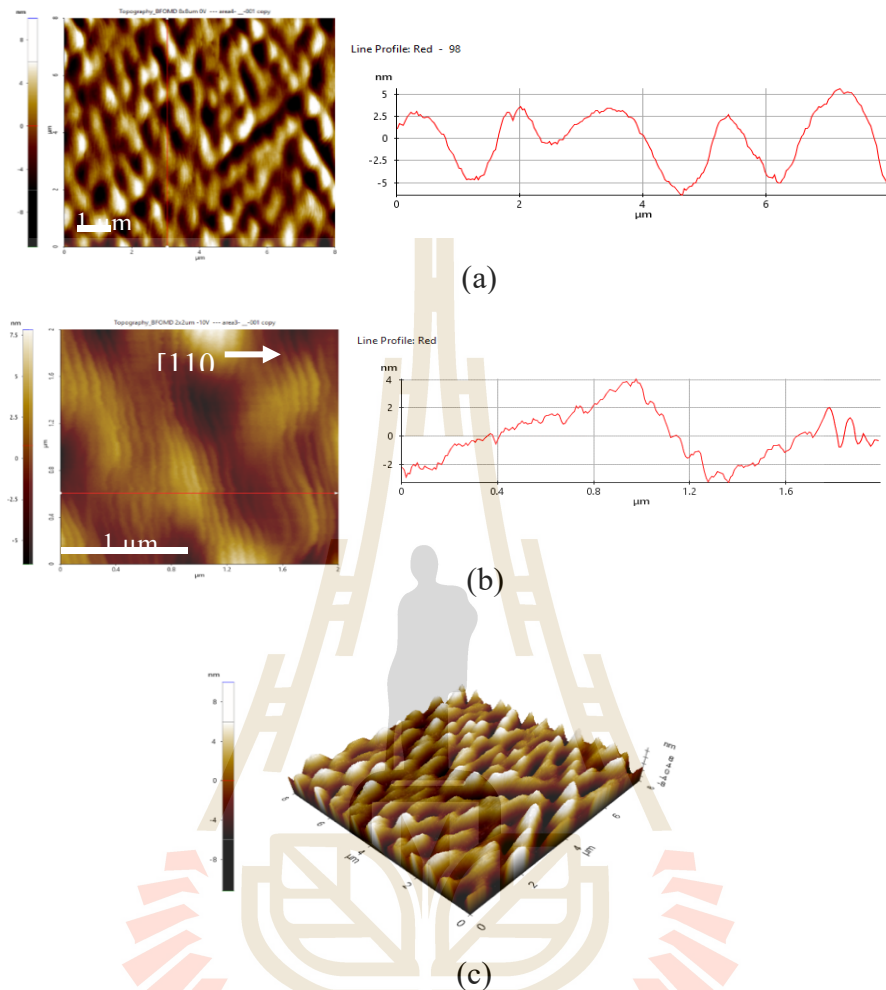


**Figure 4.5** Surface morphology of the heterostructures. Atomic force microscope (AFM) images showing smooth surface morphology of both as-grown BiFeO<sub>3</sub> (RMS roughness  $\sim$  4.0 nm). Scale bar equal to 1  $\mu$ m. Step bunching occurs to accommodate structural relaxation during BiFeO<sub>3</sub> growth on miscut SrTiO<sub>3</sub> substrates in area 8x8  $\mu$ m (a), 4x4  $\mu$ m (b), and 3D image of morphology (c).

Microscopic analysis by atomic force microscope is quantitatively measurement for surface roughness in nanoscale dimension and for the surface texture visualization. We measured the surface texture of BFO films with horizontal length scale of 4 microns and a vertical length scale of 5 nm which is not impact to optical properties. The AFM image was scanned in an AC scanning mode with a deflection set point of 0.2 V and at a scanning rate of 0.5 Hz. The spring constant of the tip is 2 N/m. The surface morphologies of BFO film are shown in Figure 4.5(a)-(b). It shows that the surfaces are smooth enough for PFM scanning and no random defect. The image shows the uniform distributed shape of the hills and valleys. Three-dimensional (3D) AFM images is shown in Figure 4.4(c). The surface roughness of BFO films equal to 4 nm, without any changes of surface morphology when the sample is under UV laser. On right hand side of Figure 4.4(a)-(b) show an analysis of the roughness derived from the XEI program of XEI' s Park System.

#### 4.2.4 Piezoresponse force microscope (PFM) analysis.



**Figure 4.6** PFM image showing polarization domain structures of (001)-oriented  $\text{BiFeO}_3$  film.

The piezoresponse force microscope (PFM) is performed to illustrate the piezoelectric response of BFO film. The resolved amplitude image of BFO films sample exhibit a piezoelectricity derived from PFM amplitude histogram. In figure 4.6, PFM phase images of the out-of plane polarization show the majority amount of the monodomains in BFO films are oriented with the polarization upward (bright brown), and domains containing the polarization oriented downward (dark brown). The schematic of scan area is shown. After switching from up to down polarization state of the middle area, the out-of-plane PFM images show the same contrast as the unswitched area. This confirms that the polarization of the switched area from up to down state has the same polarization as the virgin state. This confirmation is useful to study a one-to-one correlation between order parameters of  $\text{BiFeO}_3$  to exploit deterministic light coupling without the complicated effect caused by domain walls. The previous experimental and theoretical studies demonstrated that rotation of  $\mathbf{P}$  away from the  $[111]_{\text{pc}}$  towards the  $[001]_{\text{pc}}$  direction caused by an in-plane compressive strain (Ederer and Spaldin, 2005; Jang et al., 2008). When the  $c/a$  ratio exceeds 1.1, the  $\mathbf{P}$  has been found to be almost parallel to the  $c$  axis (Hatt et al., 2010; Zhang et al., 2011). Moreover,  $\text{BiFeO}_3$  possessing the ferroelectric monodomain also exhibits a single antiferromagnetic domain with the propagation vector along the film's plane and a spin-cycloid orientation that differs from bulk single crystals (Saenrang et al., 2017).

### 4.3 Magnetic-optical effect (MOKE) measurement

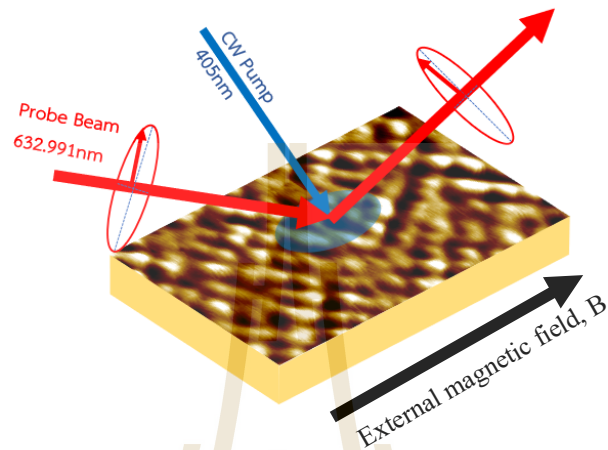


**Figure 4.7** Schematics of MOKE experiment configurations for magnetic field applied parallel to the surface.

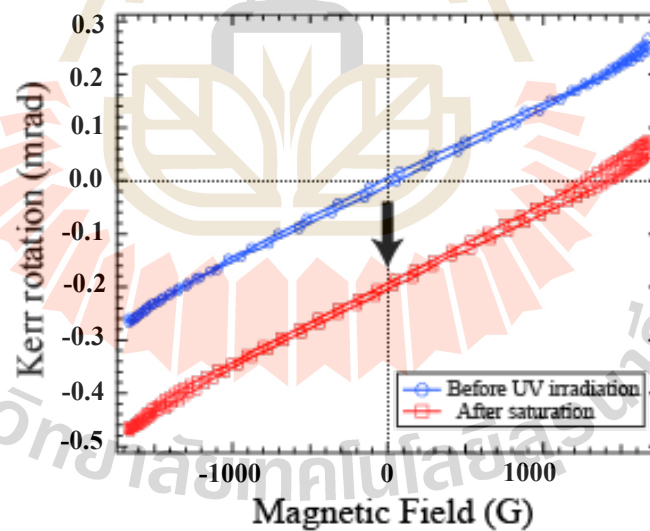


**Figure 4.8** Magneto-optical hysteresis loop measured by MOKE for a BFO/SRO/STO film, measured in external range -1600G to 1600G at RT.

Kerr rotation of epitaxial BFO/SRO/STO heterostructure thin films was performed in magnetic field from -1600G to 1600G at room temperature following the

configuration shown in figure 4.7. The probed signal was measured via modulation of a lock-in amplifier and then be subtracted the background signal by comparing with Kerr rotation of the aluminium mirror. We observed the variation of Kerr angle upon increasing the external magnetic field. The change in Kerr angle reaches around 0.52 mrad at  $B_{ext} = 1600\text{G}$  comparing with at  $B_{ext} = -1600\text{G}$ . A small coercivity (loop) is observed, consistent with previous reports (Catalan and Scott, 2009; Lu et al., 2010; Shimada et al., 2014; Yan et al., 2015). The plot shows linear characteristic in low magnetic field range and passes through the origin, representing that our film exhibits a good magneto-optical response with high resolution. Clearly, M-H curve indicate that surface of sample behaved like weak ferromagnetic at 300K. The small spin canted moment in  $\text{BiFeO}_3$  ( $\sim 0.06 \mu_B \text{ Fe}^{-1}$ ) (Ramazanoglu et al., 2011) caused by the Dzyaloshinskii-Moriya interaction (Dong et al., 2009; Rahmedov et al., 2012). Normally, the spin-cycloid structure in  $\text{BiFeO}_3$  single crystal make the net moment averages to be zero over a cycloid period ( $\sim 62 \text{ nm}$ ) (Catalan and Scott, 2009). The suppression of the spin cycloid in BFO/SRO/STO heterostructure e.g. due to strain in this film, give rise to the formation of collinear G-type ferromagnetic order which orthogonal ferroelectric polarization vector ( $\vec{P}$ ), Neel vector ( $\vec{L}$ ), and canted moment ( $\vec{M}_c$ ) together induce the intrinsic weak ferromagnetism in  $\text{BiFeO}_3$  (Ramazanoglu et al., 2011; Saenrang et al., 2017).

Moreover, based on this optical equipment layout of MOKE, we utilized a magneto-optical Kerr magnetometer (MOKE) as an instrument to observe the Kerr rotation in a additional designed device to measure the Kerr rotation of epitaxial BFO/SRO/STO thin films upon ultraviolet laser (wavelength 405nm) illumination. To

study the interesting phenomenon, which is named as light-enhanced Kerr rotation effect. Laser with wavelength of 405 nm was installed along the direction perpendicular to the surface. The result shown the effect of laser induced Kerr rotation by two-fold magnitude at a light intensity equal to  $500\text{mW}/\text{mm}^2$ . Interestingly, As can see, the vertical shifting of magneto-optical hysteresis loop to lower as well as higher depending on the angle of polarizer (discussed in Figure 4.9). This vertical shifting is due to the constant additive of the polarization plane rotation angle. Moreover, we also found that this additive doesn't depend on the direction and magnitude of the external magnetic field.

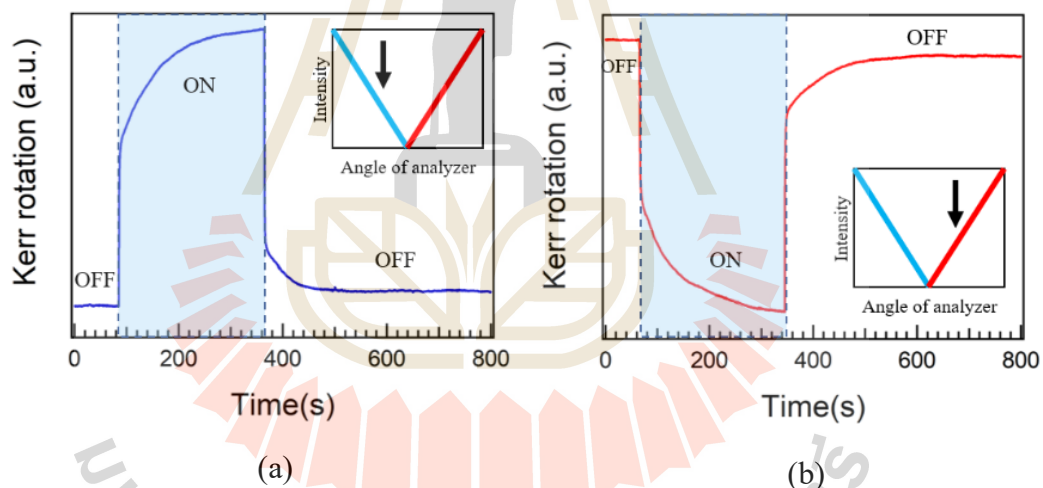


**Figure 4.9** Angle of analyzer setting(a) right (forward setup) (b) left (backward setup) of Kerr angle measurement under ultraviolet illumination.

Figure 4.9(a) and (b) show the results of the analyzer (Glan-Thomson polarizer with extinction ratio  $1:10^6$ ) angle adjustment, which give the different direction signal. We take advantage of this setting to ensure that the polarization plane of reflected light indeed rotated.

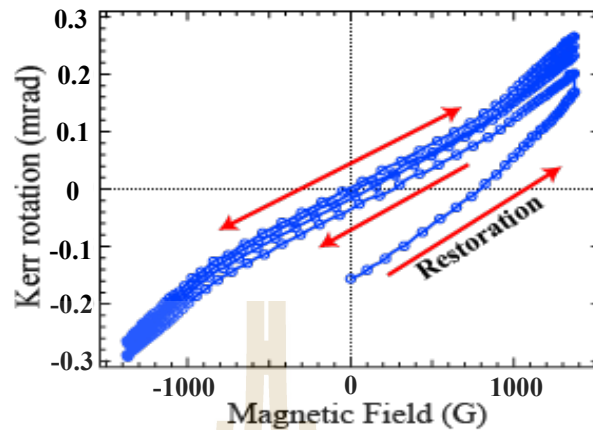


**Figure 4.10** Restoration of Kerr rotation variation after turn off UV laser.

The variation of Kerr rotation gradually decreases among UV irradiation time which is shown in Figure 4.10. Before and after UV irradiation, the hysteresis loop indicates the change of Kerr angle; however, the slope of the graph remains the same. This behavior indicates no difference of susceptibility, which may refer to electric field domination rather than magnetism. Kerr angles gradually change under UV irradiation (power density  $180 \text{ mW/mm}^2$ ) and saturated with the change of kerr angle to be around  $0.23 \text{ mrad}$  for forward setup. This effect is opposite for the backward optical polarizer setup, indeed indicates the rotation of the optical polarization plane of reflected from BFO/SRO/STO.

According to literature reports, the gradually occurrence of internal electric field can approximated via bulk photovoltaic measurement in which BFO has been report  $V_{oc}$  of single domain BFO equal to  $-0.25\text{V}$  which converted into electric field equal to  $19.2\text{kV/cm}$  (Guo et al., 2020; Zhou et al., 2014) and in multi-domain equal to  $-7\text{V}$  in the perpendicular geometry (Yang et al., 2017). And for parallel geometry measurement, it was found that single crystal BFO exhibited a  $V_{oc}$  of  $-28\text{V}$  in its pristine state, which is above the band gap (Yang et al., 2015). Moreover, it has been reported

that light can induced the photovoltaic effect in BFO depend on two competitive contribution i.e. ferroelectric polarization leading to increment of the internal bias field caused by a nonuniform distribution of oxygen vacancies (Ji et al., 2010) and electric field screening by the light generated charges as an electric polarization averages reduction in the sample (Kundys, 2015).

Moreover, it was known that all the BFO thin films show linear electro-optic (EO) behavior which strong response to the electric field orientation (Zhu et al., 2015). The electric field induce refractive index linearly changes namely pockels effect also resulting in plane of laser polarization rotation. The field-induced refractive index changes (birefringence) is given by  $\Delta n = -\frac{1}{2}n^3r_{eff}E$  where  $n$  and  $E$  are the refractive index and the applied electric field, respectively. At this point of view, we believed that the electric field arising from the photovoltaic effect can drive EO response in BFO. Although the electric field obtained from the photovoltaic effect is much smaller than the ferroelectric coercivity, however, to prove that a small electric field produced by the photovoltaic effect can cause a change in the refractive index through the MO phenomenon, we experimented with applied the small electric field in the perpendicular direction. The results of this study will be discussed in section 4.5.

#### 4.4 Summation of magnetic and electric (laser) fields via Kerr angle

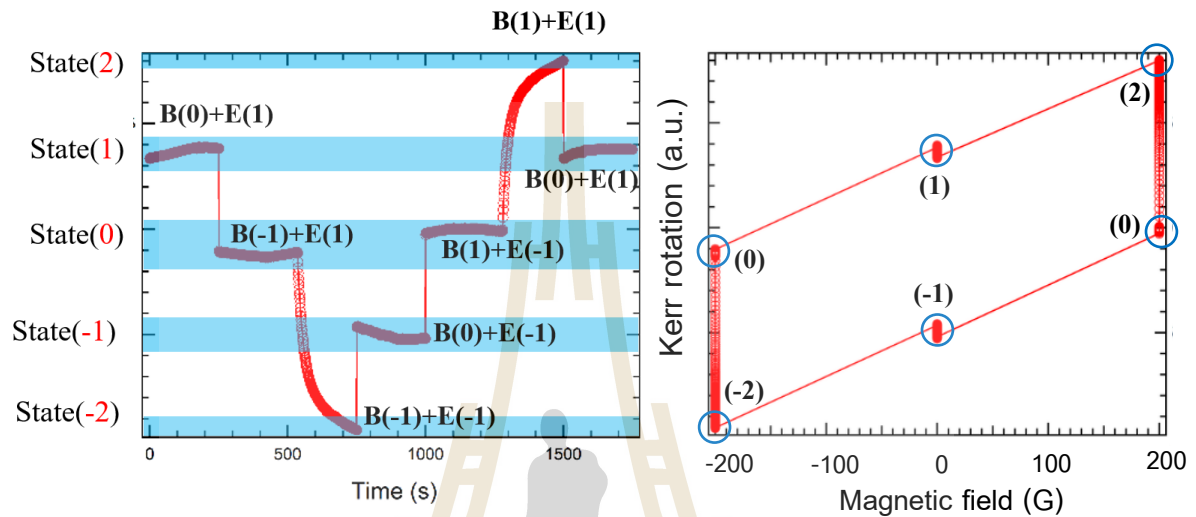


**Figure 4.11** (a) Utilization of Kerr angle rotation. (b) magneto optical coupling at constant external magnetic field -200G and 200G.

In this part of experiments, we can add or subtract the Kerr angles rotation resulting from both magnetic field and laser irradiation. In the graph, we can add magnetic field state 0 and electric field state 1, and the result will be state 1; adding magnetic field state -1 and electric field state 1, the result will be in state 0, adding magnetic field state -1 and electric field state -1, the result will be in state -2 and so on. As far as we are aware, this is the first time showing that we can couple both magnetic and electric fields via Kerr rotation. This result also promises a new type of device that a couple of magnetic fields, electric fields, and laser irradiation. we present a possible implementation of optically induced Kerr rotation and magneto-optical Kerr rotation in single phase  $\text{BiFeO}_3$  to fabricate multi-state at room temperature. Namely, this state

could be written by applying ultraviolet laser with wavelength 405 nm and magnetic field, and read out by measuring its Kerr rotation signal.

In this graph (figure 4.11(b)), a constant external magnetic field of -200G and 200G is placed under the laser on and off. The resulting data are plotted on the axis of the magnetic field and the Kerr rotation. In the graph, the Kerr angle due to a combination of the light-induced Kerr rotation with magnetic field-induced Kerr rotation show to be six states.

#### 4.5 In situ Kerr rotation measurement under external electric field and laser application.

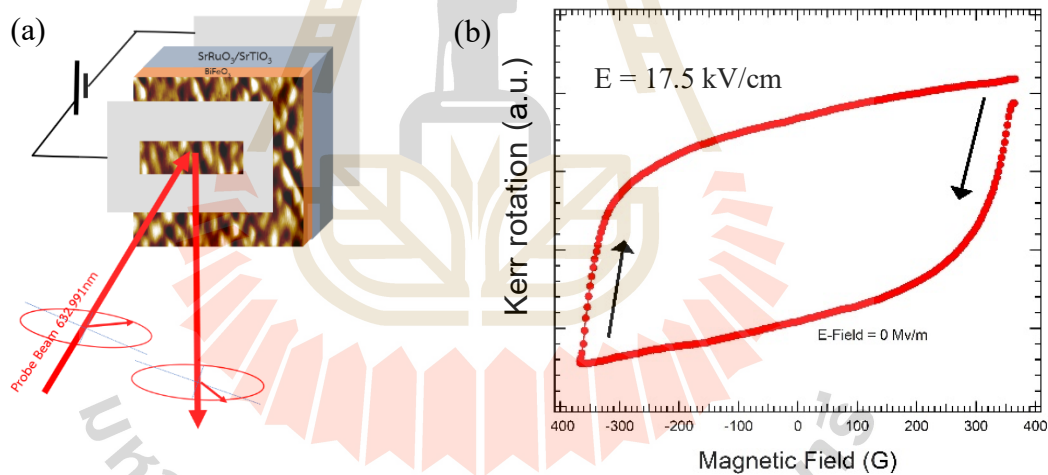


**Figure 4.12** Schematics of MOKE experiment configurations for magnetic field applied perpendicular to the BFO/SRO/STO surface (a). electric-optic coupling of BFO/SRO/STO via measured Kerr angle (b).

Magnetic hysteresis Kerr loop was performed under external constant electric field application. Figure 4.12(a) show schematic configuration of Kerr signal measured with a bias electric field of 17.5 kV/cm. Constant electric field was applied while

hysteresis loop measurement while external magnetic field (figure 4.12(b)), the external electric field with magnitude 17.5 kV/cm was applied while external magnetic field equal to -360G until to 360G, then the external electric field was turn off. This result shows the magnetoelectric coupling via Kerr rotation in characteristically linearly summation resulting in the vertical shift of Kerr rotation similar to light induced Kerr rotation.

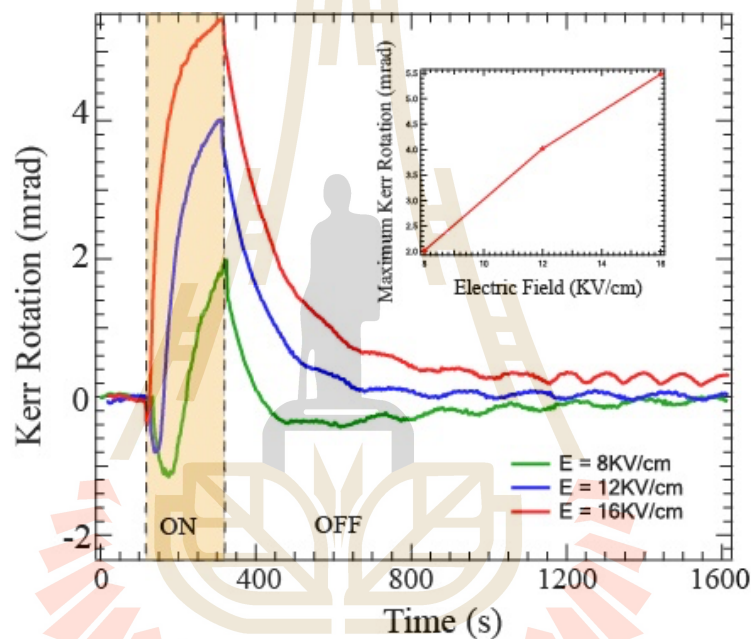


**Figure 4.13** The time resolve Kerr rotation of BFO which respond to the external electric field at different external electric field.

Time resolve measurements of Kerr angle variation in a BFO were carried out for different magnitudes of the bias electric field in order to study the coupling between the Kerr rotation and the electrical field. A bias field of 8KV/cm, 12KV/cm, 16KV/cm, respectively, was applied perpendicular to the surface. The dependence of the Kerr rotation enhancement upon the field strength shown in the figure 4.13, change in Kerr angle as a function of applied electric field was indicated. The change in Kerr rotation

with respect to the increase in the external electric field can be observed. For more detail, the Kerr rotation suddenly increases as the electric field is turn on, and then Kerr angle gradually drop as the electric field is turn off. This result indicates that Kerr effect in BFO can be induced by applied external electric field. The present of local polarization variation in BFO/SRO/STO, although an external applied electric field is not as strong as the remanent polarization coercive field of  $\text{BiFeO}_3$ . Our data are compatible with optical induced Kerr rotation results (Figure 4.16).

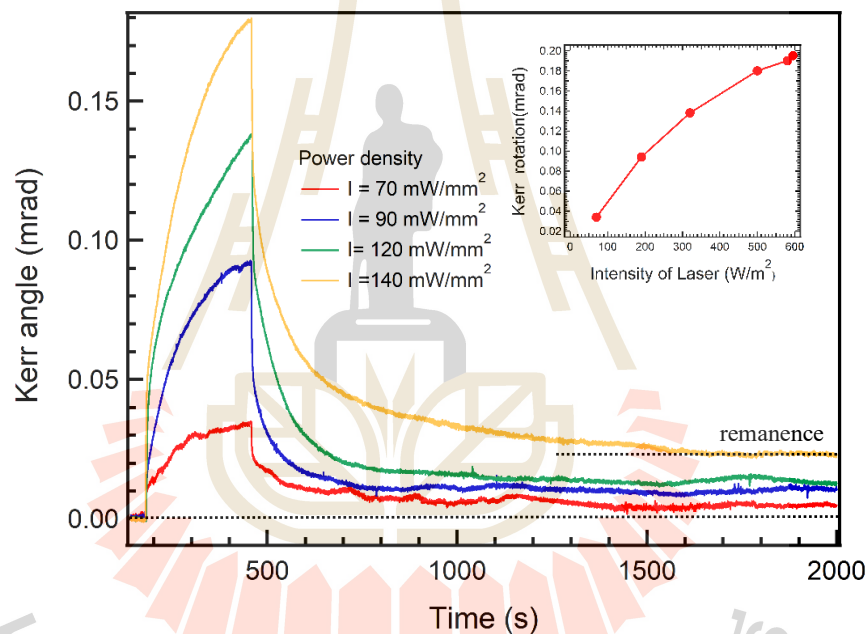


**Figure 4.14** The Kerr rotation behavior in terms of four different power density ( $\leq 140 \text{ mW/mm}^2$ ) in time resolve Kerr rotation of BFO which respond to the ultraviolet stimuli at different power density.

The experiment changing the laser power density was preformed to studies the behavior of Kerr rotation. We have studied the evolution of the photo-enhance of the BFO films as a function of incident light intensity. Figure 4.14 shows the evolution of Kerr rotation upon laser illumination with wavelength 405 nm, above light powers

density of  $\sim 70\text{mW/mm}^2$  to  $\sim 140\text{mW/mm}^2$  for 300 second. From the experiment results, it was found that the curves were changed with the intensity by modifying the UV intensity over equal intervals. And found that there was an outstanding remanence Kerr rotation after turning off the laser. The inset show relation between laser power density and Kerr rotation tends to saturate under power density of irradiation over  $600\text{mW/cm}^2$  which beyond the limit of our instrument.

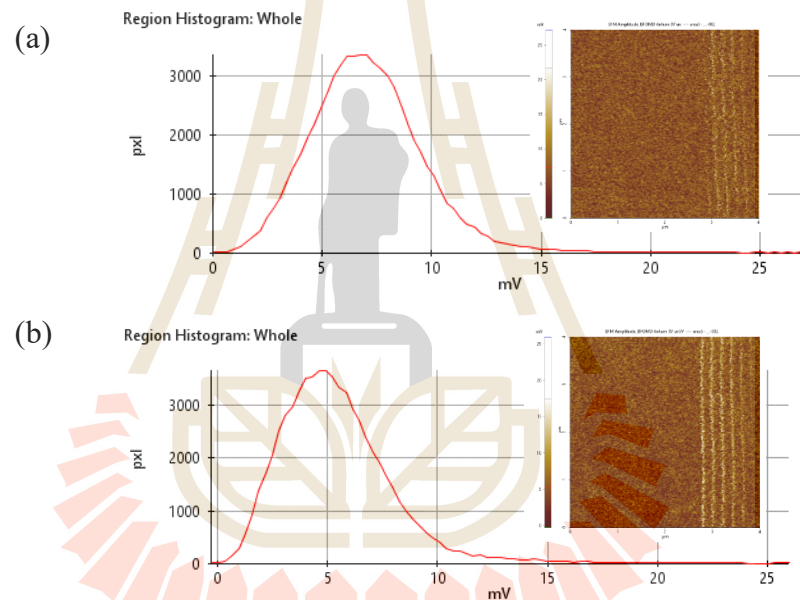


**Figure 4.15** PFM of BFO/SRO/STO under light and dark condition.

PFM image show out of plane polarization of BFO in the dark and light condition. Surface potential related to intrinsic polarization was measured, the result show that ferroelectric polarization of BFO was decrease after UV illumination. Namely, depolarization field caused by Bulk photovoltaic effect (BPV). Consistent with the research of Yang group (Yang et al., 2009) which propose that oxygen vacancies are able to move upward direction and accumulate near the top surface after

the applied electric field is turned off, this can result in ferroelectric depolarization screening in BFO.

#### 4.6 Relaxation of photo-induced Kerr rotation in BiFeO<sub>3</sub>

In this part of experiment, we report the investigation of the effect of light intensity on Kerr rotation variation in BFO/SRO/STO heterostructure. The continuous laser with the wavelength of 405 nm was used as the excitation light source in the experiment. Figure 4.16(a)-(b) show the time-resolved Kerr rotation with laser-on and off conditions upon uv illumination with 70 mW/mm<sup>2</sup> and 140 mW/mm<sup>2</sup> power density on for 300 second, respectively. As noted in figure 4.16(a), Kerr rotation raise immediately when laser is turning on, and then falls as soon as laser turning off and then gradually decrease to the initial level. Figure 4.16(c)-(g) show unpredictable variation of Kerr rotation upon UV illumination with power density between 250 to 500 mw/mm<sup>2</sup>. This phenomenon can be understood that the internal electric field separate the photon generated electron-hole pair and the electrons move to the surface, while holes move to the interface of BFO/SRO, and therefore suggest that Kerr rotation was induced. When the laser is turning off, the electron-hole pairs recombine, leading to the rapid fall of Kerr rotation and contribution to polarization to gradually fall of Kerr rotation.

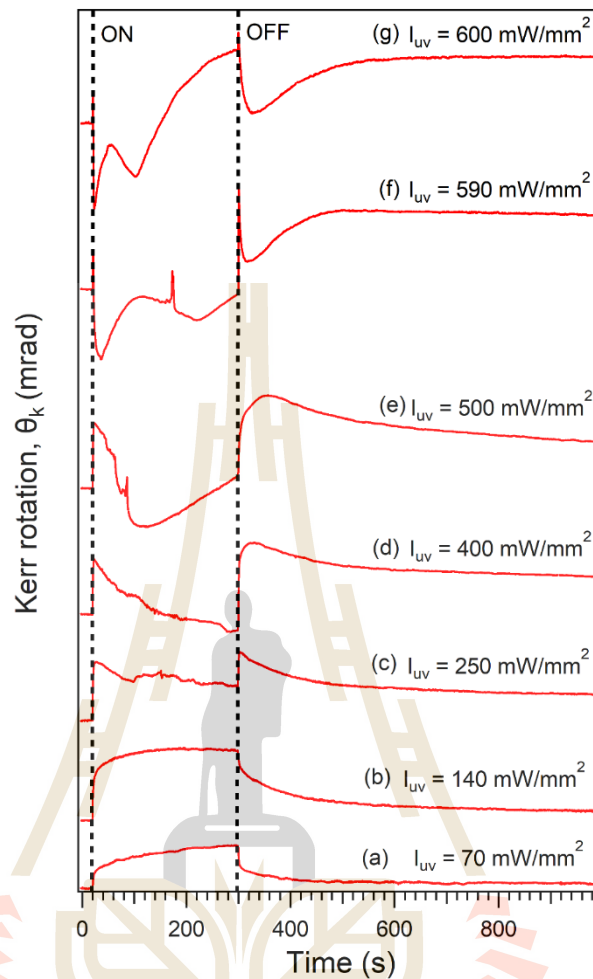


**Figure 4.16** (a)-(g) show time-resolved Kerr rotation upon uv illumination with 70 mW/mm<sup>2</sup> to 600 mW/mm<sup>2</sup> power density on for 300s.

In our discussion, UV illumination can disturb the magnitude of the spontaneous polarization in BFO which has a electronic interactions with light namely bulk photovoltaic (BPV) effect caused by non-centrosymmetric crystal structure. An anomalously large open-circuit voltage ( $V_{OC}$ ) exceeding the bandgap can be generated in BPV effect. Large open-circuit potential affects the optical properties of materials, e.g. refractive index, and also trigger polarization switching in ferroelectrics under illumination. For example, the largest electric field magnitude generated by the  $V_{OC}$  in

BFO thin films equal to  $\approx 5.5 \text{ kV cm}^{-1}$  that is smaller than coercive field of BFO.(Bhatnagar et al., 2013; Nakashima et al., 2016)

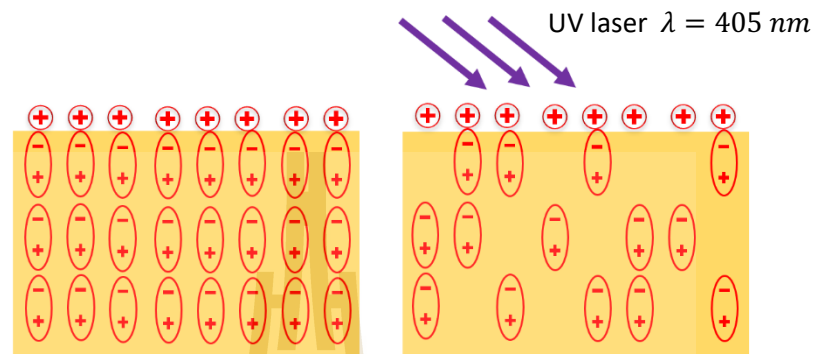


**Figure 4.17** Schematic diagram model of photo-induced depolarization in macroscopic perspective.

Figure 4.16 show the lifetime of UV induced Kerr rotation which is much longer than the photo-generated charges lifetime (approximately 100-200 ns)(Yamada et al., 2014). It could be possible scenario the photo-generated charges have completely recombined as soon as the laser was turned off. Therefore, the observed Kerr rotation enhancement is not likely to be caused by the photo-generated carriers but results from some other effect with a long lifetime. We suggest that such charges might be the bounded charges and the screening charges because screening charges are unavoidably accumulated on the surface of ferroelectrics to balance the polarization's bounded charges. In many cases, the amount of the screening charges are slightly more than the bound charges, or is called the overscreened non-equilibrium charges. The coulomb repulsion act on this charge make it diffuse away or desorb from the surface until system enter a screened equilibrium state. This diffusion or desorption of overscreened charges slowly occurs due to the polarization trapping effect. We suggest that illumination of UV laser have some long-period influence on the polarization and change the balance

between the surface-adsorbed screening charge and the bound charges. However, it might be the photo-induced depolarization that cause overscreening of surface-adsorbed charges, which can be maintained for hours after the illumination (figure 4.17).

Furthermore, according to the radiated graph with a laser power density of 70, 140, 250, 400, 500 mW/mm<sup>2</sup>, respectively, it can be seen that as soon as the light is turned off, the Kerr rotation decreases rapidly then reveal remanence Kerr rotation. In contrast, reveals a gradual increase in the gradual change when irradiated sample with  $\geq 250$  mW/cm<sup>2</sup>. Remanence Kerr rotation after turning off at 1000s delay time was plot versus power density of light show in figure 4.20 show linearly increases during light irradiation with power density 70-500 mW/mm<sup>2</sup>. That light has an end. Found that when adjusting, the light intensity increased gradually. If the light intensity is greater will result in a decrease in the curves. It is assumed that this is the result of leakage current. It has been reported that in the BFO, there is a leakage of charge, and it is reported that oxygen vacancy makes polarization much worse.

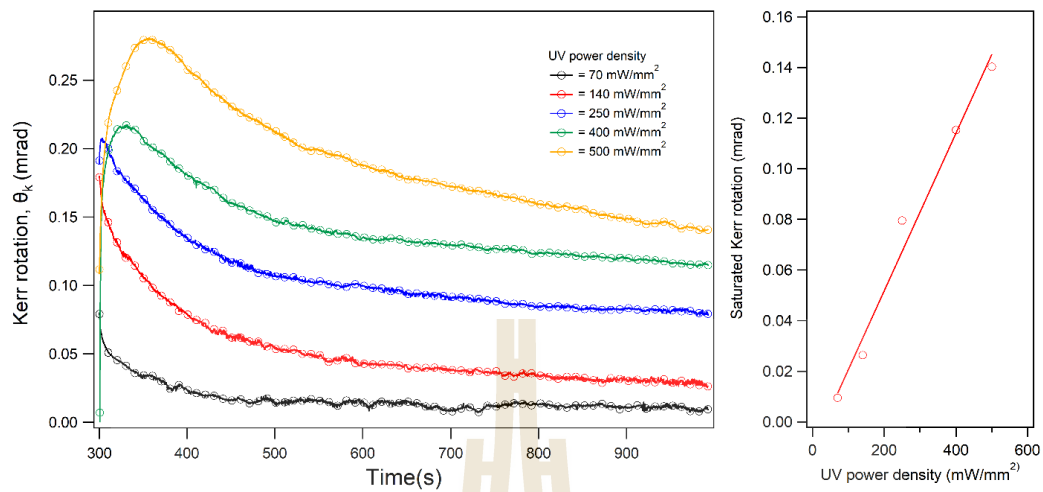


**Figure 4.18** Relaxation of Kerr rotation as a function of time (a), remanence Kerr rotation depending on laser power density (b).

#### 4.7 In-situ photoemission spectroscopy (PES)

To understand the mechanisms of the light-sensitive behavior in BFO/SRO/STO heterostructure, the BFO's electronic structure was measured by ultraviolet imaging (UPS) spectroscopy. The in-situ PES measurements were performed in ultra-high vacuum (UHV) upon laser illumination with power density 250 mW/mm<sup>2</sup> at room temperature.

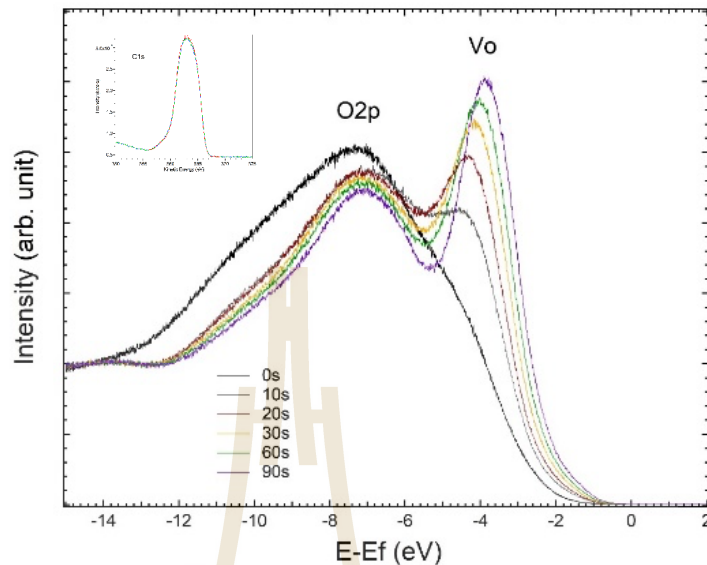


**Figure 4.19** The evolution of the valence band (VB) spectra of BFO mono-domain film measured from the initial surface to the exposed surface. The shifts in the binding energy of  $O_{2p}$  valence electrons state while the  $C_{1s}$  (inset) is located at the same energy.

Here, we discuss the corresponding changes in the oxygen valence band. Figure 4.19 shows angle-integrated photoemission (AIPES) valence band spectra for different exposures to UV laser ( $\lambda = 405 \text{ nm.}$ ). At  $t = 0$  (black line), the spectrum shows clear oxygen 2p ( $O_{2p}$ ) states mix with initial oxygen vacancy state between  $\sim 3\text{-}12 \text{ eV}$ . As the exposure time increase, the spectral weight of  $O_{2p}$  state decrease slightly and highest edge shifts to lower binding energy. Moreover, oxygen vacancy state edge significantly shifts to lower binding energy. This indicates an increase in valence band maximum to surface Fermi level. Together with the valence band shift we also observe a broad in-gap state developing at binding energy of  $\sim 2 \text{ eV}$ . We consider that this state is likely associated with double-oxygen-vacancy at the surface. Corresponding to the literature

report that double-oxygen-vacancies cluster in solid can induce deep in-gap states located at 1.5~2.0 eV below the CBM (Li and Wei, 2021).

The as-prepared BFO sample was measured (e.g., 0-minute irradiation, black spectrum in Figure 4.19). UPS spectrum show the  $O_{2p}$  state with a binding energy of approximately 6-8 eV was in close position compared to other metal oxides imply that good electrical contact between the sample and the holder. The  $O_{2p}$  state suddenly shift to lower binding energy in first doping condition (10 second of UV exposure) as illuminated by brown spectrum in figure 4.19. The UPS spectrum of 90s condition clearly show a significant shift of 0.4eV to lower binding energy (the purple spectrum in Figure 4.19). Moreover, an inter-gap peak appear at around 4eV and 2eV can be indicated to be the oxygen vacancy state ( $V_0$ )(King et al., 2012; Masingboon et al., 2013) and double oxygen vacancy state( $V_{0++}$ ). Furthermore, after UV illumination ( $h\nu=3.06$  eV), the  $C_{1s}$  state was also measured. The result show no binding energy shift of  $C_{1s}$  state (inset in figure4.19) confirming the peculiar character of BFO. We did the standard Gaussian fitting and extract the continuous shift of  $O_{2p}$  state as a function of UV exposure time. We found that shifting reach the value as high as 243 meV at a maximum UV irradiation time as summarized in figure 4.20

Anomalous shifts appear in the region of the valence band toward lower binding energy with increasing electron doping via illumination time which suggests a direct effect of negative electronic compression (NEC). Possible that the coupling between Kerr rotation and BFO can occur together with NEC effect. Moreover, we can meet a small peak of double ionized oxygen vacancy state when we shine the light for long time.

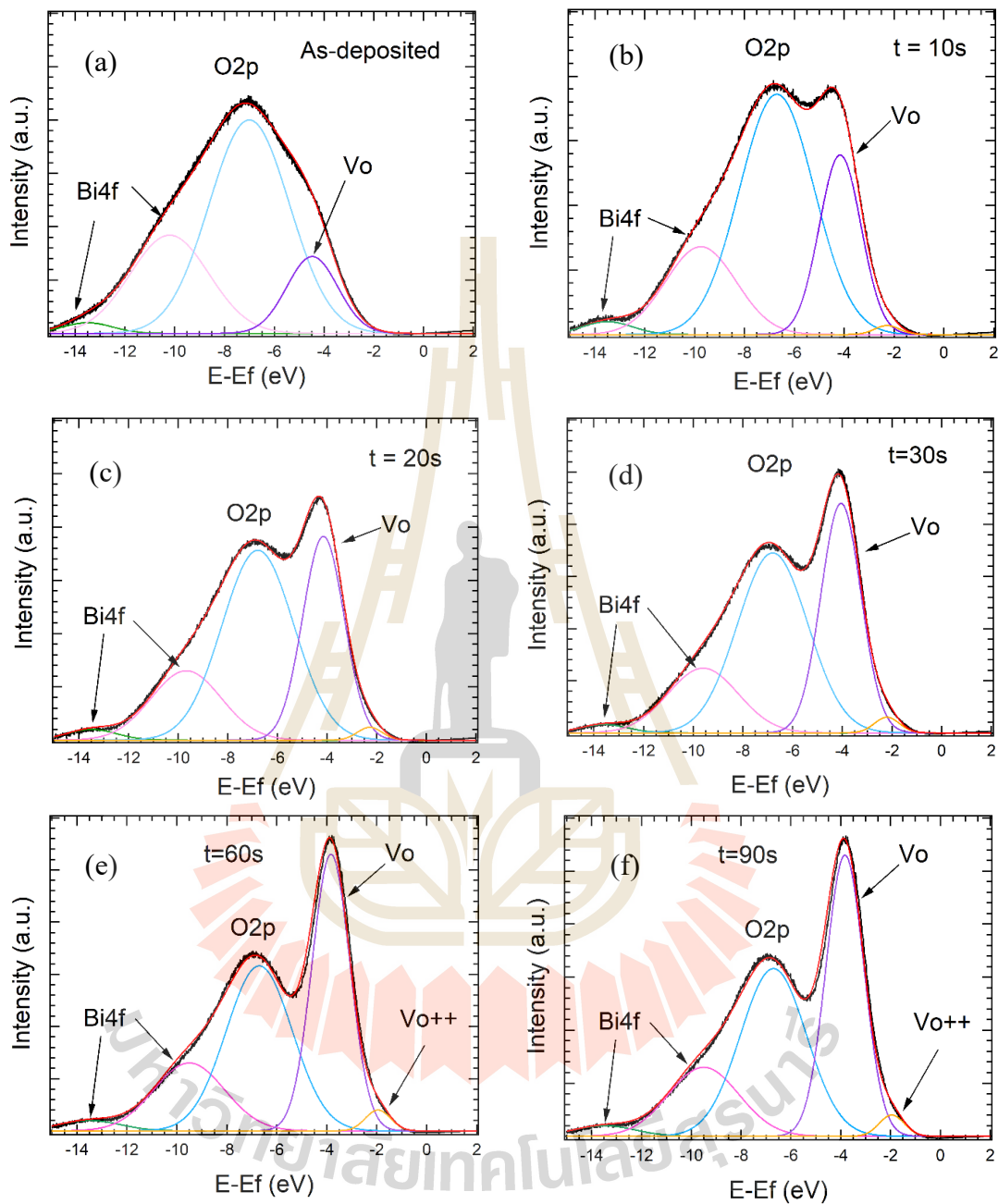
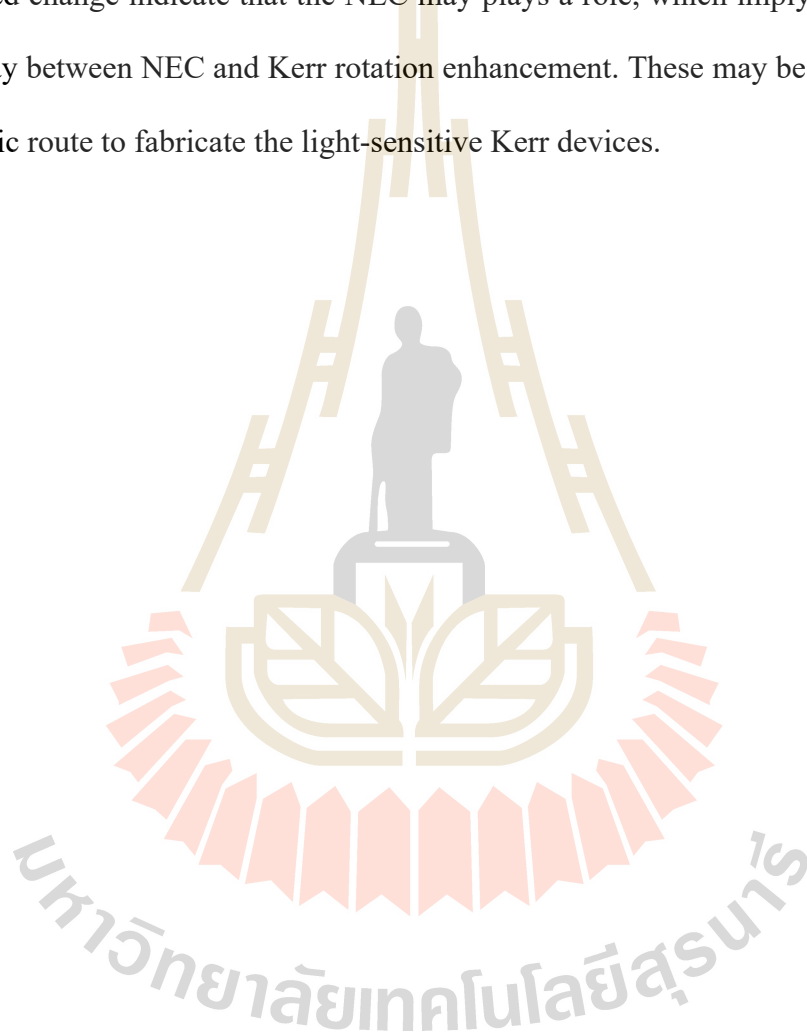


**Figure 4.20** XPS spectra for valence band of the BFO and the Gaussian fitting, upon laser irradiation time is a) 0s, b) 10s, c) 20s, d) 30s, e) 60s, and f) 90s, respectively.

It has been report that the creation of oxygen vacancy states induced by light irradiation can control carrier densities on metal oxide surface (Meevasana et al., 2011). Ultraviolet photoemission spectroscopy (UPS) reveal a signature of negative electronic compressibility (NEC) of BFO (figure 4.19) upon light illumination, the experimentally observed change indicate that the NEC may plays a role, which imply that there is an interplay between NEC and Kerr rotation enhancement. These may be begun of a new synthetic route to fabricate the light-sensitive Kerr devices.



# **CHAPTER V**

## **THE STUDY OF PHOTO-ENHANCED MAGNETISM IN**

### **NI/Bi<sub>2</sub>TE<sub>3</sub>**

This chapter's contents report the study of ferromagnetic properties of Ni/Bi<sub>2</sub>Te<sub>3</sub> thin films, which were induced by laser with wavelength 405 nm. It all started with the preparation of nickel film on Bi<sub>2</sub>Te<sub>3</sub> by the chemical electroless deposition technique. The experimental results on the study of photo-enhanced magnetism in Ni/Bi<sub>2</sub>Te<sub>3</sub> are only reported in this chapter. The content in this chapter is divided into three sections: the first section describes the preparation of the Ni/Bi<sub>2</sub>Te<sub>3</sub> sample. The second section reports the results of the samples characterization was done by various techniques to understand morphology, chemical composition, and microstructure using a scanning electron microscope (FESEM), energy dispersive X-ray (EDX). In the third section, in-situ MOKE was set up and operated under dark and light laser irradiation. This section presents a concept providing a significant enhancement in coercivity upon laser illumination, and the results of the electronic structure during laser irradiation were measured by in-situ X-ray absorption near edge structure (XANES) and X-ray photoemission spectroscopy (XPS).

## 5.1 Electroless deposition of nickel

Figure 5.1 shows the cyclic voltammogram (CV) of  $\text{Bi}_2\text{Te}_3$  in a pure electrolyte solution of  $\text{HCl}(\text{pH}=3) + 20 \text{ mM NaCl}$  (black curve) and in the electrolyte solution containing  $40 \text{ mM NiCl}_2$  (red curves) taken with a scan rate  $30 \text{ mV s}^{-1}$ . In the pure electrolyte, the potential range at the anodic limit of CV measurements show bismuth dissolution reaction (BDR) at  $0.15 \text{ V}$  followed by the appearance of a pronounced cathodic peak around  $-0.15 \text{ V}$  in the reverse potential scan. This cathodic peak indicates the redeposition of the dissolved  $\text{Bi}_2\text{Te}_3$ , which can be negligent. An exponential growth of the cathodic current appears at  $E_{\text{work}} = -0.65 \text{ V}$  showing a hydrogen evolution (HER). Because of we used a Pt counter electrode (Pham et al., 2007; Tsay et al., 2010). The small amount of Pt dissolved from the counter electrode may deposit at the working electrode, cause a farther inception of hydrogen evolution. After adding  $40 \text{ mM NiCl}_2$  and setting the range of CV measurements at  $-0.2 \text{ V}$  to  $-1.0 \text{ V}$ , the shape of the CV (curve b) looks similarly to curve a. the BDR starts at  $0.16 \text{ V}$  and the HER starts farther at around  $-0.96 \text{ V}$ . For the turning point at  $-0.7 \text{ V}$  (curve d), the strip-off CV curve indicate no significant Ni deposition. Further CV measurements (curves e–g) show that the P1 broad peak grows after extending the cathodic potential, indicate that P1 is a result of the dissolution of Ni.

CV result show cathodic current at  $\sim -0.55 \text{ V}$  vs  $\text{Ag/AgCl}$  and a broad peak (C1) at  $\sim -0.8$  to  $-0.9 \text{ V}$  vs  $\text{Ag/AgCl}$  related to Ni nucleation and reduction. The  $\text{Ni}^{2+}$  reduction potential was shift due to a nucleation barrier (Ivanova et al., 2007). The current increases extremely when the scan go to more negative potentials ( $> -0.9 \text{ V}$  vs  $\text{Ag/AgCl}$ ), corresponding to nickel deposition and simultaneously  $\text{H}_2$  gas evolution.

We can see the formation of H<sub>2</sub> gas bubbles at the edges of the sample on the WE beyond  $-1.0$  V vs Ag/AgCl. It has been reported that adsorbed hydrogen molecules caused Ni-hydrogen alloys which deter the growth of nickel film. (Cui and Lee, 1995; Fleischmann and Saraby-Reintjes, 1984; Singh et al., 1990). To avoid Ni-hydrogen alloy formation and prevent the film's surface from being destroyed by H<sub>2</sub> evolution, in sample preparation, it defines potential in electroless deposition must not higher than  $-0.9$  V. In this experiment section, performed the electroless deposition of nickel with chronoamperometry mode at  $V_{\text{bias}} = -0.86$  V, and current of deposition was shown in figure 5.2

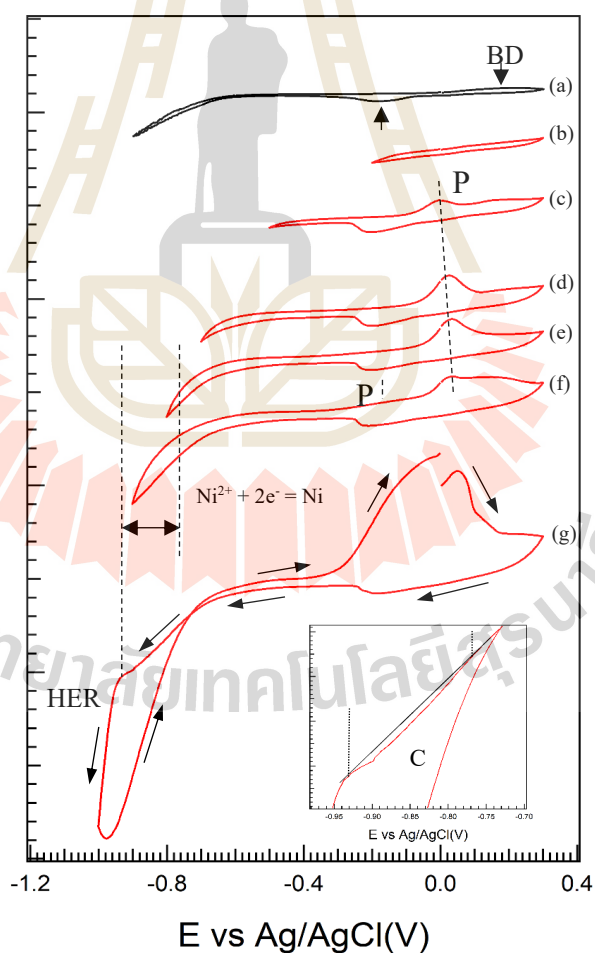


**Figure 5.1** Cyclic voltammogram of Bi<sub>2</sub>Te<sub>3</sub> in 1 mM HCl (curve 1) and 1mM HCl/1 mM NiCl<sub>2</sub> (curve b to g) solutions,  $dE/dt = 30 \text{ mV s}^{-1}$ .

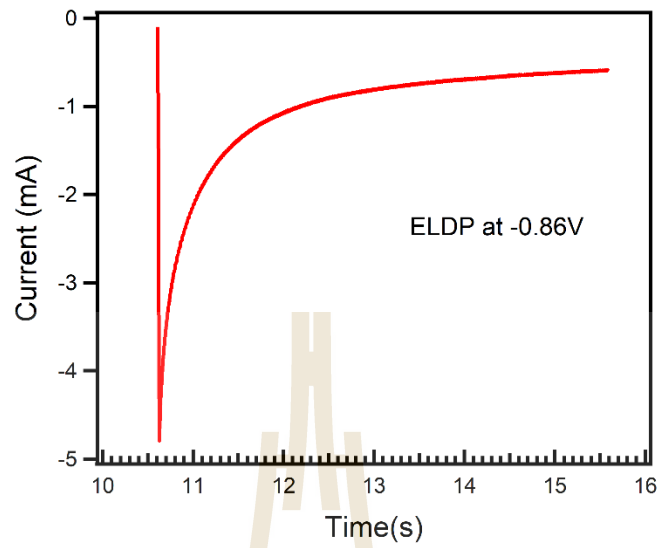


**Figure 5.2** Chronoamperometry of Ni electroless deposition on  $\text{Bi}_2\text{Te}_3$  at  $V_{\text{bias}} = -0.86\text{V}$ .

## 5.2 Morphology characterization

The morphology of the Ni film on  $\text{Bi}_2\text{Te}_3$  substrate was characterized by scanning electron microscope (SEM) as shown in Figure 5.3. The Ni film with the deposition time equal 5s to 300s were deposited to estimate the growth rate of films.

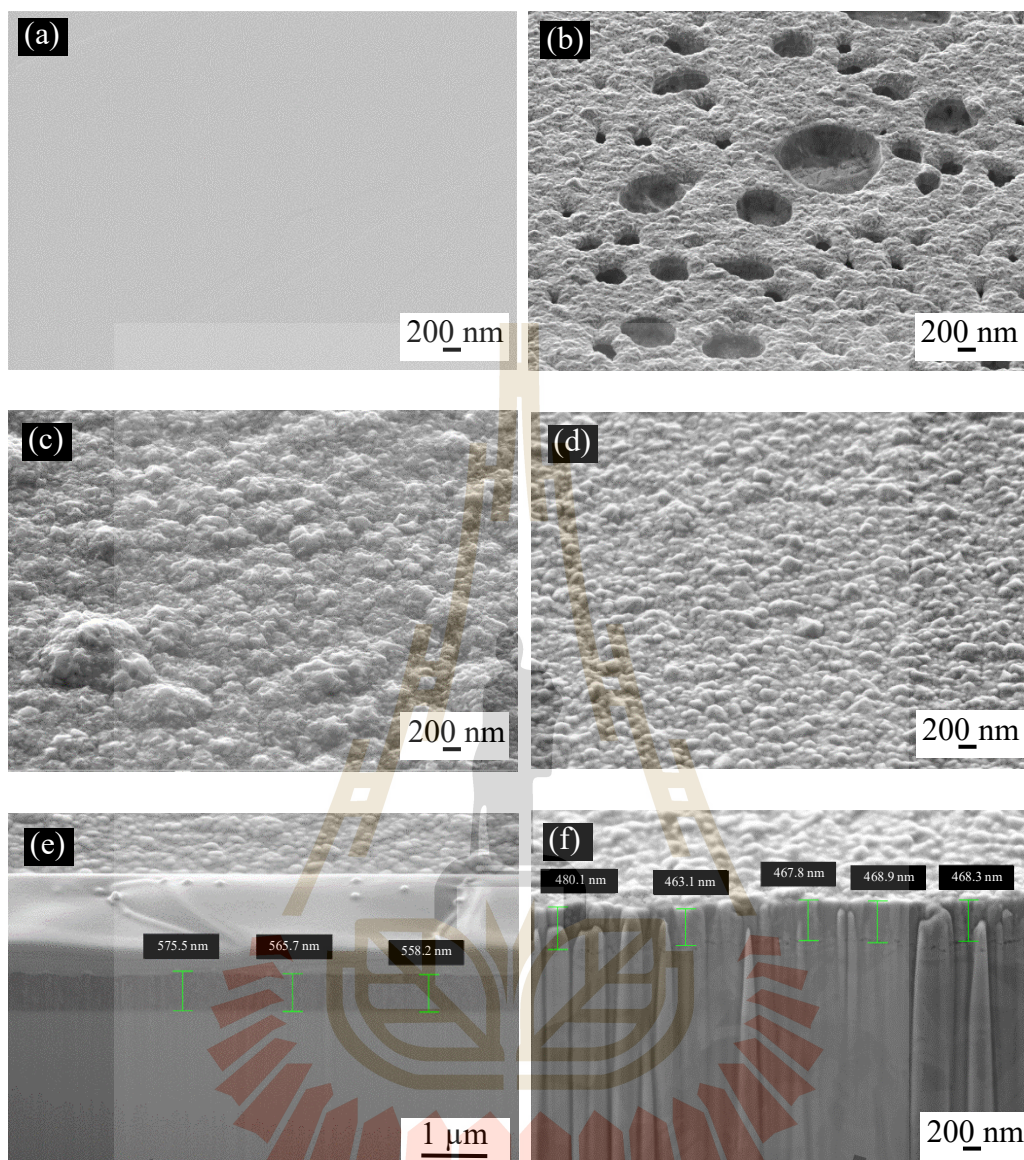
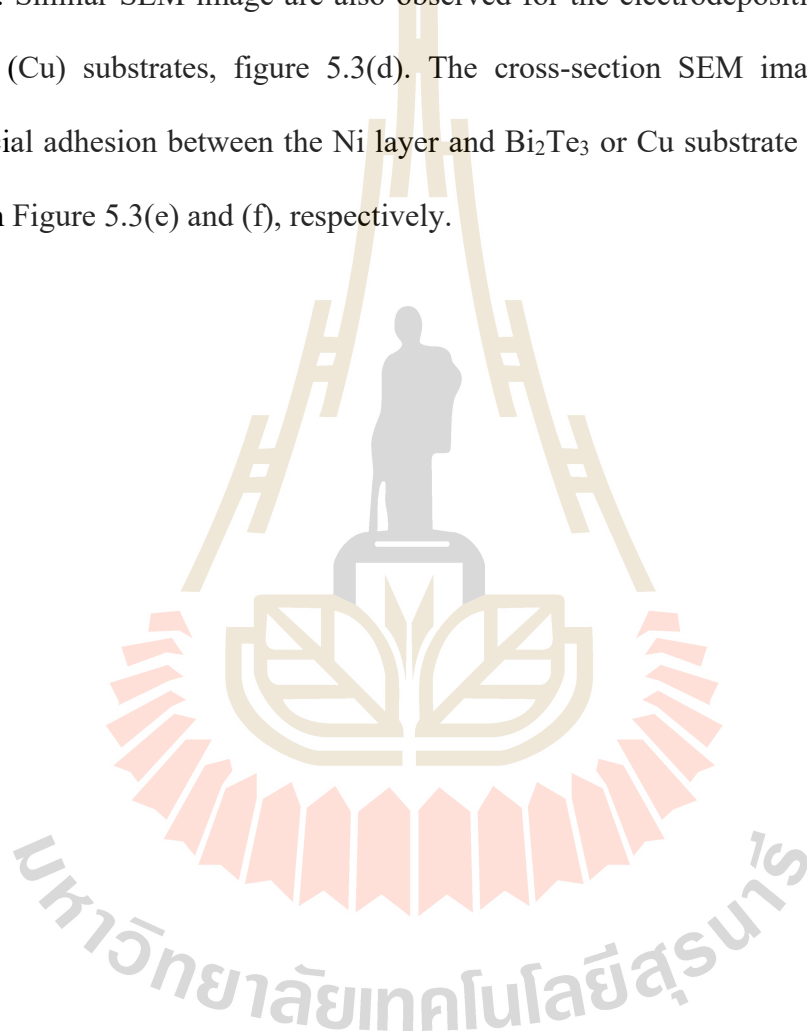


**Figure 5.3** SEM micrographs of surface morphologies of (a)  $\text{Bi}_2\text{Te}_3$  substrate before Ni electrodeposition, (b)-(c)  $\text{Ni}/\text{Bi}_2\text{Te}_3$  after Ni electrodeposition for 60s and 300s, (d)  $\text{Ni}/\text{Cu}$  after electrodeposition for 60s, and (e) Cross-sectional SEM micrographs of electroplated Ni layers with 300s deposition time on (e)  $\text{Bi}_2\text{Te}_3$ , and (f) Cu substrate.

As we know that surface roughening of the  $\text{Bi}_2\text{Te}_3$  surface is a parameter affected to adhesion between an Ni layer and  $\text{Bi}_2\text{Te}_3$  substrate. Therefore, it was set to

be done regularly to peeling off  $\text{Bi}_2\text{Te}_3$  to get virgin surface, as shown in figure 5.3(a), SEM image show the surface morphology of the cleaved  $\text{Bi}_2\text{Te}_3$  substrates is very smooth after peeling. After electrodeposition of Ni, the  $\text{Bi}_2\text{Te}_3$  surfaces are covered with a uniform Ni layer with a fine-grained nanostructure, as shown in figure 5.3(b) and (c). Similar SEM image are also observed for the electrodeposition of Ni on the copper (Cu) substrates, figure 5.3(d). The cross-section SEM image indicate the interfacial adhesion between the Ni layer and  $\text{Bi}_2\text{Te}_3$  or Cu substrate looks strong, as show in Figure 5.3(e) and (f), respectively.



### 5.3 Chemical composition analysis by EDX

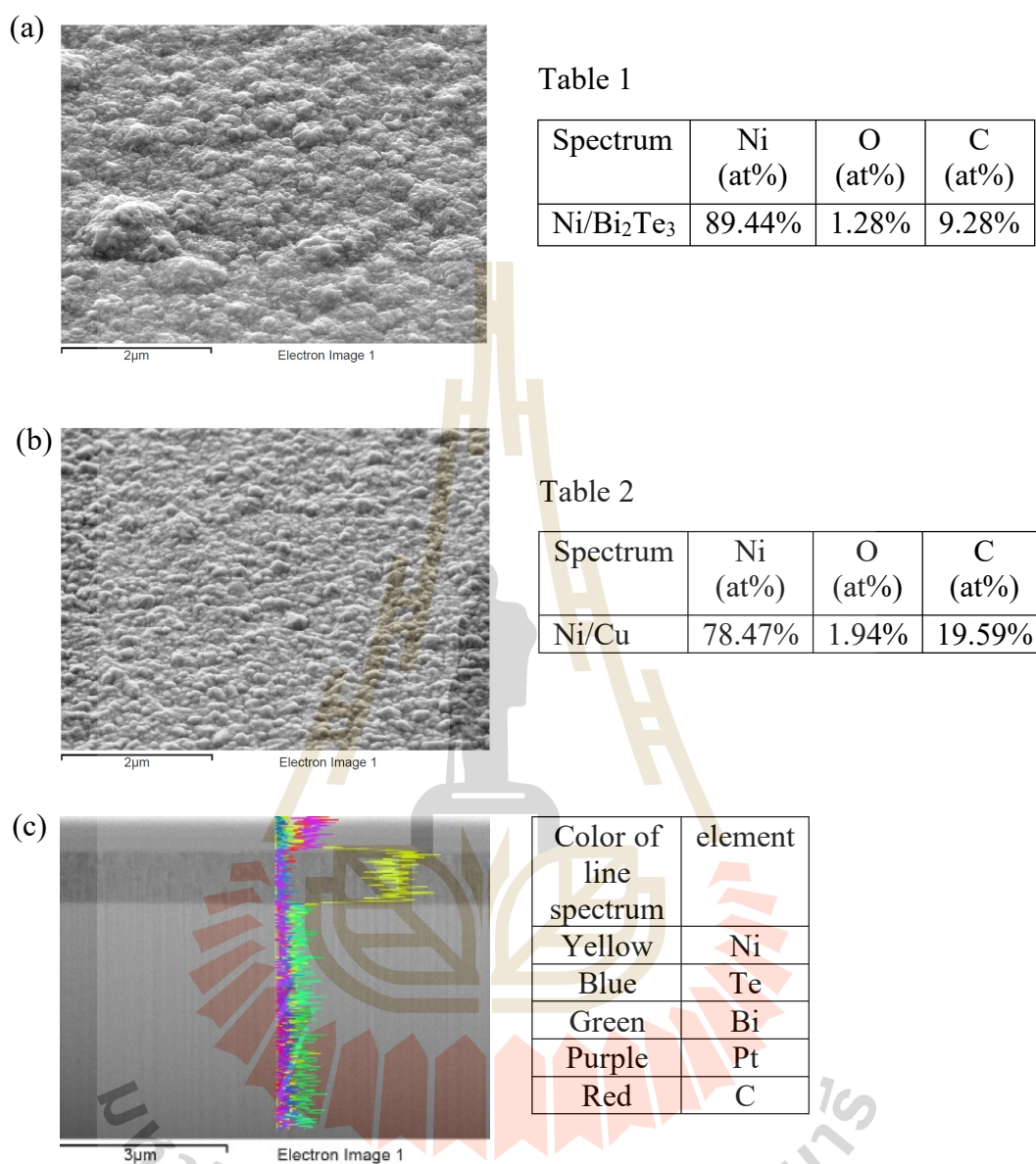


**Figure 5.4** EDS analysis. Quantitative chemical composition analysis of as-prepared Ni/Bi<sub>2</sub>Te<sub>3</sub> and Ni/Cu as shown in the SEM image. (a) The SEM image of as-prepared Ni/Bi<sub>2</sub>Te<sub>3</sub> sample. (b) The SEM image of Ni/Cu sample. (c) The cross-section SEM image of Ni/Bi<sub>2</sub>Te<sub>3</sub> sample. Table 1 EDS data recorded on the Ni/Bi<sub>2</sub>Te<sub>3</sub> sample. Table 2 EDS data recorded on the Ni/Cu sample.

The results obtained from the EDX analysis of each structure shown in SEM images are tabulated in the Table (Table 1 and Table 2) on the right-hand side of the SEM image. The Ni/O ratios of the Ni/Bi<sub>2</sub>Te<sub>3</sub> sample are approximately 70/1, ascribed to the Ni metal film. In the Ni/Cu sample, the Ni/O ratios are approximately 40/1, which cannot be identified as the oxidation of nickel (Ni) to the nickel oxide (NiO) formation. Therefore, these results confirmed that the Ni metal was formed on a Bi<sub>2</sub>Te<sub>3</sub> and Cu substrate and we consider the oxygen as the contamination.

## 5.4 Magneto-optical Kerr effect measurement (MOKE) of Ni/Bi<sub>2</sub>Te<sub>3</sub>

### 5.4.1 Light-induced changes in coercivity

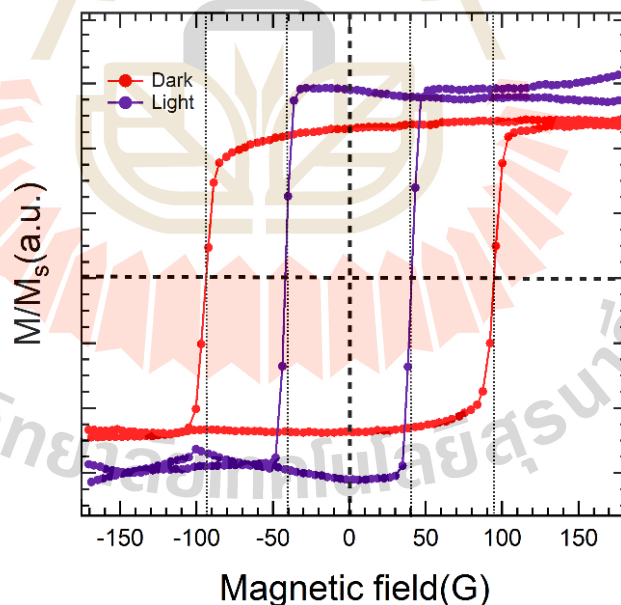


**Figure 5.5** Magnetization versus applied magnetic fields as measured in the dark and light states of Ni/Bi<sub>2</sub>Te<sub>3</sub> with deposition time 60s.

The narrowing modifies the M-H hysteresis loop of the Ni film (figure 5.5), as revealed by the longitudinal magneto-optic Kerr effect (MOKE) magnetometer. The shape of the initial M(H) loop is modified after light exposure, with a change in coercivity of 57.89%, which remains stable over a long period. MOKE hysteresis loop measurements were performed at room temperature before and after excitation. This result show here, report the ferromagnetic hysteresis loop of heterostructure of Ni/Bi<sub>2</sub>Te<sub>3</sub> which deposition time equal to 60s. After chemical preparation, magnetic characterization was performed immediately by MOKE magnetometer. Changes in coercivity with respect to light were observed, the coercivity of Ni/Bi<sub>2</sub>Te<sub>3</sub> in dark state equal to 95G, and when the sample was irradiated with 405 nm ultraviolet laser in the light state, the coercivity is 40G. Moreover, saturate magnetization increased. The magnetic behavior was evaluated via measurements of the hysteresis loop obtained by MOKE at room temperature. A substantial decrease in coercivity was obtained for the light exposed sample ( $H_c = 40 \pm 5G$ ) compared with the non-exposed sample ( $H_c = 95 \pm 5G$ ). To understand the microscopic mechanism that induce light-sensitive behavior of Ni/Bi<sub>2</sub>Te<sub>3</sub>, Magneto-Optical Kerr rotation show the longitudinal magneto-optical Kerr effect (L-MOKE) hysteresis loops of the prepared sample upon UV illumination. It is evidently verified that a narrowed Kerr hysteresis loop is observed by increasing the power density of laser to 500 mW/mm<sup>2</sup>. Similarly, the saturation magnetization was enhanced simultaneously. It has been clarified that this effect is contribution of substrate to compare, not present of light-sensitive behavior on Ni/Cu sample.

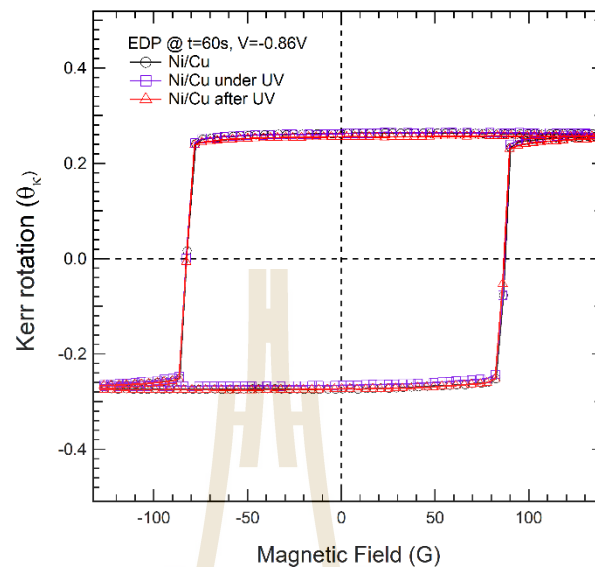


**Figure 5.6** Magnetization versus applied magnetic fields as measured in the dark and light states of Ni/Cu with deposition time 60s.

## 5.5 Ultraviolet photoemission spectroscopy (UPS) analysis of Ni/Bi<sub>2</sub>Te<sub>3</sub>

UPS was used to understand the intrinsic mechanism that drive the light-sensitive behavior at the surface of Ni/Bi<sub>2</sub>Te<sub>3</sub>. Because of the deposition time effect to the thickness and porosity of film, we selected the sample with 60s deposition time to investigate the mechanism behind the interface between Ni film and Bi<sub>2</sub>Te<sub>3</sub> substrate., The Bi5d and Te4d spectra were recorded at 90 eV photon energy to get the elite surface sensitivity and spectral resolution. The XPS spectra of Bi5d, Te4d, O1s core levels with as-prepare (dark) and light condition were recorded to investigate the chemical bonding states. Consider the case of Bi spectrum shown in the Figure 5.7(a), the main Bi5d peak has the spin-orbit splitting and split into a 5d<sub>5/2</sub> and 5d<sub>3/2</sub> doublet located at 24.85 eV and 27.95 eV agreement with the literature data (Yashina et al., 2013). Another doublet

peak of Bi is shifted towards higher BE values, indicating that the oxidation state of Bi<sup>-</sup> occur while preparing sample. The spectra show a reliable separated spin-orbit component of around 11.5 eV which is typical of the presence of Bi<sup>2+</sup>. We suggest that there is the mechanism of oxidation in aqueous solution as well as in liquid water in preparation process, the surface product formed at the beginning of the preparing process including an oxidized tellurium with a chemical shift of +1.3eV (corresponding to Te<sup>2+</sup>) (figure 5.7(b)) and a reduced Bi atoms with a chemical shift of -1.0 eV (corresponding to Bi<sup>+2</sup>) in oxidation of bismuth to bismuth oxide. Besides, all peaks are shifted towards lower BE values (0.1 eV) in the light condition, we suggest that electrical conductivity was small modify on the surface of the exposed sample. Figure 5.7(c) show O1s peak, which implies that oxygen contaminating on the surface decrease, after sample was exposed to laser irradiation. moreover, the result (figure 5.7(d)) show that Ni3p peak not change with respect to light illumination.

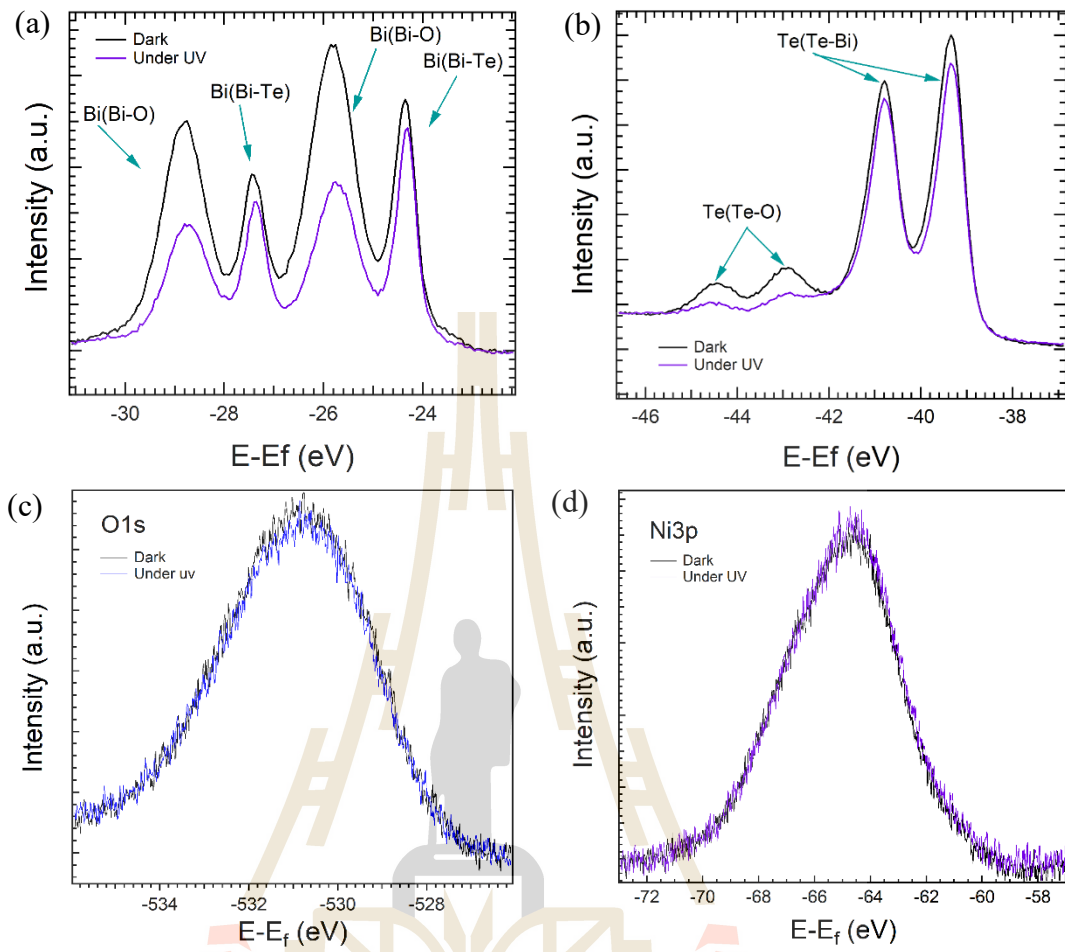


**Figure 5.7** UPS spectra of Ni/Bi<sub>2</sub>Te<sub>3</sub> sample. (a), (b), (c) and (d) Bi5d, Te4d, O1s and Ni3p spectra, respectively.

มหาวิทยาลัยเทคโนโลยีสุรนารี

## 5.6 X-ray Absorption Spectroscopy (XAS)

Schematic representation of *in situ* soft X-ray experimental setup at room temperature and ambient condition shown in figure 5.8(a) and photograph of the built-in UV laser setup is presented in figure 5.8(b). The X-rays impact the sample at an angle of  $45^\circ$ . The FY detectors were placed  $90^\circ$  out of the incoming X-rays. The XANES measurement was performed in fluorescence mode for Ni K-edge.

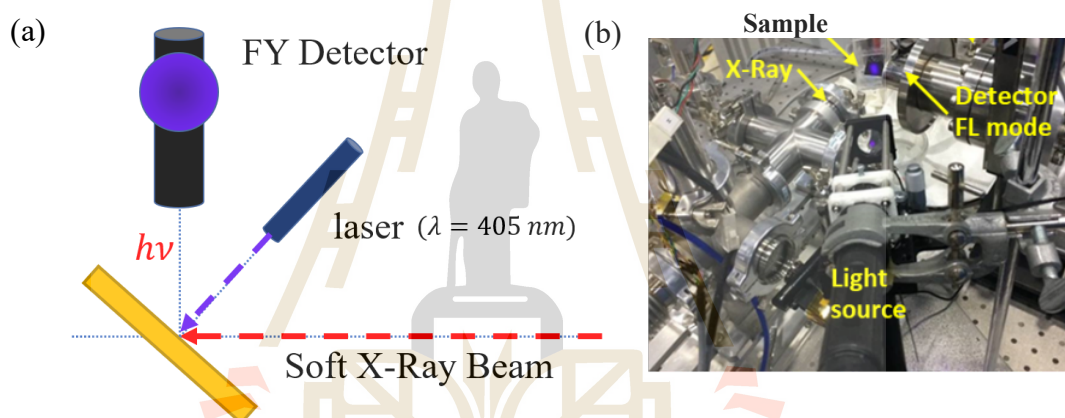


**Figure 5.8** In situ Ni L-edge fluorescence measurement setup (a) schematic and, (b) the photograph of measurement system setup.

The oxidation states in the Ni/Bi<sub>2</sub>Te<sub>3</sub> were tracked using *in-situ* X-ray Absorption Spectroscopy (XAS) in the presence and absence of UV laser irradiation. Figure 5.9 shows the resulting normalized Ni K-edge XANES spectra imply no sign of the edge positions changes. The position of the absorption edge contains information on the electronic structure of Ni film on Bi<sub>2</sub>Te<sub>3</sub> substrate. During the exposure of laser, XANES spectra showed constant position edge, indicates the Ni oxidation state no change.

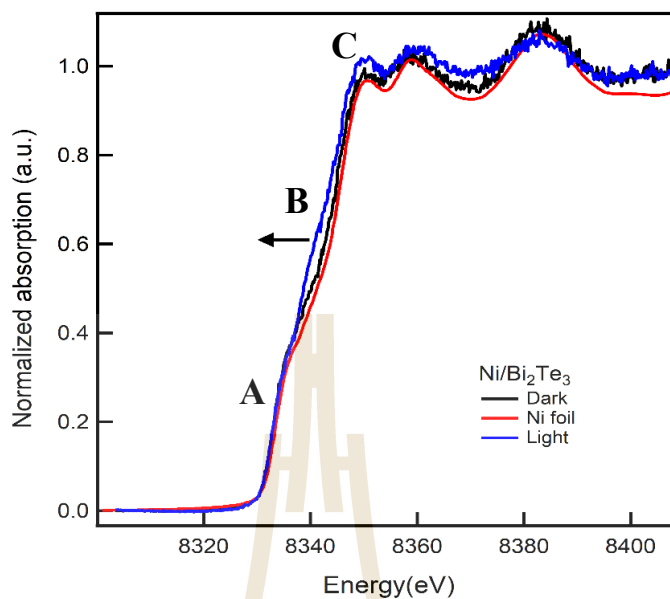


**Figure 5.9** In situ Ni K-edge fluorescence XANES spectra under dark and light illuminations.

Moreover, we reported the observation of three significant characteristics in the XANES results of Ni/Bi<sub>2</sub>Te<sub>3</sub> consist of the pre-edge feature at ~8333 eV (peak A) corresponds to an transition of electron to empty e<sub>g</sub> states, the second characteristic was observed at ~8339 eV (peak B), which indicate a transition to the Ni 4sp band, and the third characteristic is at ~8349 eV (peak c) indicate a p-like symmetry state, which is typically sensitive to Ni d-orbital mixing with Te 4p bands (Chang et al., 2018; Huggins et al., 2011; Kisiel et al., 1999).

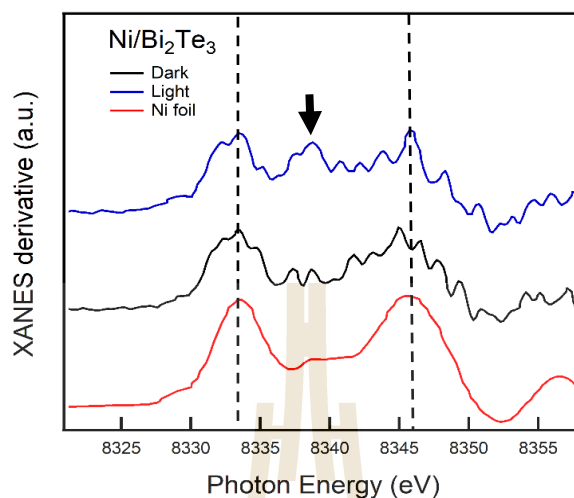


**Figure 5.10** Differentiation of Ni K-edge XANES for pure Ni foil(black), Ni/Bi<sub>2</sub>Te<sub>3</sub> sample under UV laser illumination.

The result in figure 5.10, although there is much noise, but we present the analysis of derivation XANES enough to hint at the change. The reference paper (Chang et al., 2018) states that a Ni-dichalcogenide bond, therefore we implied that after being stimulated by light with a wavelength of 405 nm, Ni:Te, was formed in sample. The characteristic feature of graph is attributed to the 1s to 4p transition, which arise from chalcogen-based charge-transfer. In our work, we implied that our results indicate the presence of strong Ni-Te covalent bonds after exposed to laser. The result implied that Bi<sub>2</sub>Te<sub>3</sub> which has a van der waal gap (~0.19 nm) between each QL (Wu et al., 2019) can contain the intercalated Ni atom, or Ni atom occupy the interstitial sites within QL. Because of Ni atom has an elemental radius (125 pm) smaller than the van der Waals gap, therefore it can move to occupy interstitial sites (Chang et al., 2018). Moreover, it was found that our result corresponds to literature result that a general electrochemical intercalation method can control concentration of zerovalent copper atoms into layered

$\text{Bi}_2\text{Se}_3$ , up to 57% copper atoms ( $\text{Cu}_{6.7}\text{Bi}_2\text{Se}_3$ ) with no destruction of the  $\text{Bi}_2\text{Se}_3$  lattice (Zhang et al., 2017). And copper (Cu) which has elemental radius (140 pm) can intercalate into Bismuth telluride, Cu (Bludská et al., 2004; Shetty et al., 2020).

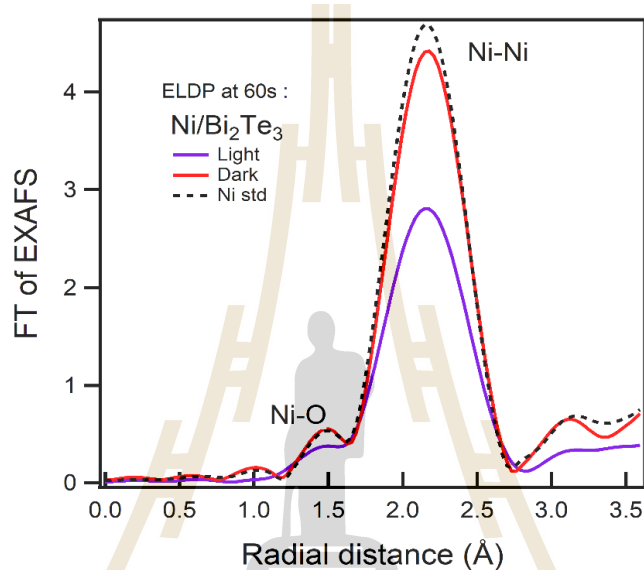


**Figure 5.11** FT EXAFS structures of  $\text{Ni}/\text{Bi}_2\text{Te}_3$  electroless deposition at 60s under dark and light illumination.

This graph reports the results of EXAFS at Ni L-edge. The peak arises from the nearest Ni-Ni coordination show Ni-Ni far away from the primary nickel atom at a distance of 2.1 Å. as-prepared  $\text{Ni}/\text{Bi}_2\text{Te}_3$  is at the same as the Ni foil. Later, the intensity of peak decreases when exposed to UV laser.

## CHAPTER VI

### CONCLUSION

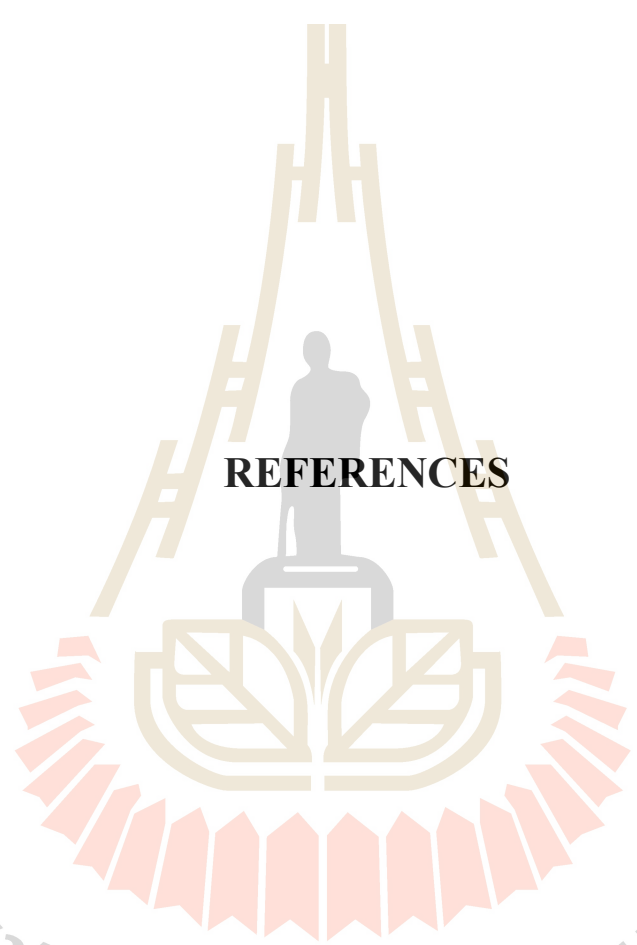
#### 6.1 Conclusion of the study of Bismuth Ferrite (BiFeO<sub>3</sub>) films

In this work, the motivation behind the project was to set up a Longitudinal Magneto-optical Kerr effect (L-MOKE) measurement system for characterizing BiFeO<sub>3</sub> films and studied the effect of laser enhance Kerr rotation. We have successfully installed the MOKE system and succeed to investigated the connection between Kerr effects and laser and magnetic field in BiFeO<sub>3</sub>/SrRuO<sub>3</sub>/SrTiO<sub>3</sub> heterostructure sample. Kerr rotation of BiFeO<sub>3</sub> can be carried out repeatedly through switching the applied laser and external magnetic field. Therefore, we have successfully utilized vertical shift of Kerr rotation to construct the state of Kerr rotation. Our proposed procedure to build in Kerr state internal optical properties inside BiFeO<sub>3</sub> and measure by Kerr rotation measurement. Based on the experimental results, we investigated the origin of laser-induced Kerr rotation, evidence to internal electric field due to oxygen vacancy distribution and ferroelectric polarization in BiFeO<sub>3</sub> are the key contribution to effect Kerr rotation of reflected laser.

## 6.2 Conclusion of the study of photo-enhanced magnetism in Ni/Bi<sub>2</sub>Te<sub>3</sub>

This part of thesis is to report the results of light response study of 405nm of a nickel film on bismuth telluride (Ni/Bi<sub>2</sub>Te<sub>3</sub>) prepared by an electroless chemical deposition method. The magnetic hysteresis loop was studied due to the relationship between the external magnetic field and the Kerr angle of rotation, which is proportional to the magnetism of the substance. The results showed that the light irradiation increased the saturation magnetization ( $M_s$ ) value. Moreover, the coercivity ( $H_c$ ) is significantly decreased. The results from XANES study of Ni charge state implied that while the laser beam irradiated to Ni/Bi<sub>2</sub>Te<sub>3</sub> sample, It could be possible an electron movement between the nickel and the tellurium and form a weak bond (Ni:Te) which affects the ferromagnetic interaction.





**REFERENCES**

มหาวิทยาลัยเทคโนโลยีสุรนารี

## REFERENCES

- Alexe, M. and Hesse, D. (2011). Tip-enhanced photovoltaic effects in bismuth ferrite. **Nature Communications**, 2(1): 256.
- Baek, S.H., Jang, H.W., Flokman, C.M., Li, Y.L. Winchester, B., Zhang, J. X., He, Q., Chu, Y. H., Nelson, C. T., Rzchowski, M. S., Pan, X. Q., Chen, L. Q., and Eom, C. B. (2010). Ferroelastic switching for nanoscale non-volatile magnetoelectric devices. **Nature Materials**, 9(4): 309-314.
- Banerjee, S., Mandal, M., Gayathri, N. and Sardar, M. (2007). Enhancement of ferromagnetism upon thermal annealing in pure ZnO. **Applied Physics Letters**, 91(18): 182501.
- Basharat, F., Rana, U.A., Shahid, M. and Serwar, M. (2015). Heat treatment of electrodeposited NiO films for improved catalytic water oxidation. **RSC Advances**, 5(105): 86713-86722.
- Bhatnagar, A., Roy Chaudhuri, A., Heon Kim, Y., Hesse, D. and Alexe, M. (2013). Role of domain walls in the abnormal photovoltaic effect in BiFeO<sub>3</sub>. **Nature Communications**, 4(1): 2835.
- Bludská, J., Karamazov, S., Navrátil, J., Jakubec, I. and Horák, J. (2004). Copper intercalation into Bi<sub>2</sub>Te<sub>3</sub> single crystals. **Solid State Ionics**, 171(3): 251-259.
- Brownson, D. and Banks, C. (2014). The Handbook of Graphene Electrochemistry.
- Catalan, G. and Scott, J.F. (2009). Physics and Applications of Bismuth Ferrite. **Advanced Materials**, 21(24): 2463-2485.

- Chang, S.-J., Chuang, P.-Y., Chong, C.-W., Chen, Y.-J., Huang, J.-C.-A., Chen, P.-W. and Tseng, Y.-C. (2018). Heterostructured ferromagnet–topological insulator with dual-phase magnetic properties. **RSC Advances**, 8(14): 7785-7791.
- Chen, Y.-C., Ko, C.-H., Huang, Y.-C., Yang, J.-C. and Chu, Y.-H. (2012). Domain relaxation dynamics in epitaxial BiFeO<sub>3</sub> films: Role of surface charges. **Journal of Applied Physics**, 112(5): 052017.
- Choi, T., Lee, S., Choi, Y.J., Kiryukhin, V. and Cheong, S.W. (2009). Switchable Ferroelectric Diode and Photovoltaic Effect in BiFeO<sub>3</sub>. **Science**, 324(5923): 63.
- Chu, Y.-H., Martin, L.W., Holcomb, M.B., Gajek M., Han, S.-J., He, Q., Balke, N., Yang, C.-H., Lee, D., Wei, H., Zhan, Q., Yang, P.-L., Arantxa, F.-R., Scholl, A., Wang, S.X. and Ramesh, R. (2008). Electric-field control of local ferromagnetism using a magnetoelectric multiferroic. **Nature Materials**, 7(6): 478-482.
- Chu, Y.-H., Zhan, Q., Martin L.W., Cruz, M.P., Yang, P.-L., Pabst, G.W., Zavaliche, F. Yang, S.-Y., Zhang, J.-X., Chen, L.-Q., Schlom, D.G., Lin, I.-N., Wu, T.-B. and Ramesh, R. (2006). Nanoscale Domain Control in Multiferroic BiFeO<sub>3</sub> Thin Films. **Advanced Materials**, 18(17): 2307-2311.
- Cui, C.Q. and Lee, J.Y. (1995). Nickel deposition from unbuffered neutral chloride solutions in the presence of oxygen. **Electrochimica Acta**, 40(11): 1653-1662.
- Damascelli, A. (2004). Probing the Electronic Structure of Complex Systems by ARPES. **Physica Scripta**, T109: 61.
- Das, R.R., Kim, D. M., Baek, S.H., Eom, C.B., Zavaliche, F., Yang, S.Y., Ramesh, R., Chen, Y.B., Pan, X.Q., Ke, X., Rzchowski, M.S. and Streiffer, S.K. (2006).

Synthesis and ferroelectric properties of epitaxial BiFeO<sub>3</sub> thin films grown by sputtering. **Applied Physics Letters**, 88(24): 242904.

Dong, S., Yamauchi, K., Yunoki, S., Yu, R., Liang, S., Moreo, A., Liu, J.-M., Picozzi, S. and Dagotto, E. (2009). Exchange Bias Driven by the Dzyaloshinskii-Moriya Interaction and Ferroelectric Polarization at G-Type Antiferromagnetic Perovskite Interfaces. **Physical Review Letters**, 103(12): 127201.

Ederer, C. and Spaldin, N.A. (2005). Influence of strain and oxygen vacancies on the magnetoelectric properties of multiferroic bismuth ferrite. **Physical Review B**, 71(22): 224103.

Eerenstein, W., Mathur, N.D. and Scott, J.F. (2006). Multiferroic and magnetoelectric materials. **Nature**, 442(7104): 759-65.

Eerenstein, W., Mathur, N.D. and Scott, J.F. (2006). Multiferroic and magnetoelectric materials. **Nature**, 442(7104): 759-765.

Laderman, S.S. (1989). In situ grown YBa<sub>2</sub>Cu<sub>3</sub>O<sub>7-d</sub> thin films from single-target magnetron sputtering. **Applied Physics Letters**, 55(6): 595-597.

Fiebig, M. (2005). Revival of the magnetoelectric effect. **Journal of Physics D: Applied Physics**, 38(8): R123-R152.

Fleischmann, M. and Saraby-Reintjes, A. (1984). The simultaneous deposition of nickel and hydrogen on vitreous carbon. **Electrochimica Acta**, 29(1): 69-75.

Fong, D.D., Kolpak, A.M., Eastman, J.A., Streiffer, S.K., Stephenson, G.B., Thompson, C., Kim, D.M., Choi, K.J., Eom, C.B., Grinberg, I. and Rappe, A.M. (2006). Stabilization of Monodomain Polarization in Ultrathin PbTiO<sub>3</sub> Films. **Physical Review Letters**, 96(12): 127601.

- Guo, R., You, L., Lin, W., Abdelsamie, A., Shu, X., Zhou, G., Chen, S., Liu, L., Yan, X., Wang, J. and Chen, J. (2020). Continuously controllable photoconductance in freestanding BiFeO<sub>3</sub> by the macroscopic flexoelectric effect. **Nature Communications**, 11(1): 2571.
- Hatt, A.J., Spaldin, N.A. and Ederer, C. (2010). Strain-induced isosymmetric phase transition in BiFeO<sub>3</sub>. **Physical Review B**, 81(5): 054109.
- Huggins, F.E., Galbreath K.C., Eylands, K.E., Loon, L.L.V., Olson, J.A., Zillioux, E. J., Ward, S.G., Lynch, P.A. and Chu, P. (2011). Determination of Nickel Species in Stack Emissions from Eight Residual Oil-Fired Utility Steam-Generating Units. **Environmental Science & Technology**, 45(14): 6188-6195.
- Inkson, B.J. (2016). Scanning electron microscopy (SEM) and transmission electron microscopy (TEM) for materials characterization. In: G. Hübschen, I. Altpeter.
- Iurchuk, V., Schick, D., Bran, J., Colson, D., Forget, A., Halley, D., Koc, A., Reinhardt, M., Kwamen, C., Morley, N.A., Bargheer, M., Viret, M., Gumeniuk, R., Schmerber, G., Doudin, B. and Kundys, B. (2016). Optical Writing of Magnetic Properties by Remanent Photostriction. **Physical Review Letters**, 117(10): 107403.
- Ivanova, Y.A., Ivanou, D.K., Fedonov, A.K., Streltsov, E.A., Demyanov, S.E., Petrov, A.V., Kaniukov, E.Y. and Fink, D. (2007). Electrochemical deposition of Ni and Cu onto monocrystalline n-Si(100) wafers and into nanopores in Si/SiO<sub>2</sub> template. **Journal of Materials Science**, 42(22): 9163-9169.

- Jang, H.W., Baek, S.H., Ortiz, D., Folkman, C.M., Das, R.R., Chu, Y.H., Shafer, P., Zhang, J.X., Choudhury, S., Vaithyanathan, V., Chen, Y.B., Felker, D.A., Biegalski, M.D., Rzchowski, M.S., Pan, X.Q., Schlom, D.G., Chen, L.Q., Ramesh, R. and Eom, C.B. (2008). Strain-Induced Polarization Rotation in Epitaxial (001) BiFeO<sub>3</sub> Thin Films. **Physical Review Letters**, 101(10): 107602.
- Ji, W., Yao, K. and Liang, Y.C. (2010). Bulk Photovoltaic Effect at Visible Wavelength in Epitaxial Ferroelectric BiFeO<sub>3</sub> Thin Films. **Advanced Materials**, 22(15): 1763-1766.
- Kalashnikova, A.M., Kimel, A.V. and Pisarev, R.V. (2015). Ultrafast opto-magnetism. **Physics-Uspekhi**, 58(10): 969-980.
- Kim, J.-W., Vomir, M. and Bigot, J.-Y. (2015). Controlling the Spins Angular Momentum in Ferromagnets with Sequences of Picosecond Acoustic Pulses. **Scientific Reports**, 5(1): 8511.
- King, P.D.C., He, R.H., Eknapakul, T., Buaphet, P., Mo, S.-K., Kanako, Y., Harashima, S., Hikita, Y., Bahramy, M.S., Bell, C., Hussain, Z., Tokura, Y., Shen, Z.-X., Hwang, H.Y., Baumberger, F. and Meevasana, W. (2012). Subband Structure of a Two-Dimensional Electron Gas Formed at the Polar Surface of the Strong Spin-Orbit Perovskite KTaO<sub>3</sub>. **Physical Review Letters**, 108(11): 117602.
- Kisiel, A., Zajdel, P., Lee, P.M., Burattini, E. and Girit, W. (1999). XANES study of K edges of Fe, Co, Ni, and Se in transition metal selenides. Experiment and comparison with LMTO numerical calculations. **Journal of Alloys and Compounds**, 286(1): 61-65.

- Kundys, B. (2015). Photostrictive materials. **Applied Physics Reviews**, 2(1): 011301.
- Lambert, C.H., Mangin, S., Varaprasad, B.S.D.CH.S., Takahashi, Y.K., Hehn, M., Cinchetti, M., Makinowski, G., Hono, K., Fainman, Y., Aeschlimann, M. and Fulleltron, E.E. (2014). All-optical control of ferromagnetic thin films and nanostructures. **Science**, 345(6202): 1337.
- Lebeugle, D., Colson, D., Forget, A., Viret, M., Bataille, A.M. and Gukasov, A. (2008). Electric-Field-Induced Spin Flop in BiFeO<sub>3</sub> Single Crystals at Room Temperature. **Physical Review Letters**, 100(22): 227602.
- Leng, Y. (2013). Materials characterization: Introduction to microscopic and spectroscopic methods: Second edition, 1-376 pp.
- Li, Y. and Wei, X. (2021). Deep in-gap states induced by double-oxygen-vacancy clusters in hydrogenated TiO<sub>2</sub>. **Physica B: Condensed Matter**, 600: 412631.
- Liu, W.J., Tang, X., Tang, Z., Bai, W. and Tang, N. (2013). Oxygen Defects Mediated Magnetism of Ni Doped ZnO. **Advances in Condensed Matter Physics**, 2013.
- Lu, J., Günther, A., Schrettle, F., Mayr, F., Krohns, S., Lunkenheimer, P., Pimenov, A., Travkin, V.D., Mukhin, A.A. and Loidl, A. (2010). On the room temperature multiferroic BiFeO<sub>3</sub>: magnetic, dielectric and thermal properties. **The European Physical Journal B**, 75(4): 451-460.
- Lubk, A., Gemming, S. and Spaldin, N.A. (2009). First-principles study of ferroelectric domain walls in multiferroic bismuth ferrite. **Physical Review B**, 80(10): 104110.
- Martin, L.W., Crane, S.P., Chu, Y.-H., Holcomb, M.B., Gajek, M., Huijben, Yang, C.-H., Balke, N. and Ramesh, R. (2008). Multiferroics and magnetoelectrics: thin films and nanostructures. **Journal of Physics: Condensed Matter**, 20(43): 434220.

- Marton, J.P. and Schlesinger, M. (1968). The Nucleation, Growth, and Structure of Thin Ni-P Films. **Journal of The Electrochemical Society**, 115(1): 16.
- Masingboon, C., Eknapakul, T., Suwanwong, S., Buaphet, P., Nakajima, H., Mo, S.-K., Thongbai, P., King, P.D.C., Maensiri, S. and Meevasana, M. (2013). Anomalous change in dielectric constant of  $\text{CaCu}_3\text{Ti}_4\text{O}_{12}$  under violet-to-ultraviolet irradiation. **Applied Physics Letters**, 102(20): 202903.
- Meevasana, W., King, P.D.C., Re, R.H., Mo, S.-K., Hashimoto, M., Tamai, A., Songsiriritthigul, P., Baumberger, F. and Shen, Z.-X. (2011). Creation and control of a two-dimensional electron liquid at the bare  $\text{SrTiO}_3$  surface. **Nature Materials**, 10(2): 114-118.
- Moreau, J.M., Michel, C., Gerson, R. and James, W.J. (1971). Ferroelectric  $\text{BiFeO}_3$  X-ray and neutron diffraction study. **Journal of Physics and Chemistry of Solids**, 32(6): 1315-1320.
- Munekata, H. (2005). Influence of light on ferromagnetic semiconductors: Magnetization rotation via the angular momentum and the photon energy. **AIP Conference Proceedings**, 772.
- Nakashima, S., Takayama, K., Shigematsu, K., Fujisawa, H. and Shimizu, M. (2016). Growth of epitaxial Mn and Zn codoped  $\text{BiFeO}_3$  thin films and an enhancement of photovoltage generated by a bulk photovoltaic effect. **Japanese Journal of Applied Physics**, 55(10S): 10TA07.

- Ohkoshi, S.-i., Imoto, K., Tsunobuchi, Y., Takano, S. and Tokoro, H. (2011). Light-induced spin-crossover magnet. **Nature Chemistry**, 3(7): 564-569.
- Ohkoshi, S.-I., Tokoro, H., Hozumi, T., Zhang, Y., Hashimoto, K., Mathoniere, C., Bord, I., Rombaut, G., Verelst, M., Moulin, C.C.D. and Villain, F. (2006). Photoinduced Magnetization in Copper Octacyanomolybdate. **Journal of the American Chemical Society**, 128(1): 270-277.
- Pham, D.-T., Tsay, S.-L., Gentz, K., Zoerlein, C., Kossmann, S., Tsay, J.-S., Krichner, B., Wandelt, K. and Broekmann, P. (2007). Quasi-Reversible Chloride Adsorption/Desorption through a Polycationic Organic Film on Cu(100). **The Journal of Physical Chemistry C**, 111(44): 16428-16436.
- Quattropiani, A., Makhort, A.S., Rastei, M.V., Versini, G., Schmerber, G., Barre, S., Dinia, A., Slaoui, A., Rehspringer, J.-L., Fix, T., Colis, S. and Kundys, B. (2018). Tuning photovoltaic response in  $\text{Bi}_2\text{FeCrO}_6$  films by ferroelectric poling. **Nanoscale**, 10(28): 13761-13766.
- Rahmedov, D., Wang, D., Íñiguez, J. and Bellaiche, L. (2012). Magnetic Cycloid of  $\text{BiFeO}_3$  from Atomistic Simulations. **Physical Review Letters**, 109(3): 037207.
- Ramazanoglu, M., Laver, M., Ratcliff, W., Watson, S.M., Chen, W.C., Jackson, A., Kothapalli, K., Lee, S., Cheong, S.-W. and Kiryukhin, V. (2011). Local Weak Ferromagnetism in Single-Crystalline Ferroelectric  $\text{BiFeO}_3$ . **Physical Review Letters**, 107(20): 207206.
- Saenrang, W., Davidson, B.A., Maccherozzi, F., Podkaminer, J.P., Irwin, J., Johnson, R.D., Freeland, J.W., Íñiguez, I., Schad, J.L., Reiersen, K., Frederick, J.C., Vaz, C.A.F., Howald, L., Kim, T.H., Ryu, S., Veenendaal, M.V., Radaelli, P.G., Dhési,

- S.S., Rzchowski, M.S. and Eom, C.B. (2017). Deterministic and robust room-temperature exchange coupling in monodomain multiferroic BiFeO<sub>3</sub> heterostructures. **Nature Communications**, 8(1): 1583.
- Shetty, P.P., Kondekar, N., Thenuwara, A.C., Boebinger, M.G., Wright, S.C., Tian, M. and McDowell, M.T. (2020). In Situ Dynamics during Heating of Copper-Intercalated Bismuth Telluride. **Matter**, 3(4): 1246-1262.
- Shimada, T., Arisue, K., Wang, J. and Kitbindamura, T. (2014). Ab initio study of multiferroic BiFeO<sub>3</sub> (110) surfaces. **Physical Review B**, 89(24): 245437.
- Singh, R.N., Koenig, J.F., Poillerat, G. and Chartier, P. (1990). Electrochemical Studies on Protective Thin Co<sub>3</sub>O<sub>4</sub> and NiCo<sub>2</sub>O<sub>4</sub> Films Prepared on Titanium by Spray Pyrolysis for Oxygen Evolution. **Journal of The Electrochemical Society**, 137(5): 1408-1413.
- Spaldin, N.A. and Fiebig, M. (2005). The Renaissance of Magnetoelectric Multiferroics. **Science**, 309(5733): 391.
- Stanciu, C.D., Hansteen, F., Kimel, A.V., Kirilyuk, A., Tsukamoto, A., Itoh, A. and Rasing, Th. (2007). All-Optical Magnetic Recording with Circularly Polarized Light. **Physical Review Letters**, 99(4): 047601.
- Suwanwong, S., Eknapakul, T., Rattanachai, Y., Masingboon, C., Rattanasuporn, S., Phatthanakun, R., Nakajima, H., King, P.D.C., Hodak, S.K. and Meevasana, W. (2015). The dynamics of ultraviolet-induced oxygen vacancy at the surface of insulating SrTiO<sub>3</sub> (001). **Applied Surface Science**, 355: 210-212.

- Tabares-muñoz, C., Rivera, J.-P. and Schmid, H. (1984). Ferroelectric domains, birefringence and absorption of single crystals of BiFeO<sub>3</sub>. **Ferroelectrics**, 55(1): 235-238.
- Teale, R.W. and Temple, D.W. (1967). Photomagnetic Anneal, A New Magneto-Optic Effect, in Si-Doped Yttrium Iron Garnet. **Physical Review Letters**, 19(16): 904-905.
- Tsay, S.-L., Tsay, J.-S., Fu, T.-Y., Broekmann, P., Sagara, T. and Wandelt, K. (2010). Molecular structures of dicarboxylated viologens on a Cu(100) surface during an ongoing charge transfer reaction. **Physical Chemistry Chemical Physics**, 12(45): 14950-14959.
- Tschuncky, R. and H.-G. Herrmann (Editors), *Materials Characterization Using Nondestructive Evaluation (NDE) Methods*. Woodhead Publishing, pp. 17-43.
- Wang, J., Neaton, J.B., Zheng, H., Nagarajan, V., Ogale, S.B., Liu, B., Viehland, D., Vaithyanathan, V., Schlom, D.G., Waghmare, U.V., Spaldin, N.A., Rabe, K.M., Wutig, M. and Ramesh, R. (2003). Epitaxial BiFeO<sub>3</sub> Multiferroic Thin Film Heterostructures. **Science**, 299(5613): 1719-1722.
- Waterfield P.N., Vibhakar, A.M., Johnson, R.D., Schad, J., Saenrang, W., Bombardi, A., Chmiel, F.P., Eom, C.B. and Radaelli, P.G. (2019). Strain Engineering a Multiferroic Monodomain in Thin-Film BiFeO<sub>3</sub>. **Physical Review Applied**, 11(2): 024035.
- Wu, J., Liu, F., Sasase, M., Ienaga, K., Obata, Y., Yukawa, R., Horiba, K., Kumigashira, H., Okuma, S., Inoshita, T. and Hosono, S. (2019). Natural van der Waals heterostructural single crystals with both magnetic and topological properties. **Science Advances**, 5(11): eaax9989.

- Xie, J., Qin, H., Hao, Y., Cheng, B., Liu, W., Liu, L., Ren, S., Zhou, G., Ji, Z. and Hu, J. (2017). Light Control of Ferromagnetism in ZnO Films on Pt Substrate at Room Temperature. **Scientific Reports**, 7(1): 45642.
- Yamada, Y., Nakamura, T., Yasui, S., Funakubo, H. and Kanemitsu, Y. (2014). Measurement of transient photoabsorption and photocurrent of BiFeO<sub>3</sub> thin films: Evidence for long-lived trapped photocarriers. **Physical Review B**, 89(3): 035133.
- Yan, F., Xing, G., Wang, R. and Li, L. (2015). Tailoring surface phase transition and magnetic behaviors in BiFeO<sub>3</sub> via doping engineering. **Scientific Reports**, 5(1): 9128.
- Yang, C.H., Seidel, J., Kim, S.Y., Rossen, P.B., Yu, P., Gajek, M., Chu, Y.H., Martin, L.W., Holcomb, M.B., He, Q., Maksymovych, P., Balke, N., Kalinin, S.V., Baddorf, A.P., Basu, S.R., Scullin, M.L. and Ramesh, R. (2009). Electric modulation of conduction in multiferroic Ca-doped BiFeO<sub>3</sub> films. **Nature Materials**, 8(6): 485-493.
- Yang, M.-M., Bhatnagar, A., Luo, Z.-D. and Alexe, M. (2017). Enhancement of Local Photovoltaic Current at Ferroelectric Domain Walls in BiFeO<sub>3</sub>. **Scientific reports**, 7: 43070-43070.
- Yang, M., Bhatnagar, A. and Alexe, M. (2015). Electronic Origin and Tailoring of Photovoltaic Effect in BiFeO<sub>3</sub> Single Crystals. **Advanced Electronic Materials**, 1(11): 1500139.

- Yang, S.Y., Seidel, J., Byrnes, S.J., Shafer, P., Yang, C.-H., Rossell, M.D., Yu, P., Chu, Y.-H., Scott, J.F., Ager, J.W., Martin, L.W. and Ramesh, R. (2010). Above-bandgap voltages from ferroelectric photovoltaic devices. **Nature Nanotechnology**, 5(2): 143-147.
- Yashina, L.V., Sánchez-Barriga, J., Scholz, M.R., Volykhov, A.A., Sirotina, A.P., Vera, Neudachina, S., Tamm, M.E., Varykhalov, A., Marchenko, D., Springholz, G., Bauer, G., Knop-Gericke, A. and Rader, O. (2013). Negligible Surface Reactivity of Topological Insulators Bi<sub>2</sub>Se<sub>3</sub> and Bi<sub>2</sub>Te<sub>3</sub> towards Oxygen and Water. **ACS Nano**, 7(6): 5181-5191.
- Yuan, G.L., Martin, L.W., Ramesh, R. and Uedono, A. (2009). The dependence of oxygen vacancy distributions in BiFeO<sub>3</sub> films on oxygen pressure and substrate. **Applied Physics Letters**, 95(1): 012904.
- Zhan, P., Wang, W., Liu, C., Hu, Y., Li, Z., Zhang, Z., Zhang, P., Wang, B. and Cao, X. (2012). Oxygen vacancy-induced ferromagnetism in un-doped ZnO thin films. **Journal of Applied Physics**, 111(3): 033501.
- Zhang, J., Sun, J., Li, Y., Shi, F. and Cui, Y. (2017). Electrochemical Control of Copper Intercalation into Nanoscale Bi<sub>2</sub>Se<sub>3</sub>. **Nano Letters**, 17(3): 1741-1747.
- Zhang, J.X., He, Q., Trassin, M., Luo, W., Yi, D., Rossell, M.D., Yu, P., You, L., Wang, C.H., Kuo, C.Y., Heron, J.T., Hu, Z., Zeches, R.J., Lin, H.J., Tanaka, A., Chen, C.T., Tjeng, L.H., Chu, Y-H. and Ramesh R. (2011). Microscopic Origin of the Giant Ferroelectric Polarization in Tetragonal-like BiFeO<sub>3</sub>. **Physical Review Letters**, 107(14): 147602.
- Zhao, T., Scholl, A., Zavaliche, F., Lee, K., Barry, M., Doran, A., Cruz, M.P., Chu, Y.H., Ederer, C., Spaldin, N.A., Das, R.R., Kim, D.M., Baek, S.H., Eom, C.B.

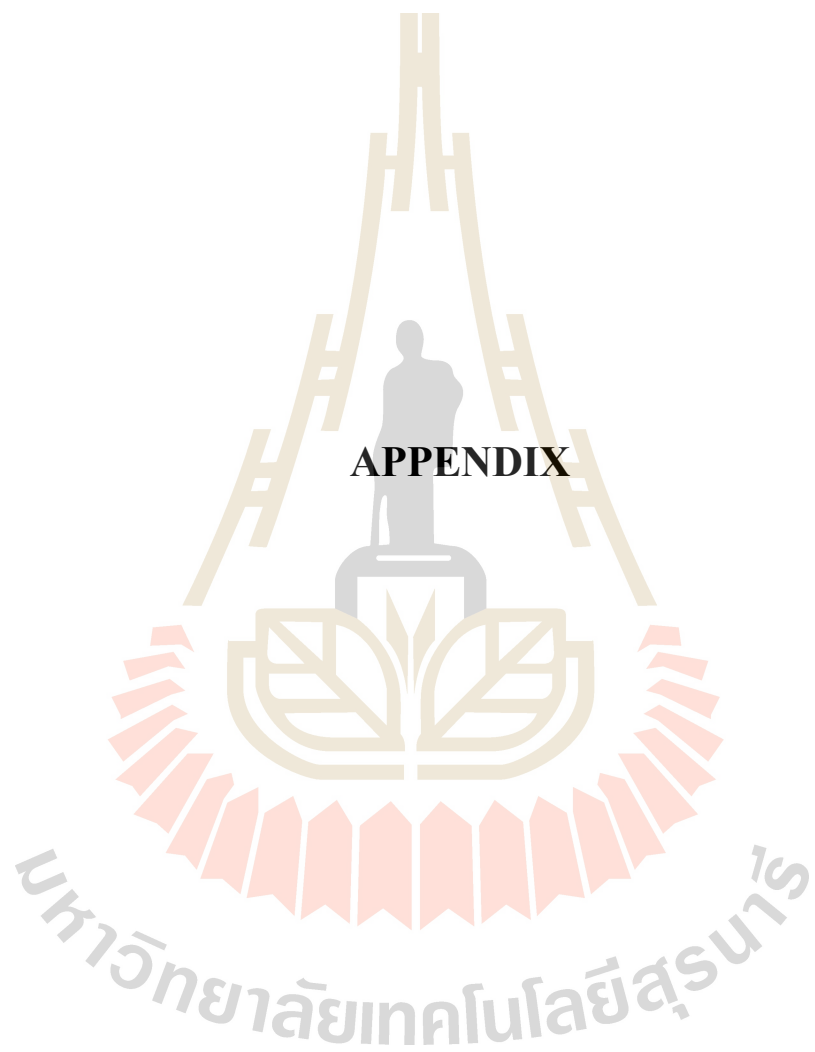
and Ramesh, R. (2006). Electrical control of antiferromagnetic domains in multiferroic BiFeO<sub>3</sub> films at room temperature. **Nature Materials**, 5(10): 823-829.

Zhou, X.J., Wannberg, B., Yang, W.L., Brouet, V., Sun, Z., Douglas, J.F., Dessau, D., Hussain, Z. and Shen, Z.-X. (2005). Space charge effect and mirror charge effect in photoemission spectroscopy. **Journal of Electron Spectroscopy and Related Phenomena**, 142(1): 27-38.

Zhou, Y., Fang, L., You, L., Ren, P., Wang, L. and Wang, J. (2014). Photovoltaic property of domain engineered epitaxial BiFeO<sub>3</sub> films. **Applied Physics Letters**, 105(25): 252903.

Zhu, M., Du, Z., Jing, L., Yoong Tok, A.I. and Tong Teo, E.H. (2015). Optical and electro-optic anisotropy of epitaxial PZT thin films. **Applied Physics Letters**, 107(3): 031907.





**APPENDIX**

## APPENDIX

### 1. I-V Characterization of BFO/SRO/STO

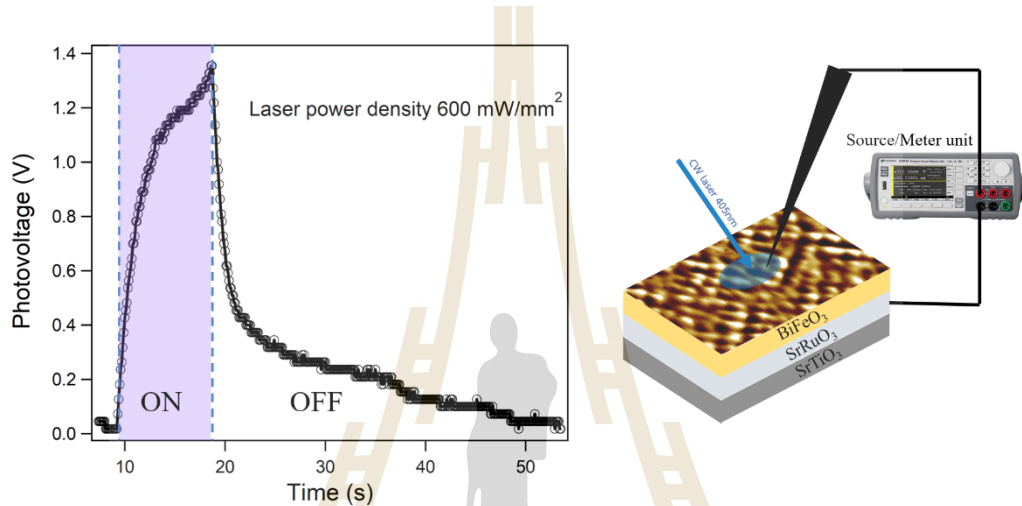


**Figure 1** The photo-response of the BiFeO<sub>3</sub>/SrRuO<sub>3</sub>/SrTiO<sub>3</sub> film under laser illumination with an intensity of 600 mW/mm<sup>2</sup>(a) and experiment set up (b).

Test structure in perpendicular geometry, based on asymmetric silver tip top electrodes and bottom SRO layer electrodes. Voltage characteristics of samples were measured under saturation laser illumination in both dark and light illumination (600 mW/mm<sup>2</sup>) on time domain. The photo induced voltages equal to 1.35V, show that there is an internal electric field was generated inside along perpendicular direction of BFO film.

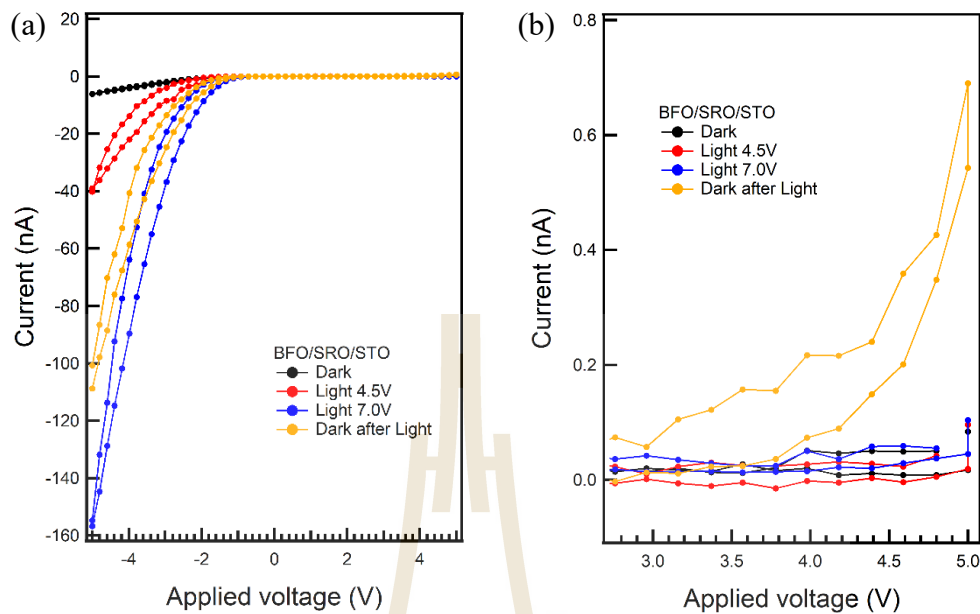


**Figure 2** Light and dark current as a function of applied field for BFO/SRO/STO in the range -5V to 5V (a) and the range 2.5V to 5V (b).

Interestingly, dark-light IV characteristics were measured to investigate if a change in conductivity appeared under illumination. The resulting current of photoexcited carriers, driven by the intrinsic polarization, can be described by the following equation.

$$J = (\sigma_d + \sigma_{ph})\xi$$

which is typical of photoferroelectrics materials. (Tabares-muñoz et al., 1984).  $\sigma_d$  and  $\sigma_{ph}$  represent the dark and light components of the conductivity, respectively. Under illumination in light of wavelength equal to or larger than the band gap the photoconductivity will effectively turn on and a large current should be measured at all

applied fields. A laser with wavelength 405 nm and three different power density were chosen as an appropriate source to test for photoexcitation given that literature theoretical calculations and absorption/transmission spectra suggest that the band gap of BFO lies in the visible/near-visible range. Preliminary results indicated a jump in conductivity under illumination at negative nonzero applied fields. Noting that large leakage currents in BFO have typically been attributed to the presence of oxygen vacancies, corresponding to our UPS results. The presence of oxygen vacancies effectively introduces electrons into the lattice and increases the free-carrier concentration. Figure 4.21 shows dark and light IV characteristics of 400nm thick BFO on SRO/STO substrate. Figure 4.21(a) refer to dark and light IV curves taken on sample in upon of 70 and 600 mW/mm<sup>2</sup> respectively. Figure 4.21 (b) shows no immediate change of IV curve in positive region of measurement, small current flow due to diode effect caused by Schottky barrier between the interface of BFO. After laser exposed onto the surface, the measurable current (~0.7 nA) implies that leakage current because of oxygen vacancy or photo-ferroelectric effect when exposed to light for a long time. (Chen et al., 2012).

## 2. Raising time analysis of Kerr angle rotation in BFO/SRO/STO sample

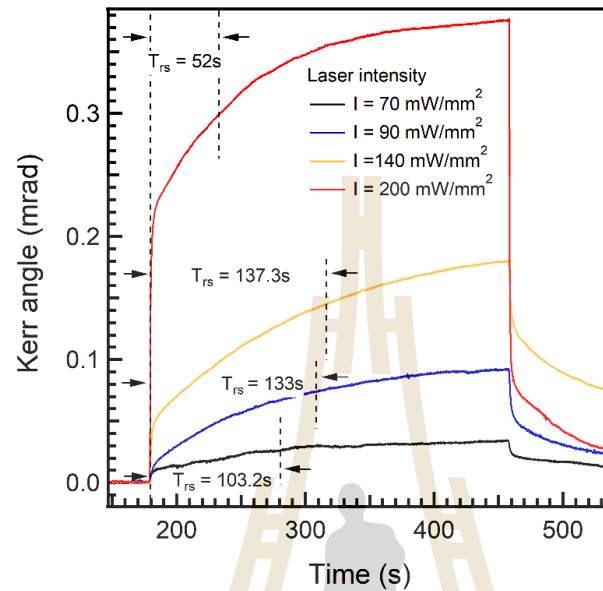


**Figure 3** Raising time of Kerr rotation under laser illumination of 70, 90, 140, 200  $\text{mW}/\text{mm}^2$ , respectively.

We define the raising time of Kerr rotation is the time of Kerr angle increment to 80% of saturated value. By looking at the raising time of Kerr angle rotation, the result shows a value of 52 seconds when BFO exposed to a laser with an intensity of 200  $\text{mW}/\text{mm}^2$ . It can be seen in figure 3 that the raising time is more than the response time of bulk photovoltaic effect (BPVE) in BFO which is equal to  $\sim 0.1$  s (Alexe and Hesse, 2011; Iurchuk et al., 2016; Quattropani et al., 2018). But consistent with the our result of electric field induced Kerr rotation, implied that the gradually occurrence of internal electric field caused by laser induced oxygen vacancy (Suwanwong et al., 2015).

## CURRICULUM VITAE

**Name** Mr. Siwat Pol-in

**Date of Birth** June 26, 1984

**Place of Birth** 58/2, Thap Thiang sub-district, Mueang district, Trang,  
92000, Thailand.

**Education**

2014-2021 Suranaree University of Technology, Nakhon  
Ratchasima, Thailand.  
Ph.D. in Physics

2006-2008 Chiang Mai University  
M.Sc. in Physics

2002-2005 Prince of Songkla University, Songkla, Thailand.  
B.Sc. in Physics

### Position and Place of Work

Lecturer

Rajamangala University of Technology Suvarnabhumi

Nonthaburi Campus: 7/1 Nonthaburi1 road, Suanyai

district, Nonthaburi, 11000, Thailand